PLASMONIC METAMATERIAL BASED STRUCTURES FOR DESIGNING OF MULTIBAND AND THERMALLY TUNABLE LIGHT ABSORBERS, MULTIPLE THERMAL INFRARED EMITTER, AND HIGH-CONTRAST ASYMMETRIC TRANSMISSION OPTICAL DIODE

A THESIS SUMBITTED TO

THE GRADUATE SCHOOL OF ENGINEERING AND SCIENCE

OF BILKENT UNIVERSITY

IN PARTIAL FULFILLMENT OF THE REQIREMENTS FOR

THE DEGREE OF

MASTER OF SCIENCE

IN

PHYSICS

By

Ataollah Kalantari Osgouei

July 2021

PLASMONIC METAMATERIAL BASED STRUCTURES FOR DESIGNING OF MULTIBAND AND THERMALLY TUNABLE LIGHT ABSORBERS, MULTIPLE THERMAL INFRARED EMITTER, AND HIGH-CONTRAST ASYMMETRIC TRANSMISSION OPTICAL DIODE

By Ataollah Kalantari Osgouei

July 2021

We certify that we have read this thesis and that in our opinion it is fully adequate, in scope and in quality, as a thesis for the degree of Master of Science.

Ekmel Özbay (Advisor)

Oğuz Gülseren

Alpan Bek

Approved for the Graduate School of Engineering and Science:

Ezhan Karaşan
Director of the Graduate School

ABSTRACT

PLASMONIC METAMATERIAL BASED STRUCTURES FOR DESIGNING OF MULTIBAND AND THERMALLY TUNABLE LIGHT ABSORBERS, MULTIPLE THERMAL INFRARED EMITTER, AND HIGH-CONTRAST ASYMMETRIC TRANSMISSION OPTICAL DIODE

Ataollah Kalantari Osgouei
M.S. in Physics
Advisor : Ekmel Özbay
July 2021

Metamaterials with sub-wavelength nanostructures refer to a class of synthetic materials that possess exotic electromagnetic properties which cannot be observed with natural materials. Negative refractive index, asymmetric light transmission, invisible cloaking, and lasing are examples of these attributes. Among these possible applications, the concept of light confinement and harvesting by subwavelength structures have attracted considerable attention due to their widespread applications ranging from thermal emission, optical modulator, sensing, and photodetectors. Here, we propose and design plasmonic metamaterials with subwavelength structures in four different application areas, namely 1) Hybrid indium tin oxide-Au metamaterial absorber in the visible and near-infrared ranges for selective thermal emissions and sensors. 2) Active tuning from narrowband to broadband absorbers using a sub-wavelength VO_2 for optical modulator. 3) A spectrally selective nanoantenna emitter compatible with multiple thermal infrared applications. 4) Diode like high-contrast asymmetric transmission of linearly polarized waves.

In the first work, we propose a multi-band Metamaterial Perfect absorber (MPA) with two narrowband absorption responses that are centered on the visible and near-infrared (NIR) wavelengths [$773\,nm$ and $900\,nm$, respectively] and a broadband absorptive characteristic in another window in the NIR region [ranging from $1{,}530\,nm$ to $2{,}700\,nm$

with a bandwidth of $1{,}170\ nm$]. The MPA comprises a periodic array of self-aligned hybrid indium tin oxide (ITO)-Au split-ring-resonators that are separated from an optically thick bottom reflector with a SiO_2 layer. Based on numerical calculations, which are accompanied with a semi-analytical examination, we find that the dual narrowband and broadband responses are attributed to the hybridization of the optical responses of gold as a plasmonic material with the ones of ITO. Note that ITO acts as a low-loss dielectric in the visible range and a lossy plasmonic material in the NIR region. Moreover, due to the applied symmetry in the unit cell of the metamaterial, the proposed MPA represents polarization insensitive and omnidirectional absorptive features. The proposed metastructure can find potential applications in selective thermophotovoltaic devices, thermal emitters, and sensors.

In the second work, we propose an MPA with diverse functionalities enabled by vanadium dioxide (VO_2) embedded in a metal-dielectric plasmonic structure. For the initial design purpose, a Silicon (Si) nanograting on a Silver (Ag) mirror is proposed to have multiple resonant responses in the near infrared (NIR) region. Then, the insertion of a thin VO_2 layer at the right position enables the design to act as an on/off switch and resonance tuner. In the insulator phase of VO_2, in which the permittivity data of VO_2 is similar to that of Si, a double strong resonant behavior is achieved within the NIR region. By increasing the temperature, the state of VO_2 transforms from insulator to metallic so that the absorption bands turn into three distinct resonant peaks with close spectral positions. Upon this transformation, a new resonance emerges and the existing resonance features experience blue/red shifts in the spectral domain. The superposition of these peaks makes the overall absorption bandwidth broad. Although Si has a small thermo-optic coefficient, owing to strong light confinement in the ultrasmall gaps, a substantial tuning can be achieved within the Si nanogratings. Therefore, the proposed hybrid design can provide multi-resonance tunable features to cover a broad range and can be a promising strategy for the design of linearly thermal-tunable and broadband MPAs. Owing to the proposed double tuning feature, the resonance wavelengths exhibits great sensitivity to temperature, covering a broad wavelength range. Overall, the proposed design strategy demonstrates diverse functionalities enabled by the integration of a thin VO_2 layer with plasmonic

absorbers.

In the third work, we design a wavelength-selective nanoantenna emitter based on the excitation of gap-surface plasmon modes using a metal–insulator–metal configuration (silicon dioxide (SiO_2) sandwiched between silver (Ag) layers) for satisfying multiple infrared applications. The proposed design, which is called design I, realizes triple narrowband perfect absorptions at the resonance wavelengths of 1524 nm, 2279 nm, and 6000 nm, which perfectly match the atmospheric absorption bands while maintaining relatively low emissivity in the atmospheric transparency windows of $3-5\ \mu$m and $8-12\ \mu$m. Later, the functionality of design I is extended, which is called design II, to include a broadband absorption at the near-infrared region to minimize the solar irradiation reflection from the nanoantenna emitter. Finally, single- and three-layer graphene are introduced to provide a real-time tuning of the infrared signature of the proposed nanoantenna emitter (design II). It is also demonstrated that the three-layer graphene structure can suppress an undesired absorption resonance wavelength related to the intrinsic vibrational modes (optical phonons) of the SiO_2 layer by 53.19% compared to 25.53% for the single-layer one. The spectral analysis of design I is validated using both analytical and numerical approaches where the numerical simulation domain is extended for the analysis of design II. The thermal characteristic analyses of design I and design II (without/with graphene layers) reveal that infrared signatures of the blackbody radiation are significantly reduced for the whole wavelength spectrum at least by 96% and 91% within a wide temperature ranging from room temperature to $500\ K$, respectively.

In the fourth and final work, we present a narrow-band optical diode with a high-contrast forward-to-backward ratio at the near-infrared (NIR) region. The design has a forward transmission of approximately 88%, and a backward one of less than 3%, yielding a contrast ratio of greater than 14.5 dB at a wavelength of 1550 nm. The structure is composed of a one-dimensional diffraction grating on top of a dielectric slab waveguide, both of which are made of silicon nitride (Si_3N_4), and all together are placed over a silver (Ag) thin film embedded on a dielectric substrate. Utilizing a dielectric-based diffraction grating waveguide on a thin silver layer leads to the simultaneous excitation of two surface

plasmon modes known as long- and short-range surface plasmon polaritons (SPPs) at both interfaces of the metallic layer. The plasmon-tunneling effect, which is the result of the coupling of SPPs excited at the upper interface of the metallic layer to the radiation modes, provides a high asymmetric transmission (AT) property. The spectral response of the proposed high-contrast AT device is verified using both rigorous coupled-wave analysis as an analytical approach and finite difference time domain as a numerical one.

Keywords: Hybrid metamaterials, light absorbers, Visible, Near infrared, Vanadium dioxide, Plasmonic structure, Active tunable metamaterial, Localized surface plasmon, Nanoantenna emitter, Wavelength selectivity, Gap surface plasmon, Thermal radiation management, Solar absorber, Asymmetric transmission, Diffraction grating, Plasmon tunneling.

ÖZET

Çoklu bant ve termal ayarlanabilir ışık soğurucuları, çoklu termal kızılötesi yayıcı ve yüksek karşıtlıklı asimetrik iletim optik diyot tasarımı için plazmonik metamalzeme tabanlı yapılar

Ataollah Kalantari Osgouei
Fizik, Yüksek Lisans
Tez Danışmanı: Ekmel Özbay
Temmuz 2021

Alt dalga boyu nanoyapılara sahip metamalzemeler, doğal malzemelerle gözlemlenemeyen egzotik elektromanyetik özelliklere sahip bir sentetik malzeme sınıfını ifade eder. Negatif kırılma indisi, asimetrik ışık iletimi, görünmez perdeleme ve lazer bu özelliklere örnektir. Bu olası uygulamalar arasında, ışığın sınırlandırılması ve dalga boyu altı yapılar tarafından hasat edilmesi kavramı, termal emisyon, optik modülatör, algılama ve fotodedektörlere kadar uzanan yaygın uygulamaları nedeniyle büyük ilgi görmüştür. Burada, seçici termal emisyonlar ve sensörler için görünür ve yakın kızılötesi aralıklarda dört farklı uygulama alanında, yani 1) hibrit indiyum kalay oksit-Au meta malzeme soğurucu alt dalga boyu yapılarına sahip metamalzemeleri öneriyor ve tasarlıyoruz. 2) Optik modülatör için bir alt dalga boyu VO_2 kullanarak dar banttan geniş bant soğuruculara aktif ayarlama. 3) Çoklu termal kızılötesi uygulamalarla uyumlu, spektral olarak seçici bir nanoanten yayıcı. 4) Doğrusal polarize dalgaların yüksek kontrastlı asimetrik iletimi gibi diyot.

İlk çalışmada, görünür ve yakın Kızılötesi (nır) dalga boylarına [sırasıyla 773 nm ve 900 nm] odaklanan iki dar bant emme tepkisine sahip çok bantlı bir MPA ve NIR bölgesindeki başka bir pencerede geniş bant emici bir özellik öneriyoruz [1,530 nm'den 2,700 nm'ye kadar 1,170 nm bant genişliği ile]. MPA, bir SiO_2 tabakası ile optik olarak kalın bir alt reflektörden ayrılan periyodik bir dizi kendinden hizalı hibrit indiyum kalay oksit (ITO)-Au bölünmüş halka rezonatöründen oluşur. Yarı analitik bir inceleme ile

birlikte verilen sayısal hesaplamalara dayanarak, çift dar bant ve geniş bant tepkilerinin, altının optik tepkilerinin Ito ile plazmonik bir malzeme olarak hibridizasyonuna atfedildiğini görüyoruz. ITO'NUN görünür aralıkta düşük kayıplı bir dielektrik ve NIR bölgesinde kayıplı bir plazmonik malzeme olarak hareket ettiğini unutmayın. Ayrıca, metamateryalin birim hücresindeki uygulanan simetri nedeniyle, önerilen MPA polarizasyona duyarsız ve çok yönlü emici özellikleri temsil eder. Önerilen altyapı, seçici termofotovoltaik cihazlarda, termal yayıcılarda ve sensörlerde potansiyel uygulamalar bulabilir.

İkinci çalışmada, metal-dielektrik plazmonik bir yapıya gömülü vanadyum dioksit (VO_2) tarafından sağlanan çeşitli işlevlere sahip bir MPA öneriyoruz. İlk tasarım amacı için, bir gümüş (Ag) ayna üzerinde bir silikon (Si) nanograsyonun, yakın Kızılötesi (NIR) bölgesinde çoklu rezonans tepkilerine sahip olması önerilmektedir. Sonra, doğru konumda eklenen ince bir VO_2 katmanı yapıyı aç/kapat anahtar ve rezonans ayarlayıcı olarak kullanılmasını sağlar. VO_2'NİN geçirgenlik verilerinin Si'ninkine benzer olduğu VO_2'NİN izolatör fazında, NIR bölgesi içinde çift güçlü bir rezonans davranışı elde edilir. Sıcaklığı arttırarak, VO_2 durumu izolatörden metale dönüşür, böylece emme bantları yakın spektral pozisyonlara sahip üç farklı rezonans zirvesine dönüşür. Bu dönüşüm üzerine, yeni bir rezonans ortaya çıkar ve mevcut rezonans özellikleri spektral alanda Mavi/Kırmızı kaymalar yaşar. Bu zirvelerin süperpozisyonu, genel emilim bant genişliğini geniş yapar. Si, küçük bir termo-optik katsayıya sahip olmasına rağmen, ultra küçük boşluklarda güçlü ışık hapsi nedeniyle, Si nanogratings içinde önemli bir ayar elde edilebilir. Bu nedenle, önerilen hibrit tasarım, geniş bir yelpazeyi kapsayacak şekilde çok rezonanslı ayarlanabilir özellikler sağlayabilir ve doğrusal olarak termal olarak ayarlanabilir ve geniş bant Mpa'ların tasarımı için umut verici bir strateji olabilir. Önerilen çift ayar özelliği sayesinde, rezonans dalga boyları geniş bir dalga boyu aralığını kapsayan sıcaklığa karşı büyük hassasiyet gösterir. Genel olarak, önerilen tasarım stratejisi, ince bir VO_2 tabakasının plazmonik emicilerle entegrasyonu ile sağlanan çeşitli işlevleri göstermektedir.

Üçüncü çalışmada, çoklu Kızılötesi uygulamaları karşılamak için bir metal-izolatör-metal

konfigürasyonu (Gümüş (Ag) tabakaları arasına sıkıştırılmış silikon dioksit (SiO_2)) kullanarak boşluk yüzey plazmon modlarının uyarılmasına dayanan bir dalga boyu seçici nanoantenna yayıcı tasarlıyoruz. $3-5$ mikron ve $8-12$ mikron atmosferik şeffaflık pencereleri nispeten düşük emisyon korurken tasarım I olarak adlandırılan önerilen tasarım, atmosferik emme bantlarıyla eşleşen, 1524 nm, 2279 nm, and 6000 nm rezonans dalga boylarında üçlü dar mükemmel emilimleri sağlar. Daha sonra, Tasarım II olarak adlandırılan tasarım I'in işlevselliği, nanoantenna yayıcıdan gelen güneş ışınımı yansımasını en aza indirmek için yakın Kızılötesi bölgede geniş bant emilimini içerecek şekilde genişletilir. Son olarak, önerilen nanoantenna yayıcının (tasarım II) Kızılötesi imzasının gerçek zamanlı olarak ayarlanmasını sağlamak için tek ve üç katmanlı grafen tanıtılmıştır. Ayrıca, üç katmanlı grafen yapısının, SiO_2 tabakasının içsel titreşim modları (optik fononlar) ile ilgili istenmeyen bir emme rezonans dalga boyunu, tek katmanlı olan için $\%25.53$'e kıyasla $\%53.19$ oranında baskılayabildiği gösterilmiştir. Tasarım I'in spektral analizi, tasarım II'nin analizi için sayısal simülasyon alanının genişletildiği hem analitik hem de sayısal yaklaşımlar kullanılarak doğrulanır. Tasarım I ve tasarım II'nin termal karakteristik analizleri (grafen tabakaları olmadan/olmadan), kara cisim radyasyonunun Kızılötesi imzalarının, tüm dalga boyu spektrumu için sırasıyla oda sıcaklığından $500\ K$'ye kadar geniş bir sıcaklıkta en az $\%96$ ve $\%91$ oranında önemli ölçüde azaldığını ortaya koymaktadır.

Dördüncü ve son çalışmada, yakın Kızılötesi (NIR) bölgesinde yüksek kontrastlı ileri-geri oranına sahip dar bantlı bir optik diyot sunuyoruz. Tasarım, yaklaşık $\%88$'lik bir ileri iletime ve $\%3$'ten daha az bir geriye doğru iletime sahiptir ve 1550 nm dalga boyunda 14.5 dB'den daha büyük bir kontrast oranı sağlar. Yapı, her ikisi de silisyum nitrürden (Si_3N_4) yapılmış bir dielektrik levha dalga kılavuzunun üstünde tek boyutlu bir kırınım ızgarasından oluşur ve hepsi birlikte bir dielektrik substrat üzerine gömülü bir gümüş (Ag) ince film üzerine yerleştirilir. İnce bir gümüş tabaka üzerinde dielektrik bazlı bir kırınım ızgarası dalga kılavuzunun kullanılması, metalik tabakanın her iki arayüzünde uzun ve kısa menzilli yüzey plazmon polaritonları (Spp'ler) olarak bilinen iki yüzey plazmon modunun eşzamanlı uyarılmasına yol açar. Metalik tabakanın üst arayüzünde uyarılan Spp'lerin radyasyon modlarına bağlanmasının sonucu olan plazmon tünelleme etkisi,

yüksek asimetrik iletim (AT) özelliği sağlar. Önerilen yüksek kontrastlı AT Cihazının spektral tepkisi, analitik bir yaklaşım olarak hem sıkı birleştirilmiş dalga analizi hem de sayısal olarak sonlu fark zaman alanı kullanılarak doğrulanır.

Anahtar kelimeler: Hibrit metamalzemeler, ışık emiciler, görünür, yakın kızılötesi, vanadyum dioksit, plazmonik yapılar, aktif ayarlanabilir metamalzemeler, lokalize yüzey plazmonları, nanoanten yayıcı, dalgaboyu seçiciliği, boşluk yüzey plazmonları, termal ışıma yönetimi, güneş soğurucu, asimetrik iletim, kırınım ızgarası, plazmon tünellemesi

ACKNOWLEDGEMENT

First and foremost, I would like to express my sincere gratitude to my advisor Prof. Dr. Ekmel Özbay for giving me the opportunity to do research and providing invaluable advice throughout my M.S. study. His extensive knowledge, unwavering support, insightful suggestions, vision, and motivation have deeply inspired me. His guidance has provided positive encouragement and a warm spirit to write this thesis. I could not have imagined having a better advisor and mentor for my M.S. study.

Besides my advisor, I would also like to show gratitude to Prof. Dr. Oğuz Gülseren and Assoc. Dr. Alpan Bek for being in my thesis committee, their constructive comments, practical suggestions, and helpful advice to my thesis.

Getting through my dissertation required more than academic support. I cannot begin to express my gratitude to Dr. Amir Ghobadi for providing me professional support and unwavering guidance during my most difficult times. He has taught me a great deal about both scientific research and academia.

I am especially indebted to Dr. Bahram Khalichi for his friendship, empathy, and great sense of humor. I would like to thank him for his keen interest in reading and providing insightful suggestions to my manuscripts. He has also taught me what a good scientist (researcher) should be.

I must also express my very profound gratitude to all engineers at NANOTAM/ABMN, and UNAM for their passionate participation in my projects. Especially, I thank Dr. Bahram Butun, MR. Mert Satımış from NANOTAM/ABMN, and MR. Abdullah Kafadenk from UNAM. I would like to thank MS. Gamze Seğmenoğlu from NANOTAM/ABMN and MS. Fatma Gül Akca from the Physics department who always worked actively to make my life easier at Bilkent University.

I am grateful to all of those my friends and office mates whom I have had the pleasure to work and spent fun times during my graduate life. I would like to especially thank my office mate Salahuddin Zafar for his unwavering support and for reminding me to take breaks and have funs when I have been stressed out. From NANOTAM (old building), I would like to thank Veysel Erçağlar, Volkan Ertürk, Tayfur Kaya, Ebru Buhara, Oguz Odabaşi, Zeinab Eftekhari, Mohsin Habib, Ekin Brican Buşdurmaz, Dr. Alireza Rahimi Rashed, and Imre Ozbay. From UNAM, I would like to thank Farzan, Mohammadali, Mirali, Pedram, and Amir for making so many ordinary moments extraordinary. From Bilkent University, I would like to thank Enes, Sina, Salar, Shahab, Mehdi, Muhammad, and Amirali for their friendships.

Last but not the least, I am extremely grateful to my parents, Parviz Kalantari Osgouei and Azam Moayed for their love, caring, and supporting me spiritually for educating and preparing me for a better future. I am very much thankful for my brother Amirali Kalantari Osgouei and his handsome son Amirreza Kalantari Osgouei for their help, understanding, and unrelenting supports in the past three years. None of these achievements could have happened without my family.

Ataollah Kalantari Osgouei

“Today’s accomplishments were yesterday’s impossibilities.” (Robert H. Schuller)

TABLE OF CONTENTS

LIST OF TABLES

LIST OF FIGURES

CHAPTER 1

INTRODUCTION

"I have no special talents. I am only passionately curious." (Albert Einstein)

1.1. Introduction to surface plasmon

One of the most remarkable features of metallic nanostructures is surface plasmons (SPs). They consist of a collective oscillation of electrons at the interface between a metal and a dielectric medium. Although SPs can be excited at the surface of bulk metals, they are particularly important in the case of nanostructures [1]–[3]. Because nanostructures have a high surface-to-volume ratio, SPs can control their optical characteristics, allowing for novel phenomena properties not available in bulk materials. Depending on the geometry and shapes of the nanostructures, there are different types of SPs excited in the structures. In nanoparticles with 0 −dimension (i.e., the dimensions of the nanoparticles are much smaller than the incident wavelength of light), charge density oscillations in phase within nanoparticles excited SPs. These exciting plasmons are characterized by a resonant frequency and they are generally known as Localized surface plasmon (LSPs) [4]. For the case of thin films with dimensions that are much larger than the incident wavelength of light, SPs are propagating waves with definite dispersion relation and they are called extended surface plasmons (ESPs) [5]. Finally, for the case of dimensions similar to the light wavelength (mesoscopic systems), SPs are stationary waves at the interfaces [1]–[3]. Except for certain wavelengths that are an integer number of times the nanostructure

dimensions, the interference of the initial waves with those reflected at the edge of the nanostructures is, on average, destructive. The interference produces stationary waves, known as plasmon modes, at these specific wavelengths [1]–[3]. Therefore, we can attribute SPs to mechanical oscillations by comparing LSPs, ESPs, and plasmon modes to a mass with a spring, an infinite rope, and an oscillating string, respectively.

1.2. Brief history of Surface plasmons

LSPs have long been used by artists to create brilliant colors in glass artifacts and artwork, where for instance, the inclusion of metal nanoparticles of various sizes or shapes of the glass created a wide range of colors. One of the most renowned examples is the Lycurgus cup from the 4^{th} century A.D., which glows green when it is illuminated from outside and observed with reflected light and shines in red when it is illuminated from inside in transmitting light conditions (see Fig. 1.1). Other examples might be found in church or cathedral window glass. However, the first scientific studies about LSPs are found in 1904, when Maxwell Garnett explained the bright colors observed in metal-doped glasses using the theory of Paul Drude for metals [6]. Gustav Mie later proposed his theory of light scattering by homogeneous spherical particles, which was published in 1908 [7]. Later, Richard Gans published the expansion for spheroidal particles in 1912 for Au nanoparticles, and the Mie-Gans theory is now widely being used in the field of nanotechnology [8]. DeVoe also applied the discrete dipole approximation (DDA) method for more complicated nanoparticles in 1964 [9].

The earliest recorded research on ESPs, on the other hand, dated back to 1902, when Robert Woods noticed abnormalities in optical reflection measurements on metallic grating [10]. Ugo Fano later investigated the abnormalities discovered by Woods and found that they were linked to electromagnetic waves on the surface of metallic grating [11]. David Pines theoretically defined the characteristics of energy loss experienced by rapid electrons moving through metals in 1956, attributing them to collective oscillations of free electrons in the metal known as plasmons [12]. Rufus Ritchie proposed the idea of SPs in 1957 in the context of electron energy losses in thin films, demonstrating that plasmon modes can exist near metal surfaces. Powell and Swan provided the experimental

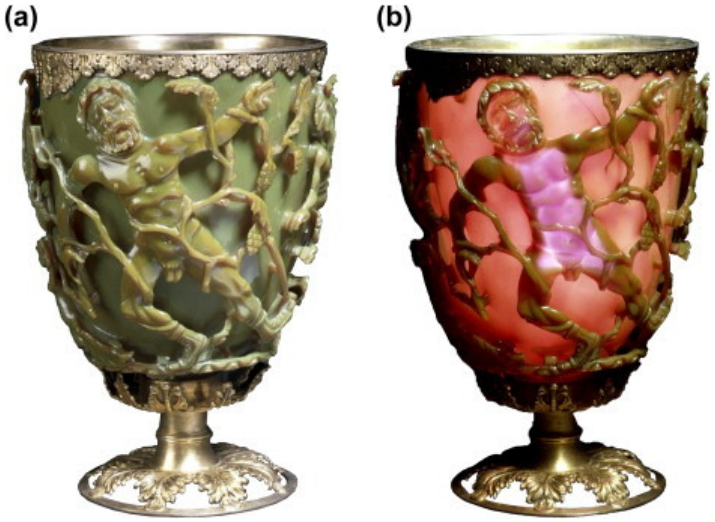

Figure 1.1. The Lycurgus cup dating from the 4th century A.D. in (a) reflected and (b) transmitted light. From http://www.thebritishmuseum.ac.uk/ science/lycurguscup/sr-lycugus-p1.html.

verification two years later [13]. Later, Ritchie noticed Wood's anomalies in 1968 and explained them in terms of surface plasmon resonances excited on the grating [14]. Andreas Otto, Enrich Kretschmann, and Heinz Raether presented methods for the optical excitation of SPs. metal films in 1968, which made significant developments in the research of ESPs [15]–[17] At the same time, Uwe Kreibig and Peter Zacharias made significant advances in the SPs of metal nanostructures in 1970 [18]. Stephen Cunningham coined the term surface plasmon polariton (SPP) and the surface-enhanced Raman scattering (SERS) was first detected by Martin Fleischmann [19], [20]. Since then, the extended use of SERS, the ability to control the optical characteristics of metal nanostructures, and the development of SP-based sensors have all contributed to the rapid expansion into a wide range of applications.

1.3. Theory of surface plasmons

The Drude model, which assumes that the metal is made of a lattice of ionic cores and a conduction electron moves freely inside the metal, can accurately represent most of the optical properties of bulk metals. These conduction electrons can observe oscillations

known as bulk plasmons, which in the framework of quantum physics are quantified. The quantum of the volume plasmon has an energy $\hbar\omega_p = \hbar\sqrt{\frac{4\pi ne^2}{m_0}}$ of the order of 10 eV, where ω_p denotes the plasma frequency and n the electron density [21].

The idea of SPs is a significant expansion of plasmon physics, as it shows that electromagnetic waves may travel through a metallic surface with a broad spectrum of frequencies from $\omega = 0$ up to $\omega = \omega_p/\sqrt{2}$, depending on the wavevector k [2]. The dispersion relationships of different types of plasmons demonstrate that for the same frequency values, SPs fall to the right of the light line with a larger wavevector than light waves traveling over the surface. As a result, SPs are non-radiative and represent surface electron density fluctuations. SPs, which are characteristic of surface waves, have their maximum intensity near the surface, and their electromagnetic field decays exponentially in the direction perpendicular to the surface. The electron oscillations cannot propagate in nanoparticles, and they do not display a dispersion relationship, only a resonance frequency.

1.4. Surface plasmons in the metallic nanostructures

For the case of metallic nanoparticles whose size is substantially smaller than the wavelength of the incident light, the electromagnetic field exerts a force on the conduction electrons, causing them to move towards the NP surface, as shown in Fig. 1.2. Therefore, an electric dipole is formed when a negative charge accumulated on one side and a positive charge accumulates on the other. This dipole creates an electric field inside the nanoparticle opposite to that of light, which acts as a restoring force to the equilibrium position. This is similar to the situation with the linear oscillator. When electrons are displaced from their equilibrium position and when the light field is removed, they oscillate at a frequency known as resonance frequency (plasmonic frequency), which for most transition metals falls in the ultraviolet-visible spectrum [1]. Because of the scattering process between the ionic cores and the nanoparticle surface, the electrons suffer damping during their movements, resulting in a condition similar to a damped

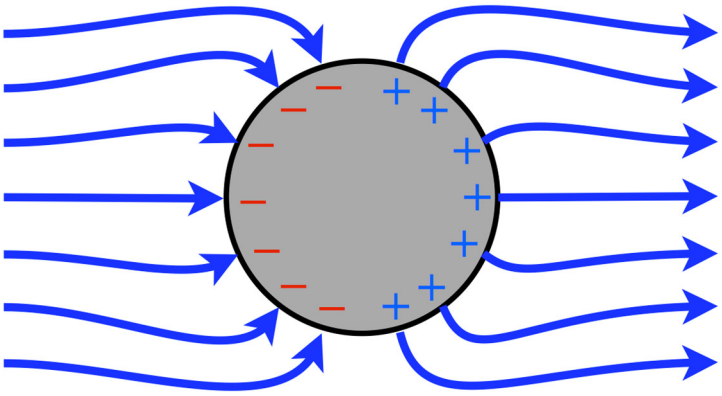

Figure 1.2. When nanoparticles are illuminated by the incident light, the electric field displaces the free electrons resulting in a charge accumulating at the surface of nanoparticle. This charge produces an opposing restoring field to that of the light, which forces electrons towards to their equilibrium positions.

oscillator, reducing the oscillation amplitude [1], [3]. Therefore, metallic nanoparticles exhibit absorption bands in the optical spectrum that are associated with the SPs.

1.5. Properties of surface plasmons in metallic nanostructures

The frequency (i.e., absorption maximum or colors), bandwidth, and intensity of LSP absorption bands are all characteristics of the type of material. Furthermore, the size, distribution, shape, surrounding medium, and interaction effects of metallic nanoparticles are all very sensitive to these absorption bands [22], [23].

- **Size effects**

The size of the nanoparticle has a direct impact on the surface plasmon resonance (SPR), with two different size ranges: smaller nanoparticles less than 50 nm in diameter, where the nanoparticle absorbs most of the energy, and larger nanoparticles, where scattering effects dominate the nanoparticle response [14], [23].

When the size of homogeneous spherical nanostructures is similar to the incident wavelength of light (for NPs smaller than 50 nm), the nanoparticles feel the electromagnetic field, and the charge displacement is generally uniform. A dielectric dipole can thus be used to explain the nanoparticles. Only one resonance band is observed in this situation. Parameters such as the width and intensity of the surface plasmon resonance are directly affected by the nanoparticle size, although the effect on the

resonance frequency is minimal [2], [22], [23].

The damping of electron oscillations is thought to be responsible for the size effect. When SPs are excited, scattering with the ionic cores and the surface slows down the movement of the electrons. The relationship between the nanoparticle size and the full width at half maximum (FWHM), Γ, of the surface plasmon resonance band can be expressed as follows:

$$\Gamma = a + \frac{b}{R} \tag{1.1}$$

where a and b denotes the material-dependent constants and R is the radium of the nanoparticle. The fraction of electrons in the shell close to the surface represents a smaller fraction of the oscillating electrons as the nanoparticle size increases, reducing the total effective damping. Moreover, the FWHM is inversely proportional to the radius of the nanoparticle.

- **Shape effects**

The shape of the nanoparticle has a big impact on the SPR. There are three plasmon resonances for metal nanoellipsoids, which correspond to the oscillation of electrons along the three axes of the nanostructures. Because the resonance frequency is determined by the orientation of the electric field relative to the nanoparticles, the SPR of nanostructures can be easily tuned by changing the axes' length. Nanorods, for example, have two equal axes, and therefore the charge accumulation at the surface of the nanoparticle will be different for electron oscillations along the longitudinal direction than in the perpendicular direction. The SPR of transversal plasmons in nanorods is similar to that of spherical nanoparticles (at slightly smaller wavelengths), whereas the resonance of longitudinal plasmons shifts towards a longer wavelength as the ratio of nanorods increases.

- **Medium effects**

The SPR is affected by the surrounding medium in addition to the characteristics of the nanoparticles, with the dielectric function of the surrounding media increases, the plasmon resonance moves towards larger wavelengths, as Fig. 1.3 illustrates. The bandwidth is restricted by the surrounding media, which is mostly determined by the nanoparticle size and the size distribution [1]. Moreover, for the resonant condition of $\varepsilon_1 = -2\varepsilon_d$, the plasmon resonance intensity relies on both the dielectric of the surrounding medium and the imaginary part of the

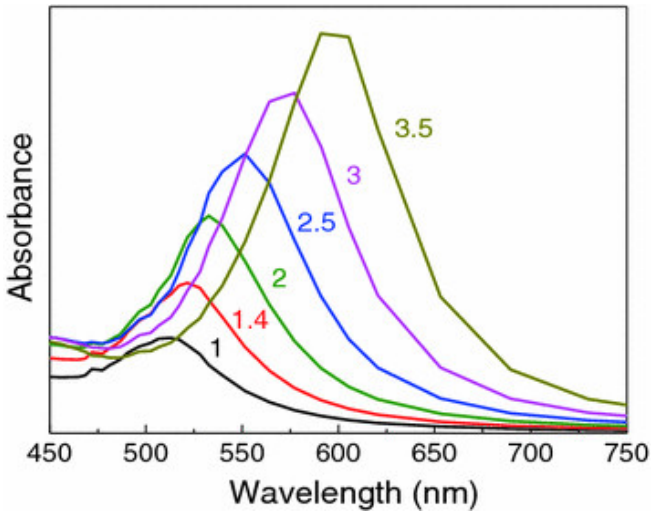

Figure 1.3. The absorption spectra of Au nanoparticles with the dimension of 10 nm with different dielectric function of the surrounding medium.

dielectric function of the metallic nanoparticles, according to the approximation dipolar equation for small nanoparticles. The resonance intensity band of Au increases, as seen in Fig. 1.3, with increasing the dielectric function of the surrounding medium.

- **Interaction effects**

When disordered nanoparticles are close enough, the local field at the nanoparticle is composed of the external incident light along with the field generated by the rest of the nanoparticles. The field generated by the nanoparticle decays over nanometer-scale distances. The field created by the nanoparticle in the rest is not uniform, resulting in non-uniform charge distributions inside the nanoparticle and further damping of electron oscillations. Interparticle interaction, in general, shifts the resonance peak of SPs to a larger wavelength and increases the FWHM [24], [25]. Therefore, it is feasible to produce controlled electromagnetic field interferences that allow extra tuning of the SPR in the case of arranged nanoparticles with particular geometries [26].

1.6. Surface plasmons in metallic films

As previously mentioned for the metallic film, SPs are oscillating waves of free electrons that are traveling across the interface between metal and dielectric layers. This $p-$

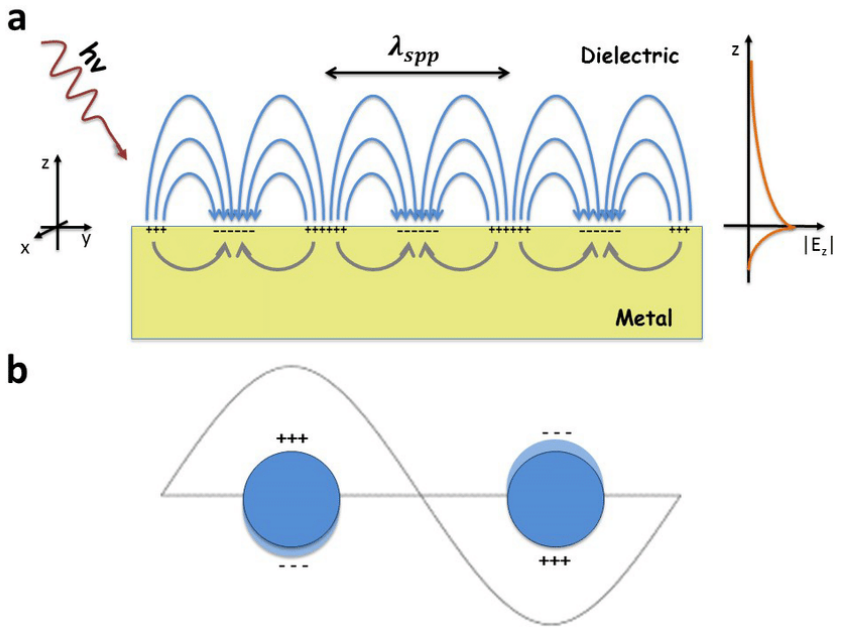

Figure 1.4. Schematic diagram representing the excitations of surface plasmon (SPs) at the interface between a dielectric and a metal mediums.

polarization or magnetic transversal electromagnetic waves are coupled with waves that move perpendicular to the metal/dielectric layers and decay exponentially into both mediums, as shown in Fig. 1.4. At the metal/dielectric mediums, the field amplitude of SPs reaches its maximum. Surface plasmon polaritons (SPPs) are defined as SPs that are coupled to electromagnetic waves [1].

1.7. Evanescent waves

Electromagnetic waves that travel along the interface between two different dielectric constants are known as evanescent waves. These waves propagate through the surrounding [27]. To fully understand the excited SPs, a mathematical explanation of evanescent waves is required [27]. An electromagnetic plane wave propagating in a medium with a specific refractive index can be described as the electric field (E) if the component is complex [1].

$$E = E_0 e^{(i\omega t - i\vec{k}.\vec{r})} = E_0 e^{(i\omega t - ik_x x - ik_y y - ik_z z)} \quad (1.2)$$

here, E_0 is the electric field amplitude, ω is the angular frequency, and r is the position

vector. The wavevectors propagation direction is parallel to that of the electromagnetic waves, so that:

$$k^2 = k_x^2 + k_y^2 + k_z^2 = (n\frac{2\pi}{\lambda})^2 = (n\frac{\omega}{c})^2 \quad (1.3)$$

where c is the speed of light in vacuum, λ is the wavelength. Considering the system is $2-$dimension with $k_y = 0$ and the electromagnetic wave is propagated at the interface between two different media with refractive indexes of n_1 and n_2, using the Snell's law and Eq. 1.3, the wavevector (k_{z2}) component perpendicular to the interface of the media can be given as:

$$k_{z2}^2 = n_1^2 \left(\frac{2\pi}{\lambda}\right)^2 \left(\frac{n_2^2}{n_1^2} - sin^2\theta\right) \quad (1.4)$$

Only longitudinal waves ($p-$polarization) propagating perpendicularly and decaying exponentially at the interface of medium 2 when Eqs. 1.2 and 1.4 are taken into consideration. The term evanescent field refers to this type of field (shown in Fig. 1.5) [1], [27].

$$E_2 = E_0 e^{-ik_z} e^{i(\omega t - k_x x)} \quad (1.5)$$

1.8. The dispersion diagram of surface plasmons

The dispersion diagram can be defined as the relationship between the angular frequency (ω) and the wavevector (k). For the interference between two different media (as shown in Fig. 1.5) a set of evanescent wave solutions necessary to obtain. Therefore, using Eqs. 1.4 and 1.5, the evanescent waves propagate through the first medium (dielectric) and second medium (metal) can be obtained based on the following expressions [3], [27].
For the first medium:

$$E_1 = E_0 e^{(k_x^2 - \varepsilon_1 \frac{\omega^2}{c^2})^{1/2} z} e^{i(\omega t - k_x x)} \quad (1.6)$$

For the second medium:

$$E_1 = E_0 e^{-(k_x^2 - \varepsilon_2 \frac{\omega^2}{c^2})^{1/2} z} e^{i(\omega t - k_x x)} \quad (1.7)$$

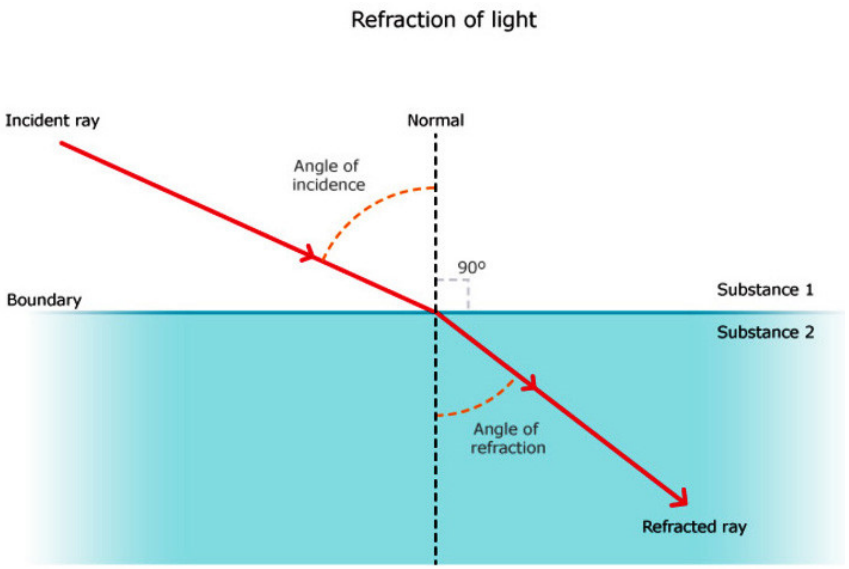

Figure 1.5. Schematic diagram illustrating the refraction of light at the interface between two different media with refractive indexes of n_1 and n_2 at the incident angle θ.

In order for evanescent waves to decay exponentially along the propagation directions, terms $(k_x^2 - \varepsilon_1 \frac{\omega^2}{c^2})^{1/2}$ and $(k_x^2 - \varepsilon_2 \frac{\omega^2}{c^2})^{1/2}$ must be positive. At $z = 0$, the boundary conditions require that the tangential components of the electric and magnetic fields to be continuous. Therefore, the following expression is necessary to satisfy:

$$(k_x^2 - \varepsilon_1 \frac{\omega^2}{c^2})^{1/2} = -(k_x^2 - \varepsilon_2 \frac{\omega^2}{c^2})^{1/2} \tag{1.8}$$

This expression can only be valid when $\varepsilon_2 < 0$ (i.e., a metal), and therefore the dispersion relation for surface plasmons can be expressed as follows:

$$k_{SP} = \frac{\omega}{c} \sqrt{\frac{\varepsilon_1 \varepsilon_2}{\varepsilon_1 + \varepsilon_2}} \tag{1.9}$$

where, ε_1 and ε_2 are the permittivity's of the first and second medium, respectively. The dispersion equation is only valid when $|\varepsilon_2| < \varepsilon_1$. When the first medium is air ($\varepsilon_1 \approx 1$) and the second medium is a metal, the dielectric function for free electron gas for the case of metals can be given as:

$$\varepsilon_2(\omega) = 1 - \left(\frac{\omega_p}{\omega}\right)^2 \tag{1.10}$$

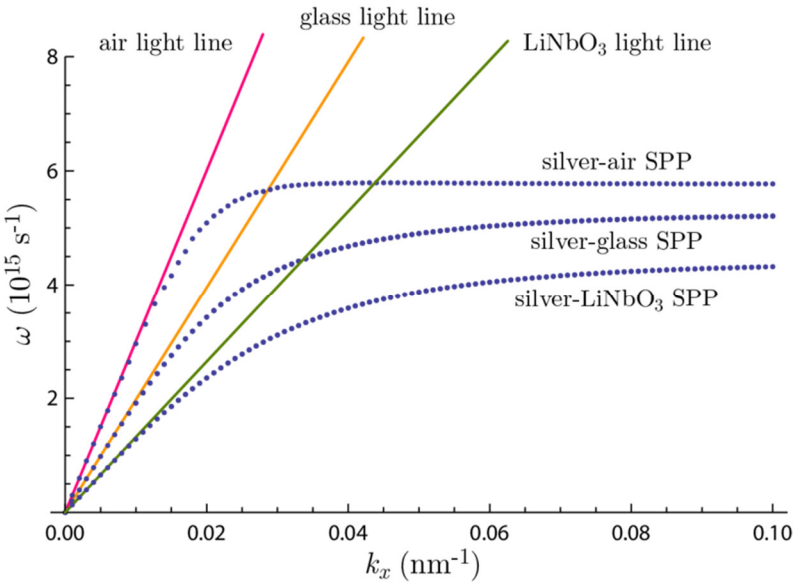

Figure 1.6. Dispersion diagram relations for air, dielectric medium (silver and $LiNbO_3$) and SPs at the interface between two different mediums. It is important to note that the SP for the case of silver-$LiNbO_3$ does not cross with that of light. As a result, SPs cannot be excited by light propagations.

here, $\omega_p^2 = \frac{ne^2}{\varepsilon_0 m}$ denotes the plasma frequency for the free electron gas [21].

Using the dielectric function for the free electron gas [$\varepsilon(\omega) = 1 - \frac{\omega_p^2}{\omega^2 + i\gamma\omega}$] and Eq. 1.9, the frequency of SPs approaches the characteristic of surface plasmon frequency as follows:

$$\omega_{SP} = \frac{\omega_p}{\sqrt{1+\varepsilon_2}} \tag{1.11}$$

As shown in Fig. 1.6, when $k_x > 0$, SPs propagate along the interfaces of metal and dielectric placing on the right side of the dispersion diagram for light in the air ($\omega = ck_x$). SPs cannot transform into light when $\omega < \omega_p/\sqrt{1+\varepsilon_1}$, and they are non-radiative waves that propagate along the surfaces. For the case when $\omega > \omega_p$, the wavevectors generally take real values and thus the SPs radiate out of the surface and they are called radiative SPs.

1.9. Propagating length and penetration depth of surface plasmons

Due to the significant losses in the metals, SPs can propagate with a high attenuation in

the visible and near-infrared spectrum. Because the electromagnetic field distribution is asymmetric at the interface, the field is primarily concentrated in the dielectric [1], [3]. Therefore, the SPs can propagate along with the interface between the metal and dielectric interface around a few micrometers at the visible and near-infrared wavelengths. The following expression determines the SPs propagated along the dielectric/metal interfaces [1], [3]:

$$L_{SP} = \frac{1}{2Im\ (k_{SP})} \tag{1.12}$$

where $Im(k_{SP})$ shows the imaginary part of the SPs wavevector. The sensitivity of the evanescent field can be explained by the penetration depth or decay length. Only changes in dielectric characteristics at the dielectric/metal interfaces will have an effect on the evanescent field [27]. As clearly demonstrated in Fig. 1.7, the decay of the SPs into the metal is significantly shorter than the dielectric, which is completely dependent on the resonance wavelength. The penetration depth of the dielectric medium is on the order of $\frac{\lambda}{2}$ whereas the penetration depth of metal is a few nanometers, which is close to the skin depth [28]. Therefore, the penetration depth for the first (dielectric) and second medium (metal) can be calculated as follows:

For the first medium:

$$\delta_{SP1} = \frac{1}{k_{z1}} = \frac{c}{\omega}\sqrt{\frac{\varepsilon_1 + Re(\varepsilon_2)}{\varepsilon_1^2}} \tag{1.13}$$

For the first medium:

$$\delta_{SP2} = \frac{1}{k_{z2}} = \frac{c}{\omega}\sqrt{\frac{\varepsilon_1 + Re(\varepsilon_2)}{Re(\varepsilon_2)^2}} \tag{1.14}$$

here $Re(\varepsilon_2)$ denotes the real part of the permittivity of the metal.

1.10. Excitation of surface plasmons at the planar interfaces

Electron or light can excite SPs. However, the excitation of SPs using light is experimentally more cost-effective. Since the dispersion diagram of SPs and the incident electromagnetic waves (light) in air do not intersect, and therefore SPs cannot be excited

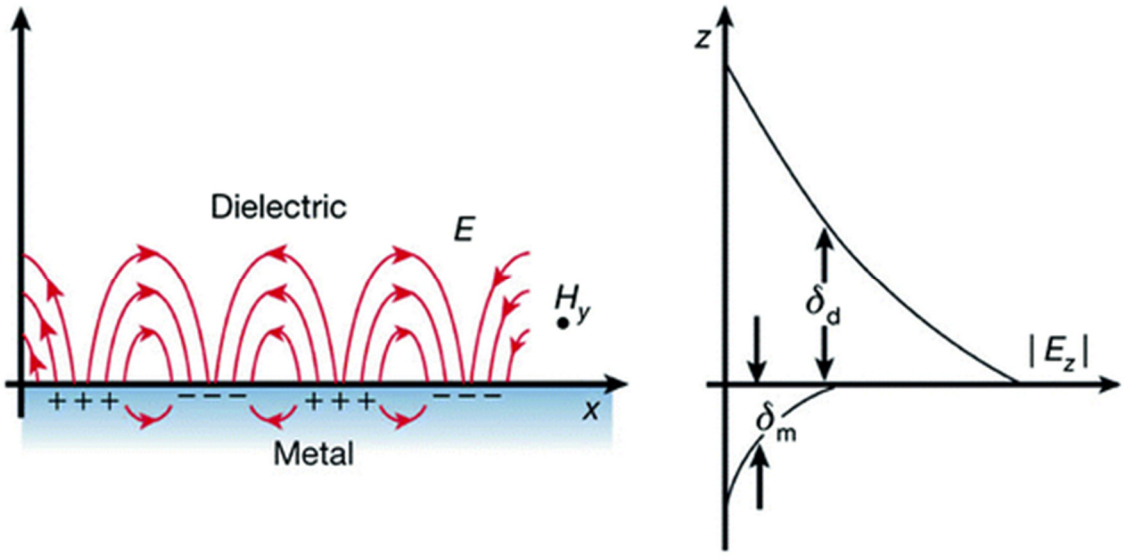

Figure 1.7. The schematic diagram of SPs. The right panel shows the penetration depth of SPs at the interfaces between the dielectric/metal. Figure adapted from Li. L [29].

when light is incident from air. Furthermore, when it is essential to illuminate the interfaces of metal/air at an angle, the problem becomes considerably difficult, since the wavevector of light in the plane must be multiplied by $sin\theta$ ($k_x = ksin\theta$). As a result, direct excitation of SPs from the air is not practical, and many experimental approaches have been devised to provide wavevector conservation such as prism coupling [17], [29], grating coupling [10], [14], and waveguides using subwavelength holes [30], [31] are widely utilized to detect SPs.

- **Prism Coupling**

As mentioned above, SPs at the interface of metal/dielectric cannot be directly excited by the incident light beam from the air, since the dispersion diagram of SPs and that of the evanescent wave of the incident field do not cross. However, a three-layer structure consists of a thin metal layer sandwiched between two different dielectric constants can achieve phase matching to SPs. For the sake of simplicity, we will assume that one of the dielectric constants is air ($\varepsilon \approx 1$). A beam that is reflected at the interface between the higher dielectric constant, generally in the shape of a prism. Thus, the metal has an in-plane momentum ($k_x = ksin\theta$), which is sufficient to create SPs at the metal/dielectric interface. The excited SPs cause a decrease in the intensity of the reflected beam. Since

the excited SPs dispersion is beyond the prism light cone, phase matching conditions of SPs at the prism/metal interface is not possible. There are also several ways to excite SPs with the incoming light beam utilizing prism coupling. When the refractive index is higher than air ($n > 1$). The Otto [17], Kretschmann Raether [16], and Sarid [32] configurations are the most common configurations to detect SPs. The ATR is utilized in these configurations as a high-refractive-index medium in a prism that is located close to the metal surface. ATR is a method that creates evanescent waves by using total internal reflection. The use of prism results in the coupling of the evanescent waves and the SPs, which are created at the interface of prism/metal by total internal reflections. The produced evanescent waves can travel from the prism to the metal/dielectric interface, where the SPs are excited as demonstrated in Fig. 1.6, showing that the resonance condition can be satisfied when:

$$k_{SP} = \frac{\omega}{c} nsin\theta = \frac{\omega}{c}\sqrt{\frac{\varepsilon_1 \varepsilon_2}{\varepsilon_1 + \varepsilon_2}} \tag{1.15}$$

It is possible from the above equation to calculate the incident angle between the incident light and the excited SPs as:

$$\theta_{SP} = arcsin\theta \sqrt{\frac{\varepsilon_1 \varepsilon_2}{(\varepsilon_1 + \varepsilon_2)\varepsilon_p}} \tag{1.16}$$

As clearly discussed above, the Kretschmann technique, which involves evaporating a thin metallic film on the top of the glass prism, is the most prevalent configuration for the excitation of the SPs. The SPs are excited at the interface of metal/air when photons from the source light is incident to the glass at an angle greater than the critical angle of the internal reflection tunnel into the metal layer. The other geometry (Otto configuration), where a small air gap separated the prism from the metal layer. At the interference of the prism/air, total internal reflection occurs, and the SPs excite at the air/metal interface. When direct contact within the metal surface is undesired, this configuration is preferred.

- **Grating coupling**

Figure 1.8 demonstrates how SPs can be excited by using a grating pattern on the metallic surface. The excited SPs can propagate through the interface between metal and dielectric layers with a definite refractive index since the metal surface at the grating pattern

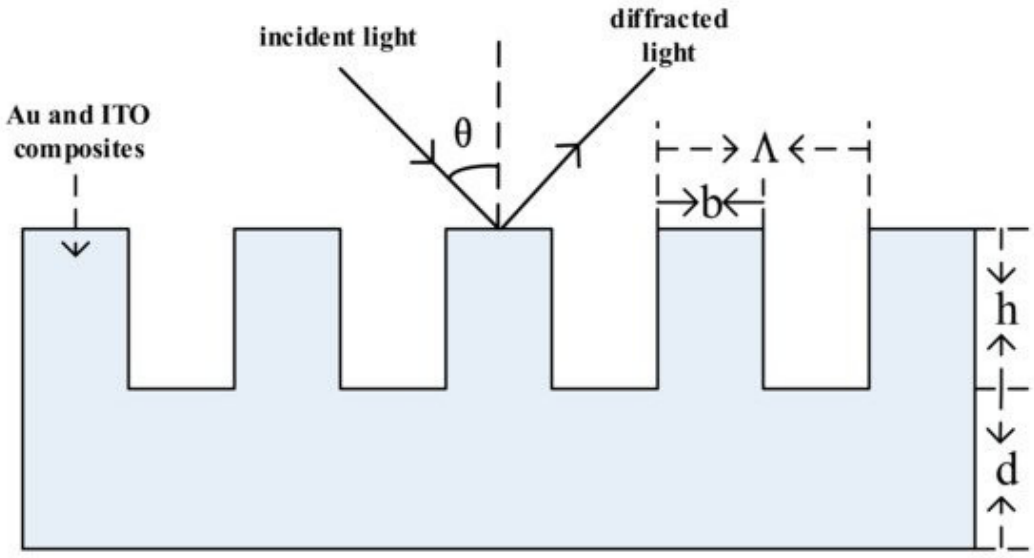

Figure 1.8. Phase matching of the incident light with the wavevector using a metallic grating surface. Figure adapted from Li.W et al [34].

corresponds to a superposition of various gratings [33]. Therefore, as depicted in Fig. 1.8 for the case of 1 −dimensional grating structure, the phase-matching conditions can be satisfied when:

$$k_{SP} = nksin\theta \pm mG \tag{1.17}$$

here $m = 1,2,3,$ ... and $G = \frac{2\pi}{a}$ is the reciprocal of the grating, and b is the lattice constant of grating.

1.11. The future of surface plasmons on plasmonic structures

Nowadays, SPs are widely utilized in the fields of energy [35], [36], nanophotonics [37], [38], sensors [39]–[41], and environments [42], [43]. Although SPs have been discovered for more than a century, the number of publications on this subject has recently increased dramatically. This is due to the development of powerful techniques for the fabrication of nanostructures and the ability to control the light at the subwavelength scale [44]. Moreover, the combination of SPs with metamaterials results in a number of advantages, making plasmonic structures a potential candidate for investigating complicated optical phenomena and novel applications. To begin with, the local field enhancement leads to greater light-matter interaction, allowing numerous weak processes to be improved and exploited more efficiently. Second, the field confinement and rapid optical process allow

for the fabrication of small devices that can serve as a bridge between photonic and electrical components. Third, by changing the responses of individual components and their coupling, plasmonic structures' spectra can be well-tuned. In virtually all practical applications, this is very desirable. Because of these appealing characteristics, plasmonic structures are likely to have broad applications. Therefore, the following areas are mainly unexplored and deserved particular attention.

- **Nonlinear optics in plasmonic structures**

If nonlinear materials are embedded in plasmonic nanostructures, the large local field can offer a significantly enhanced nonlinear process. Furthermore, the metal has a high nonlinearity property, which can be enhanced further by texturing its surface. It is also demonstrated that strong magnetic resonance, which is usually overlooked has the potential to significantly improve the nonlinear optical properties [45]. An alternative technique based on phase conjugation from a thin nonlinear layer has been suggested for negative refraction [46]. Four-wave mixing in nanostructure metallic films and graphite thin films were used to show experimentally in the microwave and visible ranges, respectively [47]–[49]. Tunable metamaterials, ultrafast switching, and optical modulations are all possible thanks to these fascinating phenomena and advances [50]–[52].

- **Expanding the properties of plasmonic structures towards quantum physics**

To explore plasmonic field enhancement at such tiny scales, new theories based on non-locality and quantum models have been established. Furthermore, the high photonic density of states in metamaterial structures allows for more interaction with the quantum emitter, while also manipulating light into a sub-diffraction single-photon resonance [53]. These research findings in the realm of quantum plasmonic and quantum metamaterials will help us better understand the underlying physics of SPs in metamaterials, and enable the fabrication of innovative quantum and electronic devices such as transistors, sensors, and single-photon emitters [54]–[56].

- **Dynamically control of plasmonic structures**

Although modulation of subwavelength properties in the optical region is so difficult, substantial progress has been made in this area. The use of graphene [57], [58], phase-change materials (PCM) [59], [60], and liquid crystals [61], [62] offer possible solutions.

Plasmonic metamaterials working in a fluidic environment, in particular, have the potential to achieve reconfigurability and numerous applications. Moreover, laser-induced surface bubbles have recently been utilized to control the propagation of SPs. Divergence, collimation, and controlling of SPs are all achieved by such plasm fluidic lenses by carefully regulating the size, position, and the form of surface bubbles [63]. In conclusion, research and development are recently being conducted to combine the SPs technology into a variety of fields to make use of the SPs distinctive characteristics [27]. This phenomenon may now be combined into other methods and utilized to investigate a variety of systems duo to the advancement of the SPs technology. Although the field of plasmonic fast expansion in recent years, there is still a lot of works that need to be done.

1.12. Thesis Outline

This thesis is divided into six chapters. This chapter reviews the concept of the excitation of surface plasmons in nanoparticles and metallic films, the current status of SPs, and the future of SPs in plasmonic structures. In the next chapter (chapter 2), we propose a metamaterial perfect absorber (MPA) with dual-band functionality that absorbs light in the visible and near-infrared (NIR) ranges. The proposed design consists of a periodic array of self-aligned hybrid indium tin oxide (ITO)-Au split ring resonator. The simulated results indicate that a narrowband perfect absorption at the resonance wavelength of 773 nm and a broadband absorptive characteristic in the NIR region can be successfully obtained. The proposed design can find potential applications in selective thermal emitters and sensors. In chapter 3, we design a MPA with dynamic thermal tuning that can control the absorption of the resonances. The proposed MPA comprises a silicon (Si) nanograting on a silver (Ag) to have multiple resonances in the NIR region. The insertion of a thin VO_2 film into the design enables the design to act as an on/off switch and resonance tuner. Therefore, the proposed structure can provide multi-resonance features to cover a broad range and can find promising applications to design linearly thermal-tunable and broadband MPAs. Chapter 4 presents the design of a wavelength-selective nanoantenna emitter based on the excitation of gap-surface plasmon resonances (GSPs) for satisfying multiple thermal infrared applications. The proposed design (design I) realizes triple

narrowband perfect absorptions, which perfectly match the atmospheric absorption windows, while maintaining relatively low emissivity in the atmospheric transparency windows. Later, we extend the functionality of design I to include a broadband absorption at the NIR region to minimize the solar irradiation reflection from the nanoantenna emitter. In chapter six, we present a narrow-band optical diode device with a high forward-to-backward ratio at the NIR region. The structure is composed of a 1 −dimention grating on top of a dielectric slab waveguide of silicon nitride (Si_3N_4), which is deposited over an Ag thin film. The design has a forward transmission of about 88%, and a backward one of less than 3%. Chapter 6 presents a conclusion on the thesis.

CHAPTER 2

Hybrid indium tin oxide-Au metamaterial as a multiband bi-functional light absorber in the visible and near-infrared ranges

This chapter is one part reprinted with permission from: **Ataollah Kalantari Osgouei**, Hodjat Hajian, Andriy, E. Serebryannikov, and Ekmel Ozbay, Journal of Physics D: Applied Physics, 2021, 54(27), 275102.

2.1. Introduction

Metamaterials are engineered structures that exhibit extraordinary electromagnetic properties not available in nature [64], [65]. They can be employed to achieve various intriguing phenomena such as invisible cloaking [66], asymmetric light transmission [67], lasing [68], and negative refraction [69]. Light absorption is another extraordinary potential capability of these artificial structures [70]. Metamaterials with nearly perfect

absorption features are generally called metamaterial nearly perfect light absorbers (MPAs). In 2008, Landy et al. proposed a narrowband MPA based on metallic split ring resonator arrays [71]. Thereafter, considerable attention has been paid in research focusing on MPAs by many research groups during the past years. Depending on the geometry and the material type being employed in the MPA structures, their absorptive responses can be categorized as narrowband or broadband. The former category may have applications in sensing [72], imaging [73], and color filtering [74] while the latter category can be functionalized in photodetectors [75], solar cells [76], radiative coolers [77], and photochemical devices [78]. Such electromagnetic nearly perfect light absorbers have been reported in various frequency ranges that cover the visible [79], [80], near-infrared (NIR) [81], [82], mid-infrared (MIR) [83], [84], far-infrared (FIR) [85], [86], terahertz [87], [88], and microwave regions [89]–[91]. In order to physically realize MPAs, as a strategy, reflectance can be suppressed by matching the effective impedance of the metamaterials with the surrounding medium. At the same time, transmission may be eliminated by employing an optically thick metal layer acting as a mirror [92], [93]. Therefore, one of the widely used approaches to obtain nearly perfect light absorption is to employ a metal-insulator-metal (MIM) configuration. Based on this structure, narrowband perfect absorption can be obtained for which the top layer of the MIM is either unpatterned [94] or patterned [95]. On the other hand, it is also possible to obtain broadband perfect absorption by employing either lossy materials like Ti [96] as a top patterned layer or using multidimensional objects in the top layer of each unit cell of the metamaterial [97], [98]. In addition to the aforementioned structures that exhibit either narrowband or broadband responses, the MPAs with dual-narrowband functionality, which are absorptive in two different narrow wavelength regions and almost reflective in other bands have been widely studied by employing a single type of material on the top layer of the MIM structure [99]–[101]. Such designs are found to have practical applications in selective photonic structures, sensors and optoelectronic devices. The idea behind those designs is to employ meta-atoms based on a single type plasmonic material (e.g. Au) with different geometrical shapes. On the other hand, as a different approach, by hybridizing graphene as a plasmonic material and hexagonal boron nitride as a phononic material, MIR MPAs with multi-narrowband resonant responses have been obtained

[102], [103]; i.e. employing diverse functional materials to achieve responses with different functionalities. However, to our knowledge, a hybrid MPA with meta-atoms composed of different plasmonic layers that represents narrowband responses in the visible and broadband feature in the NIR has not been reported.

In this paper, we propose a hybrid nearly perfect light absorber that is capable of functioning as a narrowband light absorber at $773\ nm$ ($FWHM{\sim}60\ nm$) in the visible and at $900\ nm$ ($FWHM{\sim}49\ nm$) in the NIR range [see Fig. 2.5(b)], where $FWHM$ stands for full width at half maximum. Moreover, the proposed metamaterial can operate as a broadband MPA within $1{,}530\ nm$ to $2{,}700\ nm$ in the NIR region; i.e. a bi-functional response is observed by the MPA. The top patterned layer of this novel metastructure is composed of array of self-aligned hybrid indium tin oxide (ITO)-Au split ring resonators (SRRs), that are separated from an optically thick bottom reflector with a SiO_2 layer. We first numerically evaluate the primarily obtained result by investigating how ITO and Au incorporate in the total absorption response of the metamaterial. Moreover, replacing an effective top layer with the hybrid array and employing transfer matrix method (TMM), the numerical results are also verified. As complementary investigations, the mode profiles at some frequencies inside the narrowband and broadband regions also confirm that Fabry-Perot (FP) and propagating surface plasmon (PSP) resonances are responsible for the bi-functional operation of the metastructure. Finally, by increasing the in-plane symmetry of the metamaterial, the polarization-independent and omnidirectional response of the device for transverse electric (TE) and transverse magnetic (TM) oblique incidences are also verified. Despite the considerable amount of research that have been done in the field of metamaterial light absorbers, we believe that this study can be of interest to readers and find potential applications in sensing, selective thermophotovoltaics and thermal emission.

2.2. Theoretical Background

In order to get more insight into the physical mechanism of the absorption responses of the designed metamaterial, we employ the effective medium theory (EMT) together with transfer matrix method (TMM) for a semi-analytic investigation of the numerically

obtained absorption. In this approach, an effective homogeneous layer is replaced with the top patterned layer of the MPA that is composed of an array of self-aligned hybrid ITO-Au SRRs. The schematic of the hybrid ITO-Au based metamaterial is schematically illustrated in Fig. 2.1(a). A unit cell of the MPA is also depicted in Fig. 2.1(c). As mentioned above, the metamaterial is composed of array of self-aligned hybrid ITO-Au SRRs that is separated by an optically thick gold reflector with an SiO_2 layer with thickness of t_{SiO_2}. The ITO and Au layers thicknesses in each self-aligned SRR are also introduced as t_{ITO} and t_{Au}. In the following we consider $t_{eff} = t_{ITO} + t_{Au}$. The chosen values of the remained geometrical parameters of the unit cell of the metamaterial are also highlighted in panel (c) of Fig. 2.1. In order to semi-analytically analyze absorption of the metamaterial, we employ the TMM approach on the layered medium that schematically shown in Fig. 2.1(b). In this layered structure, an effective isotropic and homogeneous medium is replaced with the top patterned ITO-Au layer, as seen from Fig. 2.1. Here, absorption is calculated as $A = 1 - R$ where A and R denote light absorption and reflection, respectively. It should be noted that since an optically thick Au layer is chosen as the bottom reflector in the calculations, transmission is zero ($T = 0$). Considering the $z-$component of the electric field as:

$$E_z(x) = \begin{cases} A_1 e^{-ik_1(z-t_{eff})} + B_1 e^{ik_1(z-t_{eff})}, z > t_{eff} \\ A_2 e^{-ik_2 z} + B_2 e^{ik_2 z}, 0 < z < t_{eff} \\ A_3 e^{-ik_3(z+t_{eff})} + B_3 e^{ik_3(z+t_{eff})}, -t_{SiO_2} < z < 0 \\ A_4 e^{-ik_{Au}(z+t_{eff}+t_{SiO_2})}, z < -t_{SiO_2} \end{cases} \quad (1)$$

and imposing the boundary conditions at the interfaces [104], reflection of light can be obtained as $R = |M_{21}/M_{11}|^2$. Here, $k_i = \sqrt{(\frac{n_i \omega}{c})^2 - k_x^2}$ $(i = 1, \dots, 4)$ [see Fig. 2.1(b) where the layers are labeled by numbers], c is the speed of light, n_i is the refractive index of each medium, and

$$M = \begin{bmatrix} M_{11} & M_{12} \\ M_{21} & M_{22} \end{bmatrix} = D_1^{-1} D_2 P_2 D_2^{-1} D_3 P_3 D_3^{-1} D_4. \quad (2)$$

Here

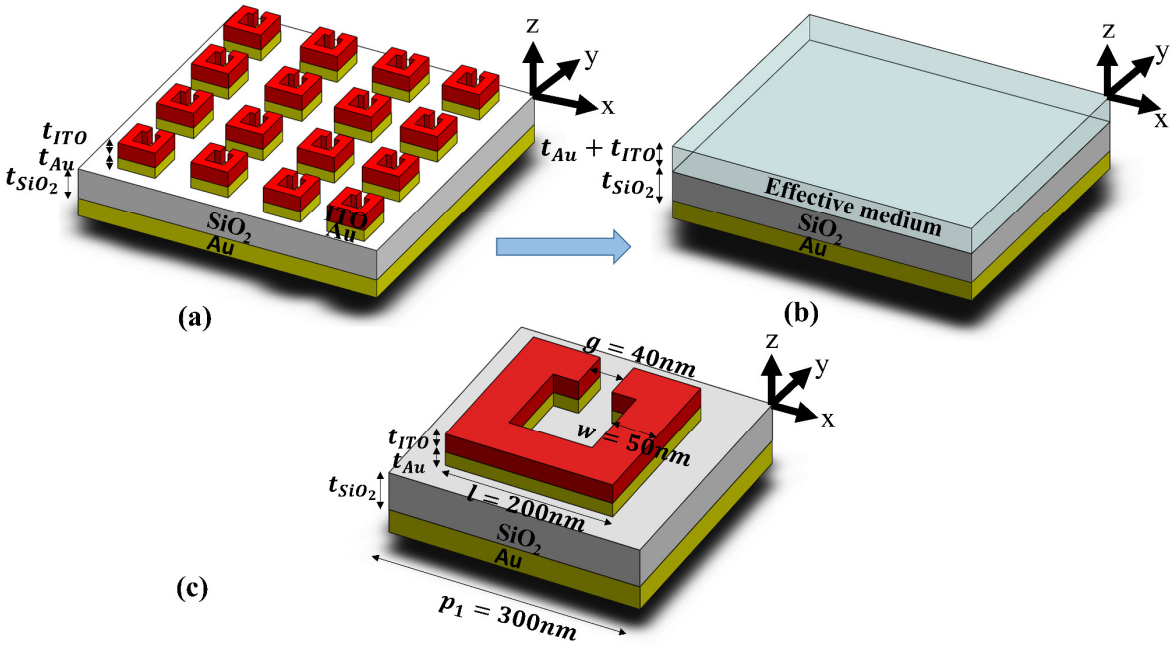

Figure 2.1. (a) Schematic of the self-aligned hybrid ITO-Au metamaterial nearly perfect light absorber. The unit cell of the metamaterial is depicted in panel (c). Panel (b) represents the optically equivalent model of the MPA shown in panel (a) in which the top effective medium layer is replaced by the self-aligned ITO-Au SRR array. The geometrical parameters and their corresponding are highlighted in panel (c). The values of the thicknesses of the layers are addressed in the text.

$$D_i = \begin{bmatrix} 1 & 1 \\ n_i & -n_i \end{bmatrix} \tag{3}$$

and the effect of light propagation through the effective medium ($n_2 = n_{eff}$) and the spacer layer ($n_3 = n_{SiO_2}$) are taken as the following propagation matrices into account

$$P_2 = \begin{bmatrix} e^{i\varphi_2} & 0 \\ 0 & e^{-i\varphi_2} \end{bmatrix}, \tag{4a}$$

$$P_2 = \begin{bmatrix} e^{i\varphi_3} & 0 \\ 0 & e^{-i\varphi_3} \end{bmatrix}. \tag{4b}$$

where $\varphi_i = n_i t_i \omega / c$ for the case of normal incidence. It is practical to replace a collection of periodically arranged scattering objects with subwavelength dimensions by a homogeneous medium. This homogenization approach, which is also called effective medium theory (EMT), can be valid as far as the applied fields are static or have spatial variations on a scale larger than the scale of the inhomogeneous medium [105]–[107]. Consequently, the effective refractive index of the effective medium in Fig. 1(b) can be retrieved using S_{11} and S_{21} scattering elements of normally incident reflected and

transmitted light. Due to the presence of the thick metallic substrate $S_{21} = 0$ and S_{11} will be calculated numerically [108].

2.3. Results and discussions

In this section, we investigate the absorption response of the MPA shown in Fig. 2.1 in a broad range of wavelengths covering the visible and NIR regions ($400\ nm$-$3{,}500\ nm$). Note that, considering the previously reported practical parameters of the SRR metamaterials [109]–[111], we performed geometrical parameter optimization simulations to obtain the following feasible parameter. Based on these parameters and employing nanofabrications techniques [112], [113], the suggested designs in this study can be experimentally verified. Therefore, the geometrical parameters shown in Fig. 2.1(c) are taken as $w = 50\ nm$, $g = 40\ nm$, $l = 200\ nm$, $t_{Au} = 60\ nm$, $t_{ITO} = 80\ nm$, $t_{SiO_2} = 160\ nm$, and $p_1 = 300\ nm$, unless stated otherwise. The thickness of the optically thick bottom reflector is also chosen as $500\ nm$ in the simulations. Refractive index of SiO_2 and Au are also selected based on experimental values [114], [115]. Moreover, following the experimental data [116], ITO has been taken into account using the Drude dispersion relation $\varepsilon(\omega) = \varepsilon_\infty - \omega_p^2/[\,\omega(\omega + i\gamma_p)]$, with the background permittivity of $\varepsilon_\infty = 3.91$, the plasma frequency of $\omega_p = 2.65 \times 10^{15}\ rad/s$, and collision frequency of $\gamma_p = 2.05 \times 10^{14}\ rad/s$. It is noteworthy that, for the FDTD simulations, the considered unit cell is excited with a plane wave, and periodic boundary condition (perfectly matched layer) is applied in the X-Y boundaries (Z boundaries). The simulated absorption of the MPA exhibits a narrowband perfect resonant peak at $767\ nm$ with a high quality factor($\sim$13, $FWHM \sim 59\ nm$) and a broadband perfect absorption spanning from $1{,}790\ nm$ to $3000\ nm$, as shown in the solid-blue curve in Fig. 2.2(a). More investigations prove that (results are not shown here) if the hybrid ITO-Au SRR array is replaced with an array of periodic hybrid ITO-Au disks with $r = 100\ nm$, two narrow absorption peaks in the visible and near infrared regions will be obtained. In other words, due to its geometrical characteristic, the metamaterial composed of the hybrid SRR array can more efficiently harvest the incident light in the NIR region to achieve broadband absorption response, as compared to an array of disks. Moreover, by further investigations

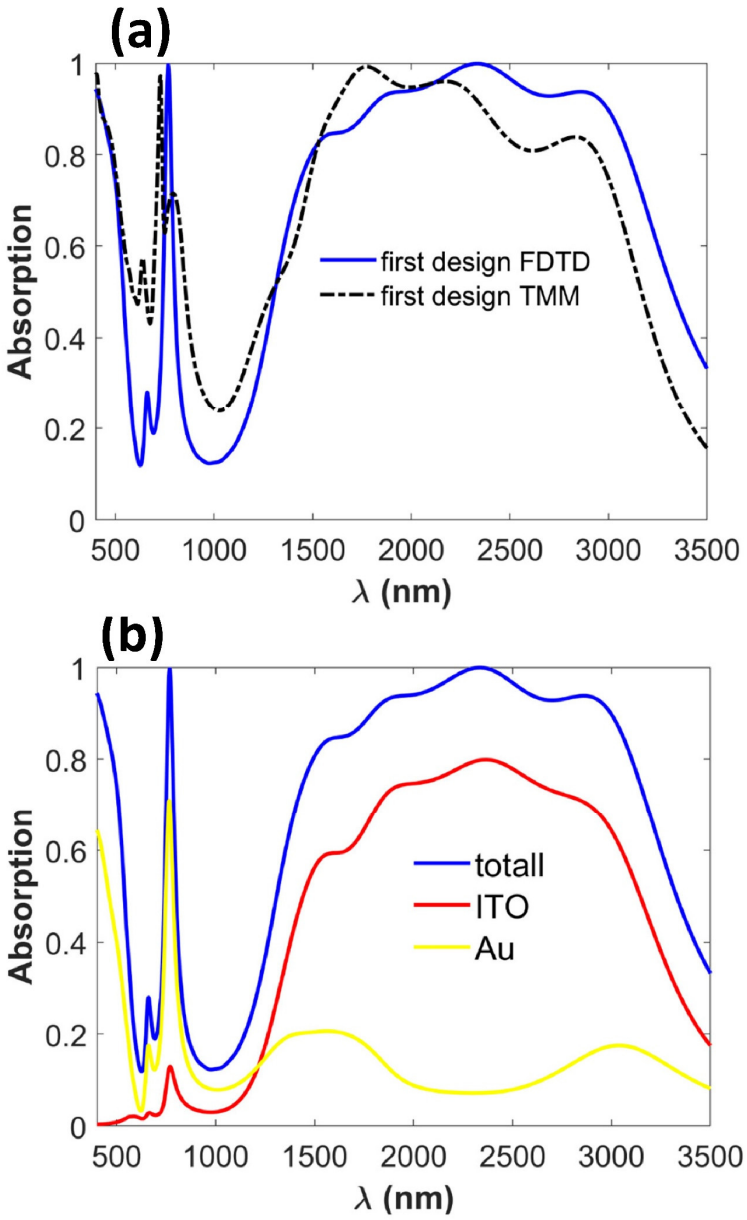

Figure 2.2. (a) Simulated normal incidence absorption spectra of the actual MPA (solid-blue) and the corresponding semi-analytical result based on the EMT and TMM. (b) Contribution of the ITO SRR and Au SRR in the total absorption of the self-aligned hybrid ITO-Au SRR. The results are obtained for normal incidence of light.

of the results we understood that for the case of $g = 40\ nm$, the NIR absorption response of the metamaterial is broaden than $g = 80\ nm$ and $g = 100\ nm$ cases. However, by removing the gap (i.e. $g = 100\ nm$) it is still possible to obtain a broadband NIR absorption.

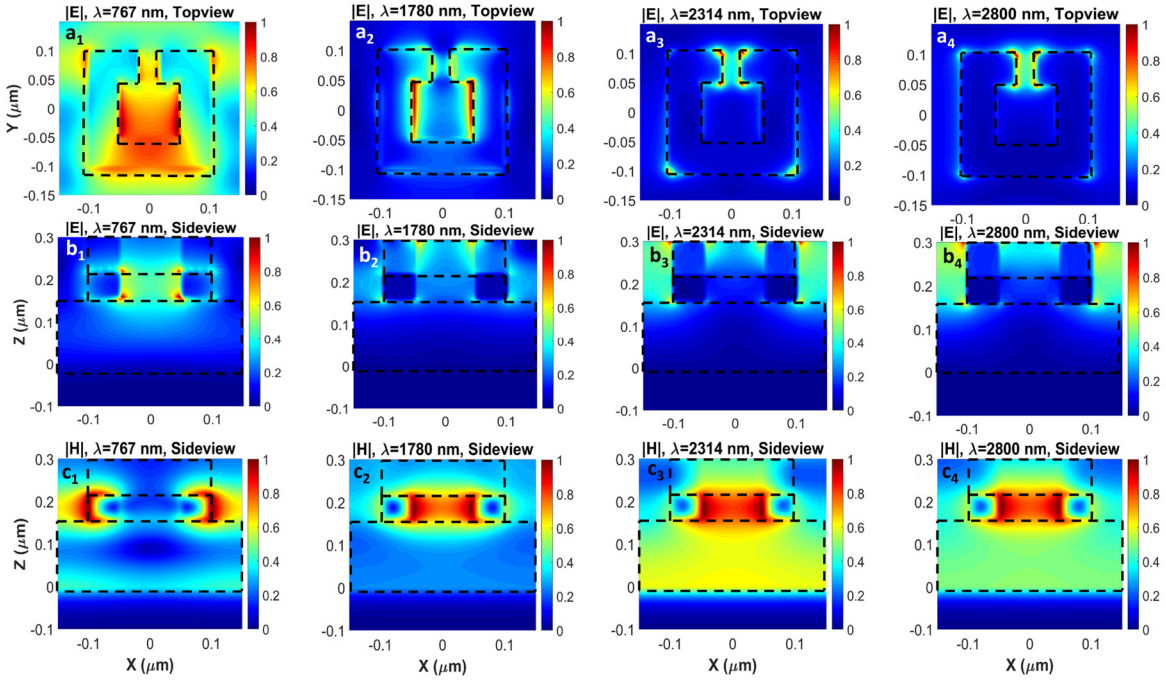

Figure 2.3. Panels (a_i), (b_i), and (c_i) [i=1,2,3], respectively, illustrate normalized values of the top-view $|E|$ mode profiles, side-view of $|E|$ and side view of $|H|$ at the narrowband resonant peak (767 nm) and the three different absorption resonances in the broadband region, namely 1,780 nm, 2,314 nm, and 2,800 nm. The dashed rectangles in panels (b_i) and (c_i) highlight the position of the ITO, Au and SiO_2 layers.

To understand the physical mechanism of the nearly perfect absorption responses of the structure, we employ the EMT together with the TMM on the layered structure depicted in Fig. 2.1(b). As mentioned earlier, in the semi-analytical approach, the effective refractive index n_{eff} of the hybrid ITO-Au SRR array with the effective thickness of t_{eff} are taken into account. The result is illustrated as the dashed-dotted black curve in Fig. 2.2(a) which fairly matches with the perfect narrow-band absorption wavelength. This agreement indicates the verification of the FP resonance by the applied approach. There is also an acceptable agreement between the semi-analytical and numerical result in the broadband region confirming that replacing a homogenized medium with the top ITO-Au patterned layer is justified for this case. However, the observed discrepancies between the semi-

analytical and the numerical results at $\lambda > 2250\ nm$ notifies that, at larger wavelengths, the PSP resonances are mostly responsible for the absorption response of the MPA that

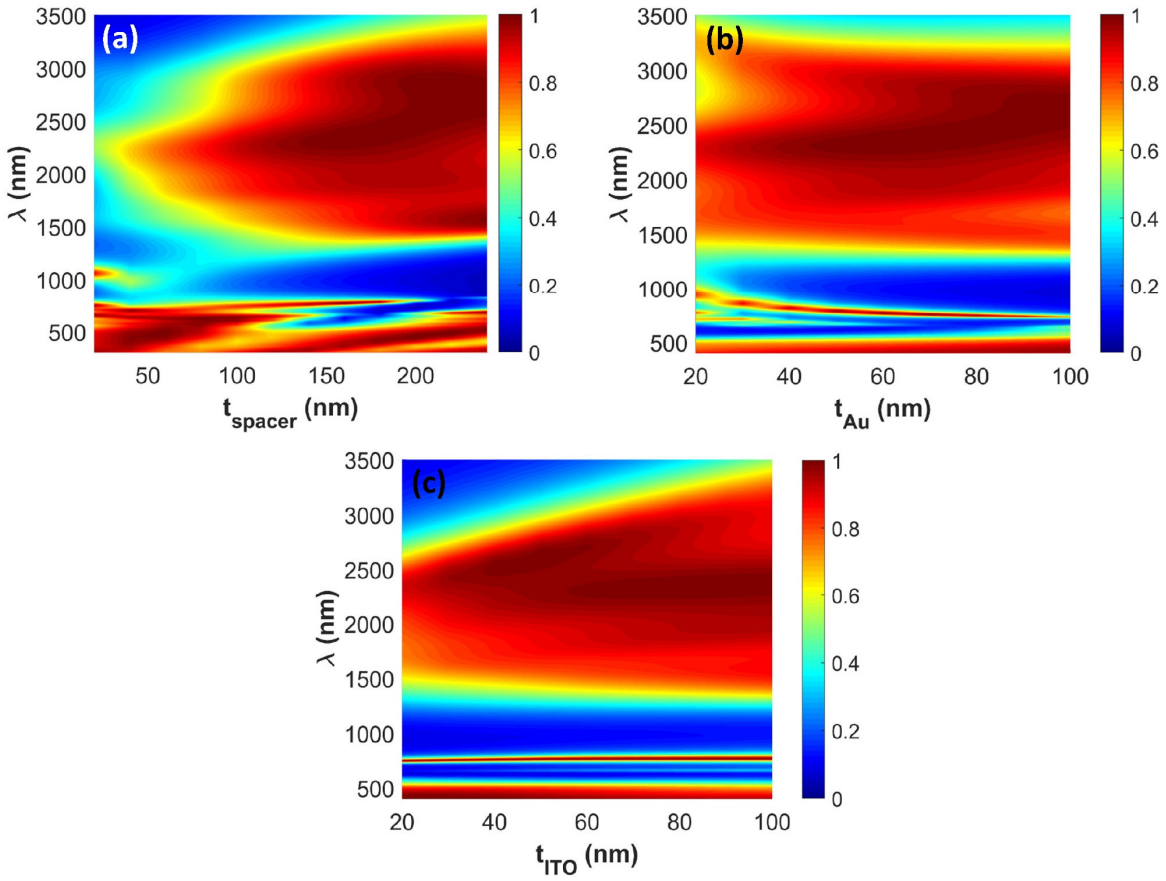

Figure 2.4. Absorption spectra of the MPA, that is schematically shown in Fig. 2.1, with respect to the thickness of spacer [(a)], thickness of the Au SRR [(b)] and thickness of the ITO SRR [(c)]. Note that in panel (a) $t_{Au} = 60$ nm and $t_{ITO} = 80$ nm, in panel (b) $t_{sio_2} = 160$ nm and $t_{ITO} = 80$ nm, and in panel (c) $t_{sio_2} = 160$ nm and $t_{Au} = 60$ nm.

are less captured by the homogenization approach. This point is clarified by examining the mode profiles in Fig. 2.3.

In order to achieve more understanding about the absorption mechanism of the hybrid ITO-Au SRR array, contribution of the ITO and Au SRRs in the total absorption of the hybrid

MPA is investigated in Fig. 2.2(b). The solid-yellow curve in this figure clearly highlights the role of gold, as a noble metal with moderate losses, in the appearance of the narrowband absorption resonance of the MPA at $\lambda = 767\, nm$. However, ITO has a minimum contribution in appearance of that resonance since it behaves as a low-loss dielectric material at the corresponding wavelength. On the other hand, once the solid-red

curve is compared to the total absorption of the MPA in Fig. 2.2(b), it is understood that ITO, that

can act as a lossy plasmonic material at $\lambda > 1420\ nm$, is responsible for the broadband response of the metamaterial absorber. It is observed that the hybridization of the ITO and Au SRR array in the final MPA eventually provides a nearly perfect narrowband resonant peak and a broadband absorption response in the NIR region.

Investigation of the mode profiles at the resonance wavelengths is also an effective tool to reveal the physical mechanisms behind the absorption characteristics of the proposed MPA. With this aim, electric and magnetic field profiles at the narrowband resonant absorption wavelength ($\lambda = 767\ nm$) and three resonant wavelengths in the broadband region, namely $\lambda = 1780\ nm$, $2{,}314\ nm$, and $2{,}800\ nm$, are shown in Fig. 2.3. Top-view of $|E|$, side-view of $|E|$, and side-view of $|H|$ at the resonant wavelengths are represented in panels (a_i), (b_i) and (c_i) of Fig. 2.3, respectively. The top- and side-view mode profiles of $|E|$ at $767\ nm$ [panels (a_1) and (b_1)] shows the electric field is mostly localized at the gap and between the edges of the SRR arms while from panel (c_1) it is seen that the magnetic field is mostly localized at the edges of the Au SRR array. This observation conveys that, at this wavelength, FP resonance is responsible for the narrowband perfect absorption. Panels (a_2) and (b_2) of Fig. 2.3 represent that the electric field at $1{,}780\ nm$ is localized between the arms of the ITO SRR while the magnetic field is captured in the gold region with weak interaction with the bottom reflector. This observation verifies that due to the localization of the electric field in the ITO SRR, which is a lossy material at that wavelength, a low-Q resonance is responsible for the absorption. The same point can be observed from the top- and side-view of $|E|$ mode profiles at $2{,}314\ nm$ and $2{,}800\ nm$. However, from the $|H|$ mode profiles in panels (c_3) and (c_4), it is observed that there are strong interactions between the magnetic fields and the bottom reflector at those wavelengths. In fact, the magnetic fields in these panels are not only confined in the region beneath each SRR, but they are also enhanced in the entire spacer region. This behavior indicates the role of propagating surface plasmon resonances in the absorptive responses of the MPA at larger wavelengths. In fact, a combination of low-Q resonances with the PSP ones at different wavelengths in the broadband region causes the broadband light absorption by the MPA.

In the next step, we examine how changes in t_{sio_2}, t_{Au} and t_{ITO} can affect light absorption of the metamaterial. Panels (a), (b), and (c) of Fig. 2.4 shows dependence of the absorbed light by MPA on the changes in t_{sio_2}, t_{Au} and t_{ITO}, respectively, while keeping all the other parameters the same as the aforementioned optimized/feasible values. One can observe in Fig. 2.4(a) that deviation from the optimized value (i.e. $t_{sio_2} = 160\ nm$) of the spacer layer leads to either losing the NIR broadband response (for $t_{sio_2} < 160\ nm$) or depriving the narrowband absorption in the visible region (for $t_{sio_2} > 160\ nm$). As mentioned hereinabove, the Au and ITO self-aligned SRRs are responsible for the narrowband and broadband absorptive response of the MPA. In agreement with that point, Fig. 2.4(b) shows that decreasing t_{Au} red-shifts the narrowband resonance (compared to the optimized case of $t_{Au} = 60\ nm$), broadens it and leads to a slight loss in the broadband response. On the other hand, choosing thicker values of the gold thickness has a negligible effect on the broadband response while it slightly blue shifts the narrowband resonance. Moreover, the decreasing thickness of ITO from the optimized value (i.e. $t_{ITO} = 80\ nm$) reduces the bandwidth while it has less effect on the narrowband resonance, see Figure 2.4(c). As a result, considering an absorption above 90% for the nearly perfect efficiency of our structure, the case of $160\ nm/60\ nm/80\ nm$ for $t_{sio_2}/t_{Au}/t_{ITO}$ gives the most promising optimum absorption with a bandwidth of $1{,}210\ nm$ (from $1{,}790\ nm$ to $3{,}000\ nm$) and a nearly perfect absorption at the wavelength of $767\ nm$.

The proposed design [shown in Fig. 2.1(c)] lacks polarization insensitivity that is the key characteristic for absorption features of the practical MPAs. Therefore, to resolve this deficiency, we improve the aforementioned design to a polarization independent one by enhancing the structural symmetry. A schematic of the symmetric unit cell composed of four self-aligned ITO-Au hybrid SRRs that are mutually rotated by 90° is depicted in Fig. 2.5(a). We keep all the geometrical parameters of each SRR in the symmetric unit cell as the optimized values of the nonsymmetrical design. The only modified parameter is the periodicity; i.e. $p_2 = 600\ nm$ in the calculations. Normal incidence absorption of the symmetric design is represented as the dashed-red curve in Fig. 2.5(b). Moreover, for the sake of comparison, the simulated absorption of the MPA of Fig. 2.1 is also shown as the solid blue curve. It is observed from the dashed-red curve in Fig. 2.5(b) that a broadband

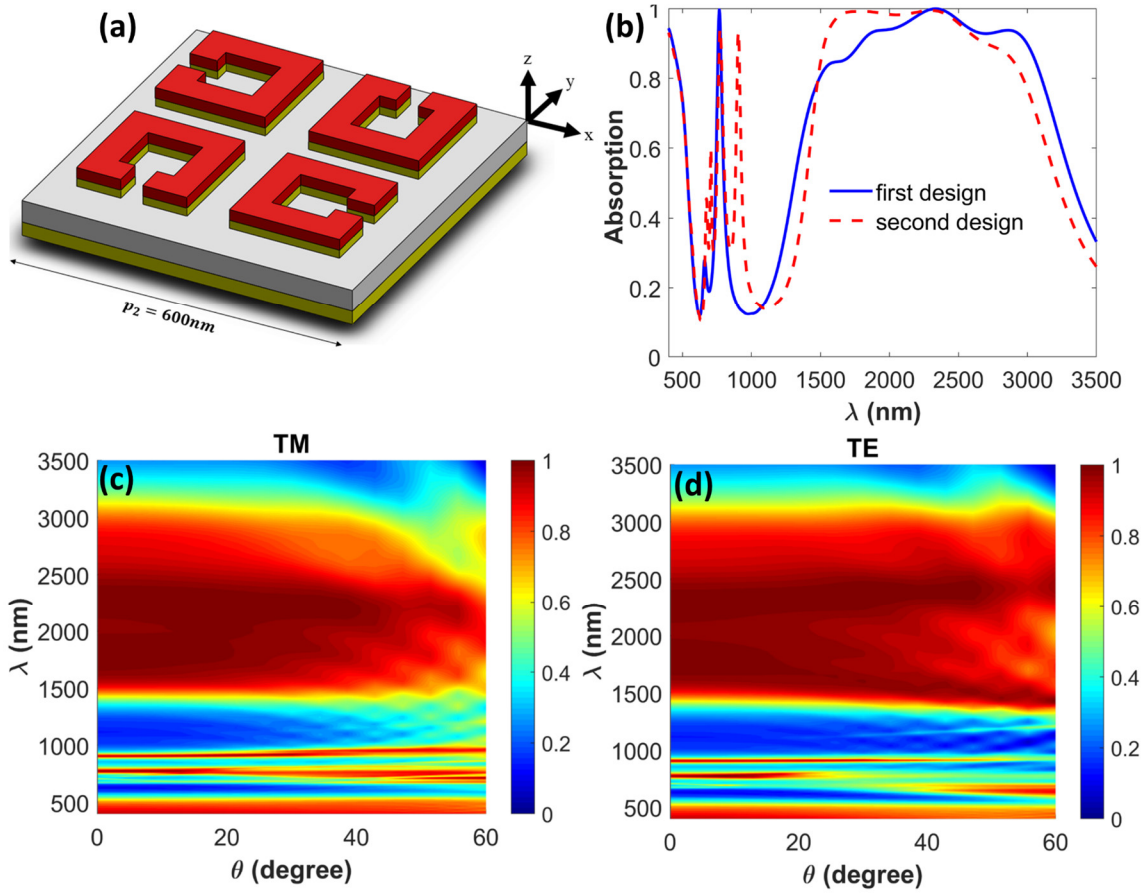

Figure 2.5. (a) Schematic of a unit cell of the symmetric MPA. This unit cell is composed of four self-aligned ITO-Au SRRs that are mutually rotated by 45°. Numerically calculated absorption of the symmetric metamaterial for normal incidence is shown by the dashed-red curve in panel (b). For the sake of comparison, the absorption of the nonsymmetric metamaterial of Fig. 1(c) is also illustrated again as the solid-blue curve. (c) and (d), respectively, represent the dependence of the absorption performance of the symmetric structure on the incident angle for TM and TE polarizations.

nearly perfect absorption (ranging from $1{,}530\ nm$ to $2{,}700\ nm$) and two narrowband nearly perfectabsorption peaks at $773\ nm$ ($FWHM{\sim}60\ nm$) and $900\ nm$ ($FWHM{\sim}49\ nm$) are obtained. Therefore, by employing the symmetric MPA, in addition to achieving a broadband absorption in the NIR

and a narrowband absorption in the visible, one additional narrow band absorption peak is also obtained. The additional narrow band response, in fact, improves the functionality of the symmetric structure upon the nonsymmetrical one. More importantly, it is observed in Figs. 2.5(c) and 2.5(d) that the nearly perfect and broadband absorption of the symmetric MPA is preserved up to 50 degrees of incident angle for both TM and TE

polarizations. The strength of the narrow band absorption resonances of the MPA are also kept unaffected for TM polarization while they are sensitive for angles of incidence more than 20 degree for TE polarization. Specifically, for TE polarization, there is only a single nearly perfect absorption peak at $\theta = 30^o$ around $900\ nm$ while at $\theta = 50^o$ only one nearly perfect resonance is observed around $773\ nm$.

The last point that should be addressed here is the physical mechanism behind the appearance of the additional resonance at $900\ nm$ in the MPA with the symmetric unit cell. This point is discussed in Fig. 2.6. In Fig. 2.6 the impact of changes in the periodicity ($600\ nm < p_2 < 1200\ nm$) on the overall normal incidence absorption characteristics of the MPA is investigated. Here, all other geometrical parameters are kept as the aforementioned optimized values. For the sake of feasibility, the minimum value of the periodicity is chosen as $600\ nm$. As already explained, once the periodicity is chosen as this value, a broadband response in the NIR region together with two narrowband absorption peaks – in the visible and NIR regions – are obtained. As Fig. 2.6(b) clearly shows, by increasing the periodicity, the structure loses its broadband absorptive feature. As an example, once the periodicity is taken as $1{,}200\ nm$, the broadband feature is totally lost. On the other hand, the dependence of the narrowband response of the metamaterial to the increase in p_2 is somehow different than the broadband response. By increasing p_2 from $600\ nm$ to $800\ nm$, the narrowband resonances are red-shifted and the three narrow band resonances appear, see Fig. 2.6(b). In fact, the physical mechanism behind the appearance of additional narrowband resonances is the mutual coupling effect between the SRRs in each symmetric unit cell and the adjacent unit cells. However, at $p_2 = 800\ nm$ the broadband characteristic is considerably lost. This point is also evident once the red- dashed curve is compared to the solid-black one in Fig. 2.6(b). Therefore, as far as we are interested in keeping both broadband and narrowband responses as efficient as possible, $p_2 = 600\ nm$ is the optimized choice. It is noteworthy that according to the Kirchhoff's law of thermal radiation, the spectral emissivity (E) of a structure is equal to its spectral absorptivity; i.e. $A(\lambda) = E(\lambda)$. Consequently, the absorption features of our proposed device can be employed for the realization of thermal emission characteristics [117].

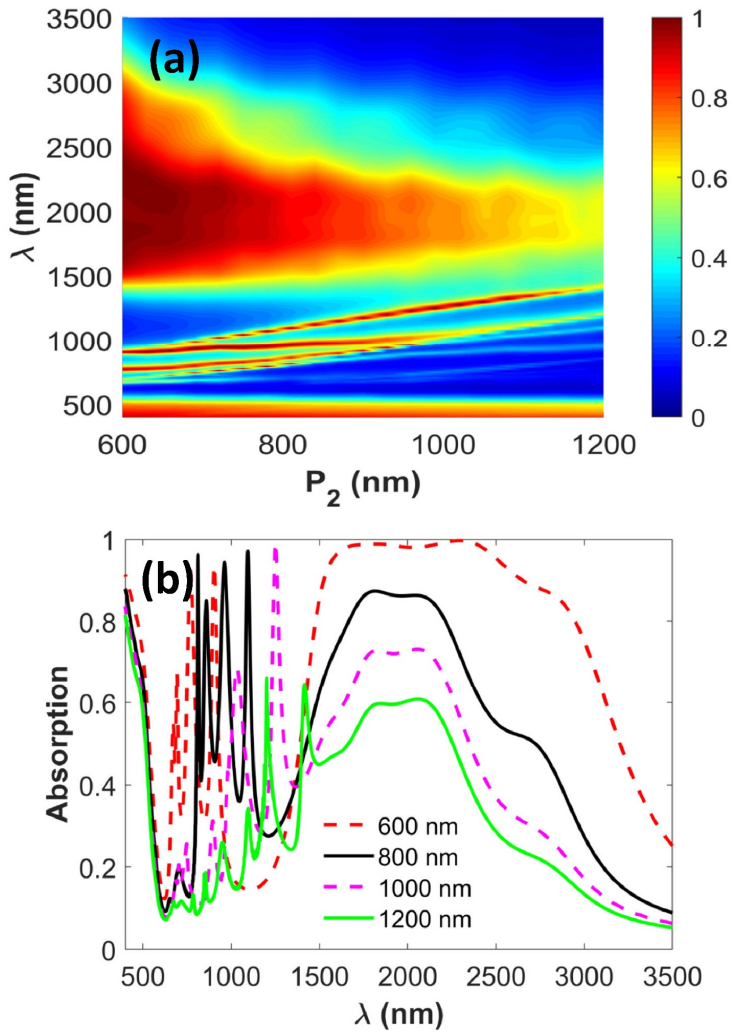

Figure 2.6. (a) Spectral absorption of the symmetric MPA as the function periodicity of the metamaterial, p_2. In agreement with panel (a), the absorption spectra for four different values of p_2 are shown in panel (b). Note that the geometrical parameters are chosen as the optimized ones mentioned in the text. The results are provided for normal incidence.

CHAPTER 3

Active tuning from narrowband to broadband absorbers using a sub-wavelength VO_2 embedded layer

This chapter is one part reprinted with permission from: **Ataollah Kalantari Osgouei**, Hodjat Hajian, Bahram Khalichi, Andriy E. Serebryannikov, Amir Ghobadi, and Ekmel Ozbay, Plasmonic, 2021, pp. 1-9.

3.1. Introduction

Metamaterials are a periodic array of subwavelength structures, which can be artificially engineered to achieve exotic properties not available in nature [64], [65]. These characteristics make metamaterials a promising technology for a wide variety of applications, such as light harvesting [118], [119], invisible cloaks [120], asymmetric light transmission [67], [121], lasing [68], and negative refractive index [69], [122]. Among them, manipulating and controlling the absorption properties of optical metamaterials have gained a lot of attention over the last decades. In particular, metamaterials with nearly perfect absorption features are called metamaterial perfect absorbers (MPAs). MPAs have been demonstrated to realize either narrow or broadband absorptions depending on the

geometry and the material type being used in the design. The former resonant response may have applications in sensing [123], imaging [73], and color filtering [124], while the latter correspondent is promising in the areas of solar cells [125], photochemical devices [126], hot-electron-based photodetectors [127], and radiative cooling [128]. Such MPAs have been developed from visible [79], [129] to terahertz [130], [131] and the microwave regions [132], [133]. MPAs can be physically realized by suppressing both the transmission and reflection of the incident electromagnetic (EM) waves, simultaneously. The transmission can be eliminated by using an optically thick metallic layer as a mirror, and the reflection may be blocked by matching the impedance of the structure with the surrounding medium. Therefore, metal-insulator pair based configurations such as metal-insulator-metal (MIM) cavity designs have been proposed and widely used in the literature [97], [134]. Generally, in these structures, a dielectric film is sandwiched by a patterned top metal film and a flat bottom reflector mirror layer. However, the resonant properties of MPAs are almost fixed, which greatly reduce their practical applications. Therefore, to fully exploit the optical properties and to extend the functionality of MPAs, dynamically tunable control over resonances such as electrical [135], optical [136], and thermal [137] tuning have been studied to realize actively tunable metamaterials. Recently, the thermal tunable narrowband MPAs are emerging with possible applications such as optical modulator [138], optical switches [139], and infrared (IR) camouflage [140]. Certain mediums known as phase-change materials (PCM) like GeSbTe (germanium-antimony-tellurium or GST) and vanadium dioxide (VO_2) are the most prominent substances for active MPA designs. Their optical properties show a large change when undergoing a phase transition. The temperature requires for GST crystallization is around $160°C$. Moreover, the amorphization of GST is only obtained at the temperature above $640°C$, which is required by very fast cooling. In contrast, VO_2 is a volatile PCM, and the insulator-to-metal transition occurs at a much lower temperature of $68°C$. During this transition, the lattice of the structure is transformed from a monoclinic to tetragonal one as the temperature increases well above the critical point. At the same time, the conductivity of VO_2 rises by several orders, leading to sudden change in the optical and electrical properties of the material [141]–[143]. It is also important to discuss here that the insulator-to-metal transition of VO_2 can be perfectly reversible when the temperature

of the material drops below the critical transition temperature, which provides a great power in memory storage. However, the bandwidth of MPAs based on GST and VO_2 are very small, usually around hundreds of nanometers [144], [145] at the near-infrared ranges (NIR) because of the inherent absorption and ohmic loss of metallic resonators. On the other hand, Mie theory predicts that it is possible to design narrowband MPAs based on employing high-refractive index dielectric materials like silicon (Si) and germanium (Ge), since they strongly support magnetic and electric dipoles at the resonance wavelengths [146], [147]. Nevertheless, the thermo-optic coefficient of these materials is rather low and cannot provide a dynamic tuning. In a recent work, Zhaol et al. proposed a linearly thermal-tunable narrowband MPA using four-nanorod amorphous Si (a-Si) with the sensitivity of $0.08\ nm\ C^{-1}$. They reported that the resonances can be tuned from 1164 to 1172 nm by increasing the temperature of a-Si from $20°C$ to $120°C$ [148]. Taking everything into account, in an ideal scheme, a hybrid design that can couple dielectric based Mie resonators with PCMs can provide a strong thermal tunability and diverse functionalities. As a result, an elegant design based on PCM VO_2 embedded in a-Si nanograting resonator is proposed in the present paper. The bottom layer of the structure is chosen to be silver (Ag) with a sufficient thickness to block transmission leading to high absorptivity and narrow-band perfect absorption at the NIR region. Specifically, double narrowband perfect absorptions are successfully achieved at the resonant wavelengths of 1077 nm and 1314 nm under the insulator VO_2 state. Under the metallic VO_2 phase, the proposed design demonstrates triple spectrally adjacent perfect absorptions at the wavelength peaks of 1064 nm, 1166 nm, and 1323 nm, which leads to a broadband light absorption. The obtained electric field distributions near the resonance wavelengths, calculated via the eigenvalue solution of Maxwell's equation in the region of interest, besides the numerical simulation of the proposed structure based on the commercial finite-differences time-domain solver, indicate that the first and second resonant peaks are Fabry-Perot (FP) like resonances. While the third peak is due to the excitation of localized surface plasmon resonances (LSPRs) in metal-dielectric interface. From the obtained results, it is also seen that, upon insulator-metal transformation, the first resonance experiences a blue shift due to change in the phase of reflected wave. The second resonance is due to formation of a virtual MIM design, due to the lossy nature of VO_2 in

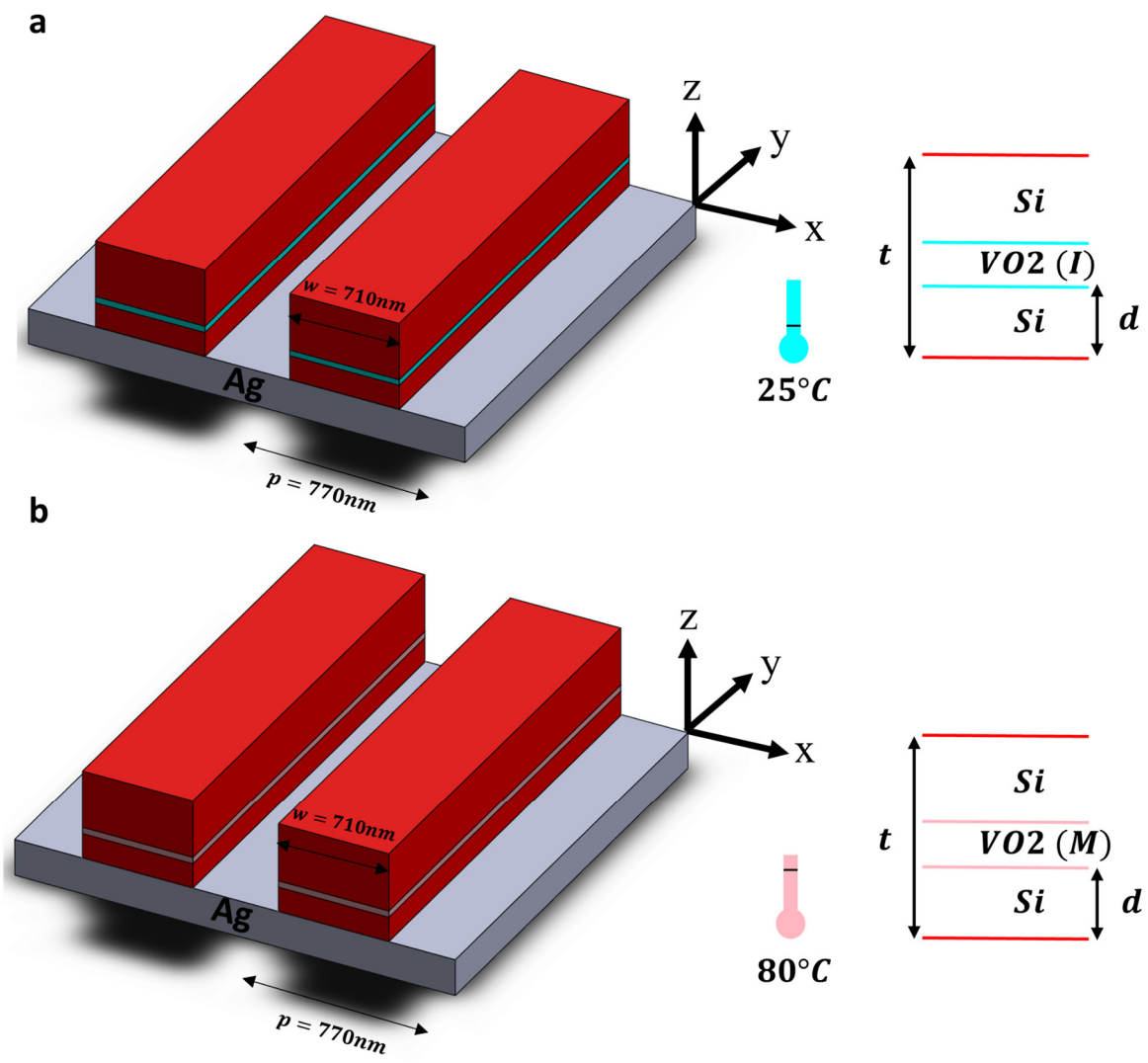

Figure 3.2. Geometry and schematic of the VO_2-based metamaterial absorber. The absorber consists of VO_2 in (a) the insulating phase and (b) the metallic phase sandwitched between layers of a-Si and continuous film of Ag as the bottom layer of the structure.

metal phase. Finally, the third LSPR mode experiences a slight red-shift due to increase in the effective refractive index of the grating design. In the last section, the thermal tunability of a-Si itself is studied. It is shown that, due to strong field confinement in the grating gaps, a new dynamic tuning is added to the structure due to change in the thermo-optic coefficient of a-Si. This paper numerically demonstrates the possibility of the realization of multiple functionalities using a hybrid plasmonic-PCM design.

3.2. Structure and Simulation Setup

The schematic diagram of thermal tunable narrowband metamaterial absorber is shown in Fig. 3.1. The structure is composed of a VO_2 layer sandwiched between a-Si and a continuous Ag bottom reflector. Due to the resonating nature of the structure [149]–[151], CST Microwave Studio eigen-solver is utilized to have an initial guess regarding the dimension of the parameters of the structure and the resonance wavelengths in the NIR region which are useful for the future optimization. Accordingly, the bottom layer is chosen to be 100 nm, with no transmission in our desired range. The thickness of the VO_2 layer is $5\ nm$. The distance from the top surface of Ag to VO_2 layer is d, as shown in Fig. 3.1. The thickness of the nanograting structure Si/VO_2/Si is t while its width is w. The period of the unit cell is fixed at P in the x direction. The numerical calculations based on commercial finite-differences time-domain (FDTD) software package Lumerical FDTD solutions [108] is used to obtain the optical properties of the proposed absorber. The periodic boundary condition is applied only in the x-direction and the perfectly matched layer (PML) boundary condition is used in the z-direction in order to avoid the boundary scattering. The reflection spectrum is recorded by putting a 2-D frequency-domain power monitor, which is placed behind the incident source monitor. Since the bottom metallic layer is chosen to be thick enough to suppress the transmission, the transmission is nearly zero and absorption can be calculated from the formula $A = 1 - R$. The frequency profile monitors are used to obtain electric and magnetic fields at the resonances. The optical properties of the silver film follow the common Palik model and the optical constant of VO_2 in both the insulator and metallic phases are reported in [152], where the permittivity of the material in the NIR region is experimentally measured by variable angle spectroscopic ellipsometry and then fitted by the Tauc-Lorentz model [VO_2 (Insulator)] and Drude model [VO_2 (Metal)]. The VO_2 in the insulator phase acts like a spacer at a room temperature of $25°C$ as presented in Fig. 3.1(a), while the transition to the metallic phase can be accomplished in a hot environment at $80°C$ as illustrated in Fig. 1b. From now on, we specifically refer to these different phases as VO_2 (I) and VO_2 (M). As for the a-Si, we use a linear relationship with the temperature dependance limited by the thermal-optical coefficient given by $3.25 \times 10^{-4}/°\ C(n(T)) = 3.42 + 3.25 \times 10^{-4} \times (T - 20)$.

According to the relationship, the refractive index of a-Si at the room temperature of $25°C$ is 3.42 [148], [153]. To get proper physical insight into the absorption resonances of the proposed design, we replaced a collection of scattering object materials by a homogeneous medium, whose properties result from the averaging of local EM fields. The procedure of modeling a composite environment and replacing it with a homogeneous medium is defined as the effective medium theory. It is better to be noted that the equivalent problem can be defined when the applied electric fields are static or have spatial variations on a large scale. Therefore, it is possible to replace the inhomogeneous materials by an effective medium[107], [154] where the electromagnetic properties of the inhomogeneous materials can be obtained from solving the Maxwell's equations inside the effective medium. Accordingly, we exploit the effective medium theory to describe the impedance amplitude of the absorption resonances for both insulator and metallic phases. Meanwhile, the effective and impedance parameters of the proposed metamaterial absorber are extracted using the S-parameter calculation embedded in FDTD Lumerical solver.

3.3. Results and Discussions

In this section, we are going to study the impact of periodicity, thickness, and width of a-Si in the overall absorption spectra of the proposed design. It is crucial to be mentioned here that the real part of the permittivity of a-Si and VO_2 (I) is almost equal to each other at the room temperature of $25°C$. Therefore, we can simplify the design to a straightforward simulation route of Ag-Si to study the overall absorption response of the proposed structure. As a first step, the absorption spectra of the structure as a function of periodicity differing from 750 nm to 1000 nm at different operating wavelengths is considered in Fig. 3.2(a), while the other material dimensions of the structure are kept unchanged. The result represents a double resonance response for all P values, where both resonances experience a red shift as the periodicity increases. Moreover, larger P values broadens the absorption peak (see Fig. 3.2(a) for the bandwidth of the resonances) and reduces the strength of the longer wavelength resonance. In other words, the absorption spectra experience a sharp reduction for the second resonance once the periodicity of the

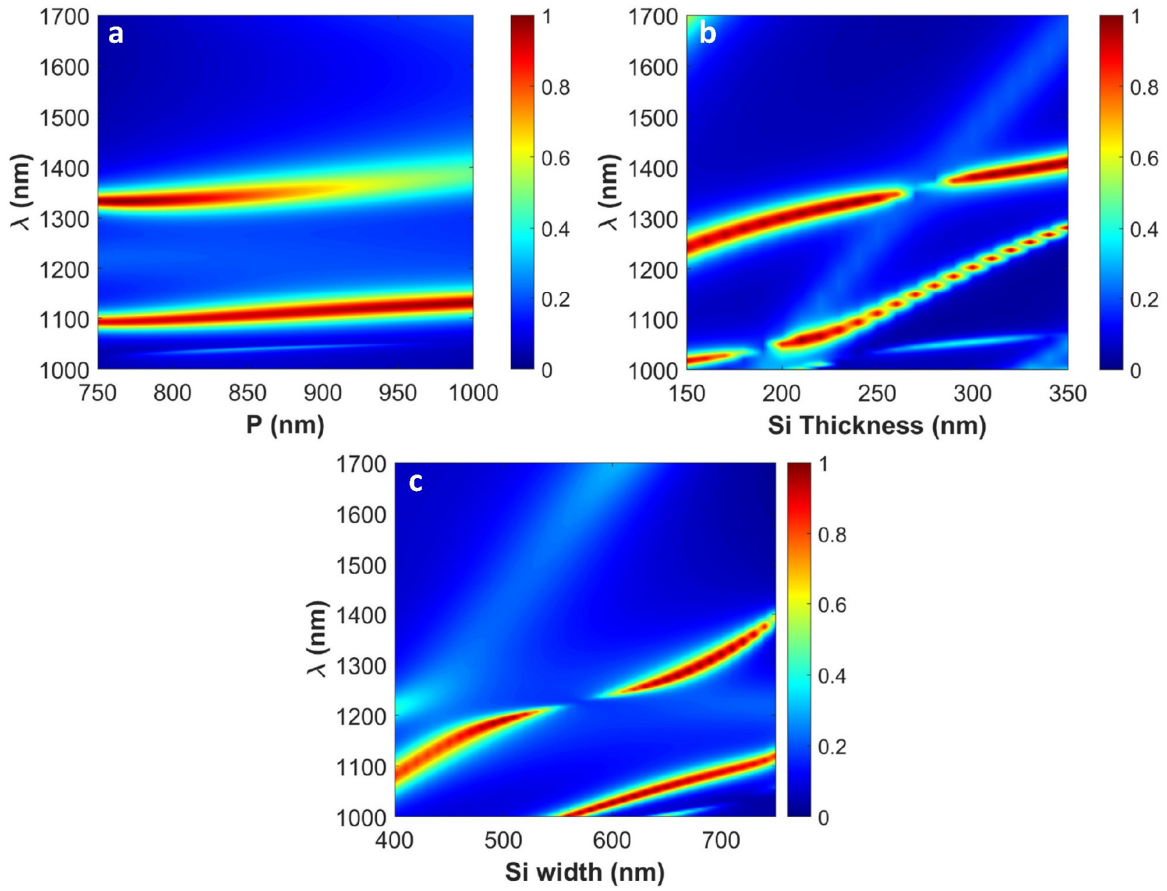

Figure 3.2. Color plots of the absorption spectra at different operating wavelengths versus (a) periodicity of the grating, (b) the thickness of the a-Si layer, (c) and the width of the a-Si layer.

design is increased from 750 nm to 1000 nm. Keeping in mind that the perfect absorption threshold is considered as 0.9, the optimal periodicity is chosen as 770 nm. The next step is sweeping a-Si layer shorter resonance wavelengths. Accordingly, the origin of the first and second resonances depend on the thickness and width of the grating, respectively. All in all, the optimal obtained values are considered for the design of the proposed narrowband NIR MPA. As thickness from 150 nm to 350 nm as the result is presented in Fig. 3.2(b). It can be observed that both resonances red-shift, and the second resonance has more-pronounced change with a semi-linear trend. Again, taking the strength and bandwidth of the resonances into consideration, the optimized thickness value that retains both the narrowband peaks in the structure is 240 nm. At the final step, a-Si width is swept from 400 nm to 750 nm where both the periodicity and the thickness of a-Si are

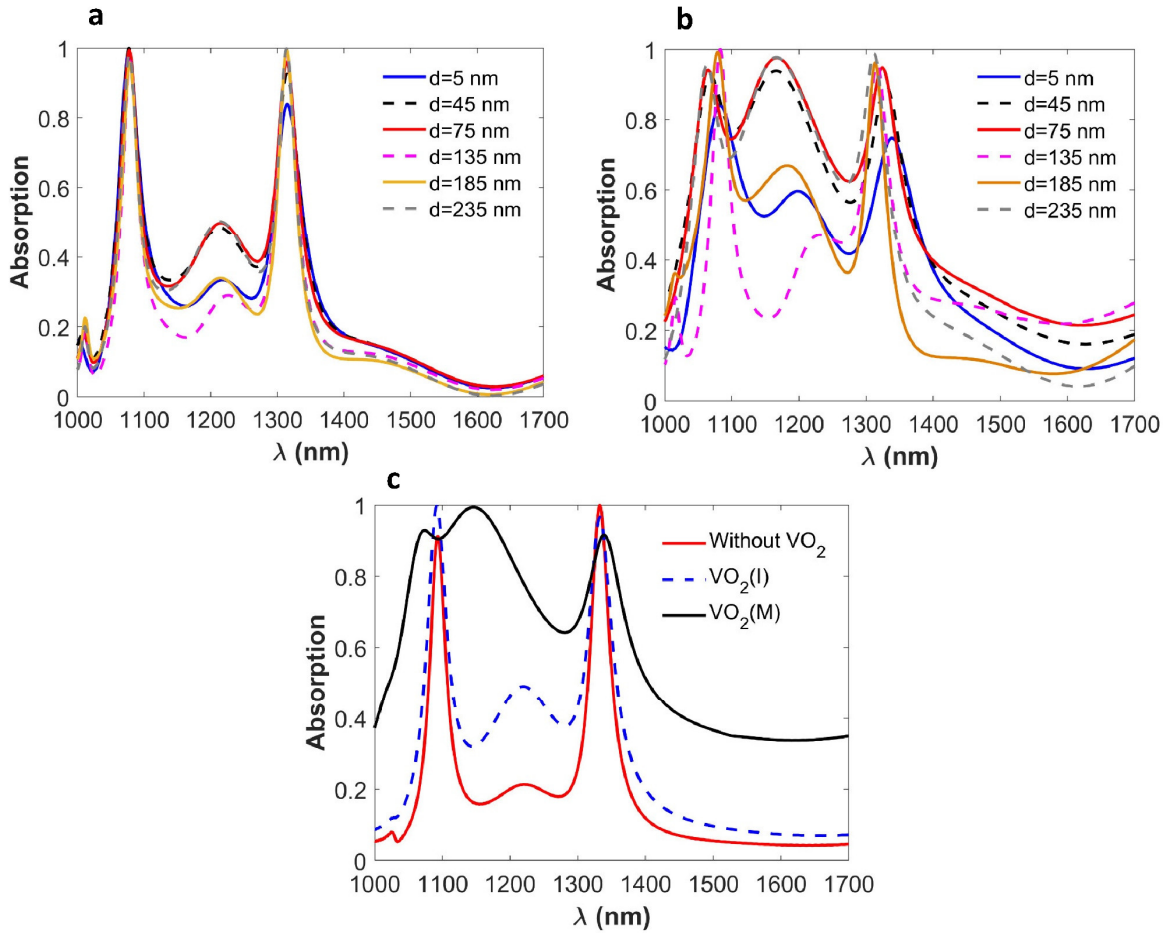

Figure 3.3. The calculated absorption spectra of the proposed absorber based on distances of VO_2 film mid plane from the bottom metallic layer (a) in the insulator phase (b) in the metallic phase (c) and the obtained optimized distances of VO2 layer in the insulator and metallic phases compared with absorption spectra without VO_2 layer.

kept at their optimal values. The corresponding result is presented in Fig. 3.2(c), and it demonstrates that the absorption response versus the width of an a-Si layer can take a wider bandwidth due to the excitation of both resonances, while the first resonant peak completely disappears by moving toward a narrower Si width. Moreover, in comparison to the width changes [as illustrated in Fig. 3.2(b)], the thickness variations cause weaker shifts in the presented in Fig. 3.3(a)-(b), the effects of changing the locations of VO_2 layer (at two different phases) on the overall absorption spectra of the proposed structure are studied. In the figure, d denotes the distance of VO_2 film from the bottom metallic layer. Fig. 3.3(a) demonstrates that the overall spectral response for VO_2 (I) is somehow

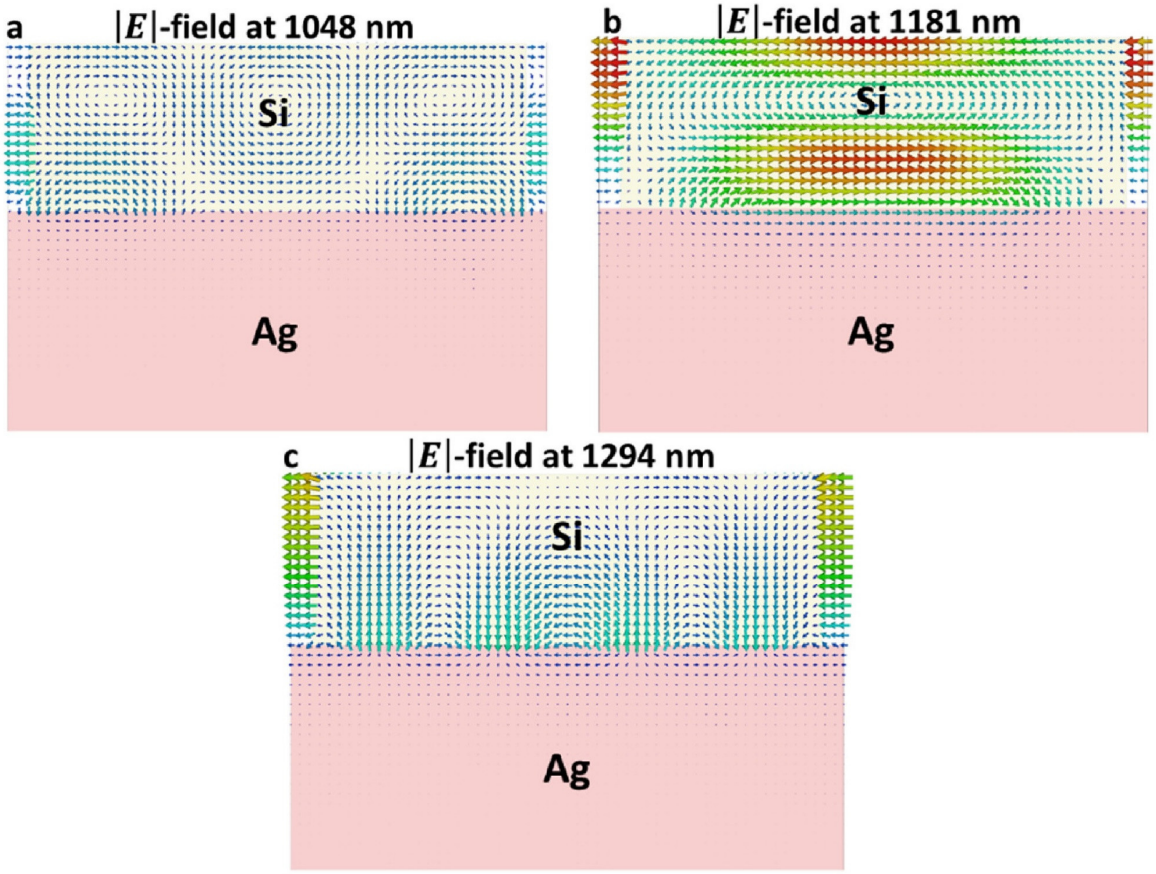

Figure 3.4. Vector electric-field distributions of the proposed MPA with VO_2 layer under the insulating state at the resonant wavelengths of (a) 1048 nm, (b)1181 nm, (c) and 1294 nm.

insensitive to the variation of d, in spite of slight changes in the strength of the resonances, which agrees with our expectation based on similar permittivity values for both a-Si and VO_2 (I). On the contrary, variation of d has a significant impact on the absorption response of the structure as well as strength of the resonances when VO_2 layer at the metallic phase is used. In this case, at two different values of d (75 nm and 235 nm), a second weak resonance gets stronger with a peak amplitude above 0.9. Therefore, in the metallic phase, the position of VO_2 layer can be manipulated to efficiently excite another resonance with a slight effect in the first and third resonance values. As d increases, the first resonance experiences a blue-shift, while the third resonance shows a red-shift which will be discussed later. Taking all into account, the optimal position of VO_2 layer is considered to be 75 nm to have a broad and nearly flat absorption response in the metallic phase. To have a better qualitative comparison, the absorption response of the MPA absorber with

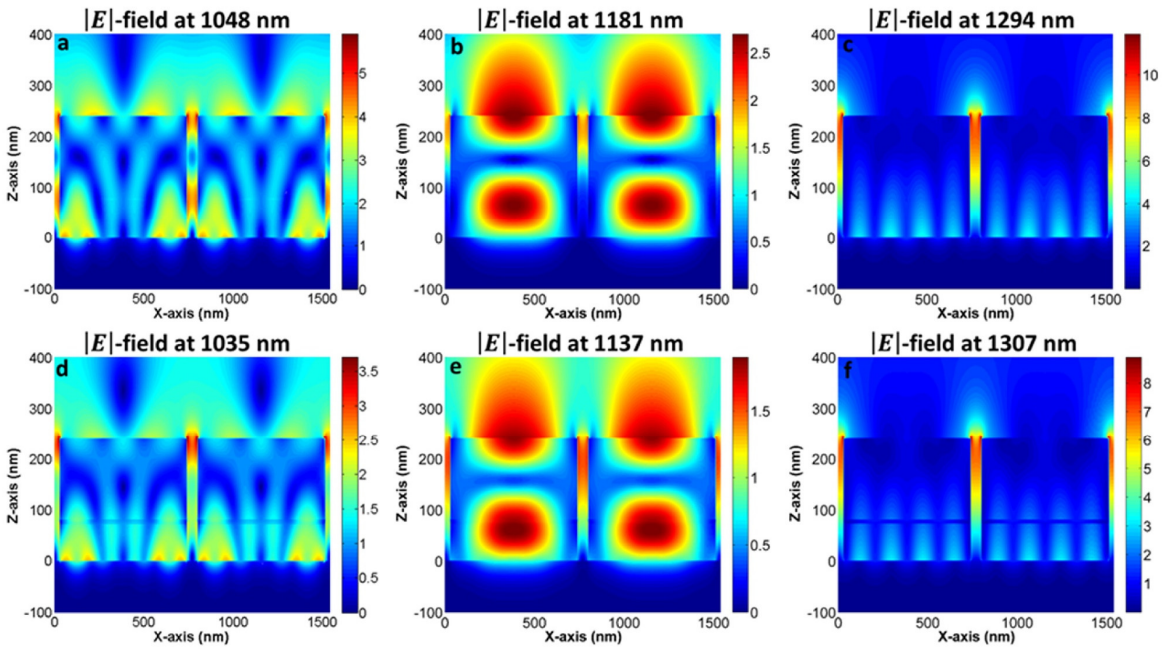

Figure 3.5. Magnitude of electric field distributions including VO_2 layer in the (a)-(c) insulator phase at the resonant wavelengths of 1048 nm, 1181 nm and 1294 nm and (d)-(f) in the metallic phase at the resonant wavelengths of 1035 nm, 1137 nm, 1307 nm.

(both metallic and insulator phases) and without a VO_2 embedded layer is plotted in Fig. 3.3(c). The figure implies thatupon a thermally induced phase change, a distinct transformation from a narrowband absorber to a broadband one is achieved using an ultrathin VO_2 interlayer. To gain an insight on the origin of these resonance modes, CST Microwave Studio eigen-solver together with FDTD commercial software are utilized to determine the supported modes by the MPA with and without considering the VO_2 layer. Therefore, we can interpret the coupling among these modes and VO_2 interlayer. The vector electric-field distributions across the $x-z$ plane, at three wavelength values of 1048 nm, 1181 nm, and 1294 nm, are depicted in Fig. 3.4(a)-(c). Formation of standing wave interference patterns within the Si grating shows that the first and second resonance modes are dominantly FP like modes. However, the third mode originates from the excitation of LSPRs in Ag-Si interface. This is in agreement with the obtained results in Fig. 3.2. The strong dependence of the first peak position to the grating thickness [Fig. 3.2(b)] is due to the change in the optical path length of the FP resonator. While the third resonance is tailored by the grating width [Fig. 3.2(c)] which is a major factor defining

the resonance position of the LSPR mode. To analyze the coupling of these modes to metal and insulator phase VO_2 layer, electric-field distributions in the $x-z$ plane are recorded and illustrated in Fig. 3.5. As is apparently displayed in this figure, the field distributions are quite similar for both metallic and insulator phase designs. The first resonance is a hybrid mode with FP resonance dominancy that is formed due to the interference of incoming and reflected waves with the cavity. When PCM material changes its phase to lossy metallic one, due to its larger permittivity values, its optical path length increases and, therefore, the impedance matching condition is blue-shifted. The second resonance is also a FP mode with hot spots formed within the a-Si grating. Placing VO_2 in a high-field region will make its absorption maximized. This is the case when *d* equals to 75 nm and 235 nm, see Fig. 3. In fact, in this situation, Ag-Si-VO_2 forms a virtual MIM cavity design. When VO_2 transforms from a low loss to lossy phase, the cavity is activated and a new resonance starts to appear. The last mode, which is the LSPR mode, shows the field localization patterns in the Ag-Si interface. In this case, the change in permittivity of the PCM will change the effective refractive index of the grating and therefore, this leads to a red-shift in the resonance wavelength of the LSPR. All these results show that, upon use of right geometries and design, an ultrathin PCM can diversely modulate the optical absorption response of an MPA. In addition to mode profile analysis, the absorption properties of the proposed design can be fully explained by the equivalent media and impedance matching theories. Since the element size of the metamaterial absorber is much smaller than the operation wavelength, and the effect of the internal microscope atoms and molecules of the EM field can be easily ignored. Therefore, the whole metamaterial structure can be regarded as a uniform and equivalent medium. At the same time, the input impedance of the entire structure, which is normalized to the free space impedance, can be analytically calculated by the following formula:

$$Z_{in} = \frac{\sqrt{(1+S_{11}(w))^2 - S_{21}(w)^2}}{\sqrt{(1-S_{11}(w))^2 - S_{21}(w)^2}} \quad (1)$$

where $S_{11}(\mathrm{w})$ and $S_{21}(w)$ are the reflection and transmission coefficients obtained by the *S*-parameter method. When the impedance matching condition is satisfied, the EM wave incident on the surface of the metamaterial can enter the structure without reflection and be directly converted into heating energy and absorbed in the structure. Therefore, the

value of the equivalent complex impedance must be equal to 1. The equivalent impedance of the metamaterial absorber is also affected by the permittivity and permeability of the material. Here, we use the impedance theory technique to describe the perfect absorber of the structure as shown in Fig. 3.6. The results of the impedance amplitude for the VO_2 (I) is shown in Fig. 3.6(a). In order to have perfect matching with free space, the real part of the normalized input impedance of the design must be close to 1, and its imaginary part should be near zero. Therefore, the impedance amplitude of the absorber at the desired perfect absorption peaks should be 1. For instance, the impedance amplitude for the spectra position of the first peak at 1077 nm is the order of magnitude 1, causing the strong narrowband perfect absorption. The same statement can also be applied to the second resonant peak as well as for the case of VO_2 (M) structure, which is shown in Fig. 3.6(b), once more, the results of the impedance amplitude is completely in agreement with the theoretical conceptions. A good agreement between the impedance theory and actual MPAs structures prove that the impedance theory is a common approach to investigate the physical mechanism of the EM waves of the structure. Up to this point, we showed how an ultrathin PCM can strongly change the optical absorption response of a MPA design in cold and hot states. In general, the active tuning optical absorption of MPA is achieved by modulating the refractive index of the material. However, in PCM materials, this change is rather abrupt and linear tuning is not possible with these designs. However, in reality, all types of materials have thermo-optic coefficients but these values are quite small. For instance, the refractive index of a-Si has a linear relationship with the temperature change (ΔT) with a thermo-optic coefficient of $3.25 \times 10^{-4}\ C^{-1}$. Therefore, for a bulk a-Si, the change is temperature cause a negligible change in the material index and, therefore, it cannot be used for active tuning scenarios. However, if we can design a structure with strong field localization in sub-wavelength geometry units, we can intensify response to any changes in the refractive index of the grating. In the previous section, we showed that the third resonance is red-shifted upon transformation from clod to hot state. This was due to change in the effective refractive index of the grating. Now, a new mechanism can be added to the structure, which is the thermal tunability of a-Si index. By this way, we can design a linear- thermal tunable modulator. Fig. 3.7 shows the absorptionthis behavior. As in our case, we have strong field confinement in the gap

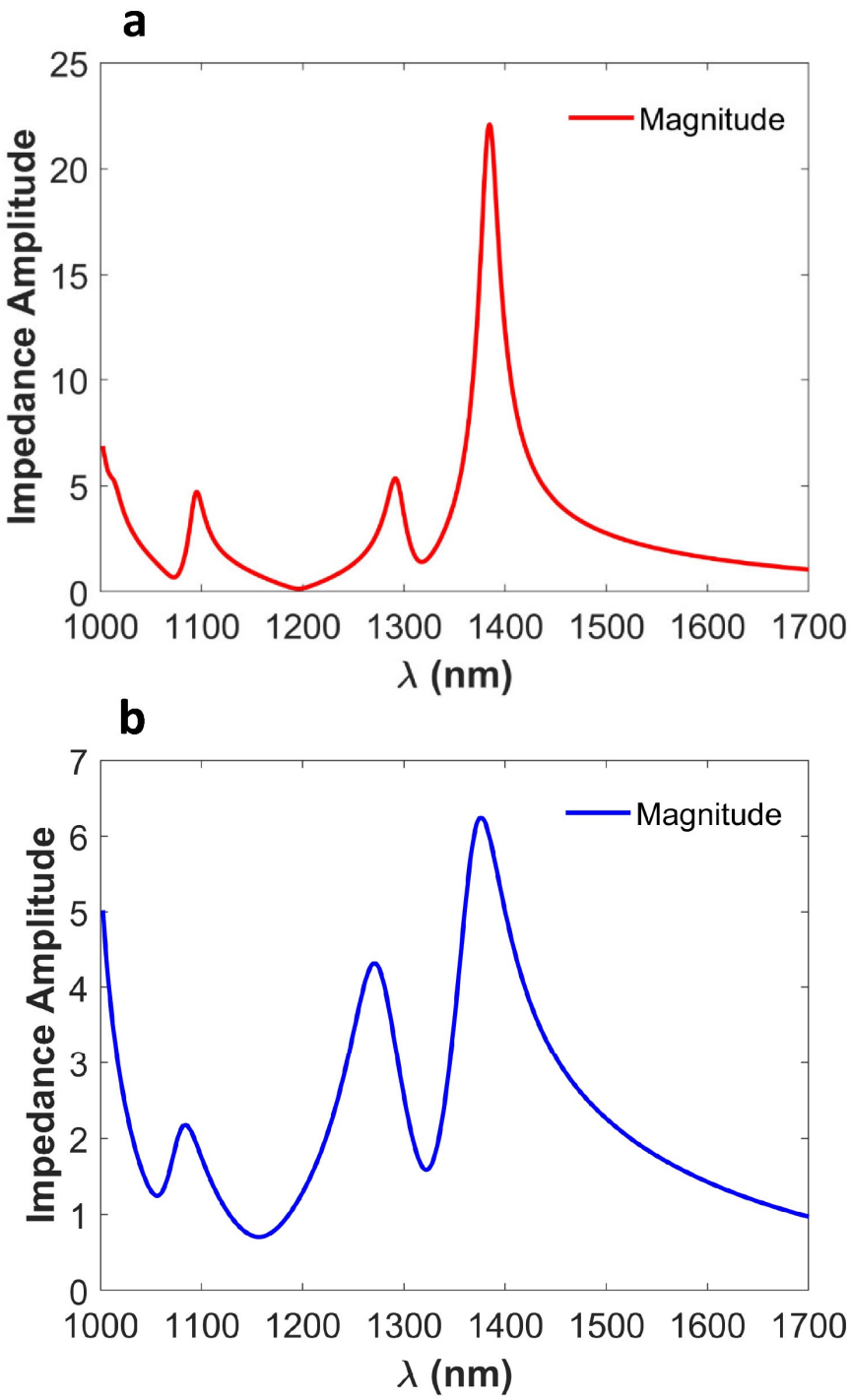

Figure 3.6. Calculated the impedance amplitude of the absorber based on VO_2 under the (a) insulating phase and, (b) metallic phase.

regions, as shown in Fig. 3.5. Therefore, in such hot spots, the MPA design can show a strong response of the MPA design at different temperatures. In the studied range, the refractive index of the a-Si increases linearly from 3.54 to 3.59 when the temperature of

the absorber increases from $25°C$ to $250°C$. At the lower range, when the temperatureincreases from $25°C$ to $100°C$, the PCM materials takes the main role in the absorption peak tuning. After this temperature, the change in a-Si index becomes the dominant mechanism for thermal tunability function of the MPA. As extracted from Fig. 7b, the overall sensitivity of the design reaches to a value as high as $S = \frac{\Delta\lambda}{\Delta T} \simeq 0.09 nm^{\circ}C^{-1}$. Beyond the simple wavelengths tuning of the structure at NIR, the development of thermo-optic filters opens a new type of dynamic functionality, such as switching between the reflection and transmission at the specific wavelength channel. Such a linear thermal-tunable metamaterial absorber is a promising device in the applications of optical modulator and infrared (IR) camouflage.

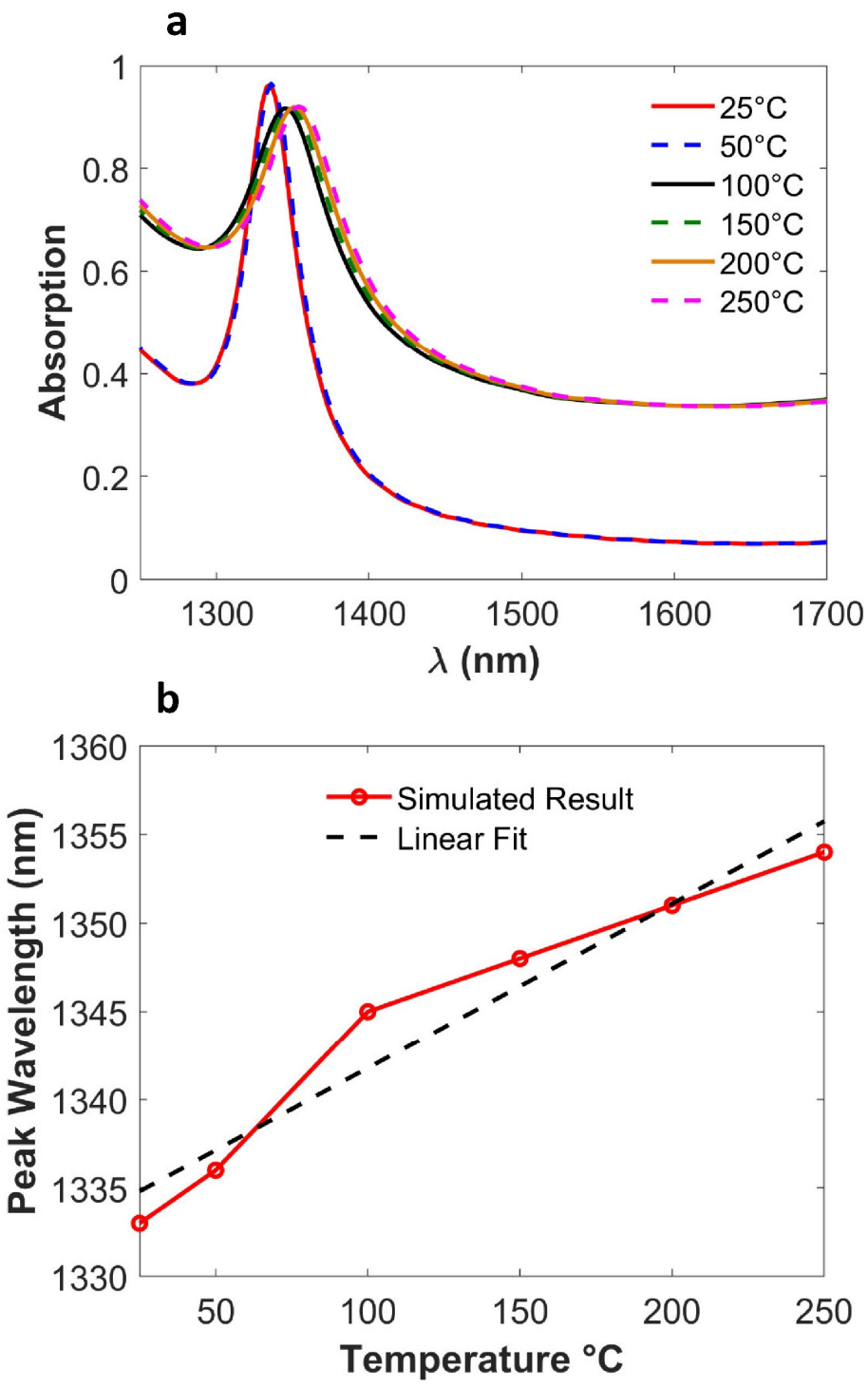

Figure 3.7. Spectra absorptivity, peak absorptivity of the third resonant peak as functions of the temperature (a) varying from 25°C to 250°C. (b) The variation of resonance wavelengths corresponding to the estimated thermal-optical sensitivity through the linear fitting of the data of the proposed structure with respect to the temperature.

CHAPTER 4

A spectrally selective gap surface-plasmon-based nanoantenna emitter compatible with multiple thermal infrared applications

This chapter is one part reprinted with permission from: **Ataollah Kalantari Osgouei**, Amir Ghobadi, Bahram Khalichi, Amir Ghobadi, and Ekmel Ozbay, Journal of optics, 2021.

4.1. Introduction

Total emissive power per unit area from a hot surface is defined by the Stefan-Boltzmann law $P = \varepsilon\sigma T^4$ [155], [156], where σ is the Stefan-Boltzmann constant, ε and T are the emissivity and absolute temperature of the object, respectively. At the thermal equilibrium, Kirchhoff's radiation law [155], [156] states that the wavelength-dependent thermal radiation of a surface is equal to the optical absorption of that surface defined as $\varepsilon(T,\lambda) = \alpha(T,\lambda)$. Therefore, suppressing the thermal radiation can be achieved by reducing the emissivity/absorptivity (ε) or the real temperature of the object (T).

However, the poor efficiency of the thermal radiation contributes to a sharp increase in the real temperature of the object. Accordingly, wavelength-selective thermal emitters are widely used to overcome this problem. In particular, a wavelength-selective material-based shield should have a low emissivity to reduce the object's thermal radiation within specific atmospheric windows as well as have a high emission outside of those atmospheric windows for the radiative cooling applications. In other words, the thermal radiation should dominantly be suppressed within the mid-wave infrared (MWIR: $3-5\,\mu$m) and the long-wave infrared (LWIR: $8-12\,\mu$m) ranges representing the transmission channels for electromagnetic waves in the atmosphere, while the thermal radiation is allowed to pass in the non-transmissive (absorption) windows, including $1.5-1.61\,\mu$m, $2.15-3\,\mu$m, $4-4.2\,\mu$m, and $5-8\,\mu$m, due to the fact that the absorption phenomenon quench the propagation of emitted photons in these ranges [157]. This wavelength-selective characteristic makes the object blend into the background and offers thermal radiation management for multiple thermal camouflage scenarios. Moreover, to have a comprehensive infrared characteristic, the design should absorb (solar) photons in the range of $0.9-1.7\,\mu$m to hide from short-wave infrared (SWIR) and laser tracking cameras (typically operating at 1064 nm). Since the design of wavelength-selective thermal nanoantenna emitter is equivalent to the design of wavelength-selective thermal nanoantenna absorber (Kirchhoff's law), metamaterial-based perfect absorbers with wavelength selectivity characteristic have attracted considerable attention due to their potential applications in radiative cooling [128], [158] and thermophotovoltaics [159], [160]. In addition, plasmonic metamaterials [82], [161], [162] and photonic crystals [163], [164] are widely exploited in thermal radiation management [165]–[173] as an ability to hide or disguise an object from infrared (IR) detection equipment and thermal imaging systems. Although photonic crystals can be designed to realize high emissivity with a special structure[163], [164], the configuration complexity makes photonic crystals less suitable in high-temperature environments due to the thermal stress [168]. On the other hand, plasmonic metamaterials as a periodic array of subwavelength structures can be artificially engineered to achieve exotic properties in terms of perfect absorptions and wavelength selectivity. The absorption can reach near unity at specific wavelengths, enabling the realization of perfect absorptions. Generally, metal-insulator-metal (MIM)

plasmonic-based cavity designs are considered as one of the typical configurations for designing near unity wavelength-selective absorbers [79], [174]–[181]. Properly choosing selective emissive materials for an MIM cavity design and its extensions to composite unit cell [140], [182] or multi-layer [183], [184] structures can lead to wavelength-selective metamaterial-based nanoantenna emitters/absorbers satisfying the requirements of multiple thermal infrared applications. Overall, in an ideal architecture, a wavelength-selective thermal nanoantenna emitter should radiatively cool the surface within specific atmospheric absorption windows without being detected by infrared cameras. In the first part of this paper, a wavelength-selective nanoantenna emitter based on the excitation of gap surface plasmon modes using an MIM configuration (silicon dioxide (SiO_2) sandwiched between silver (Ag) layers) is proposed. The proposed structure, called design I, shows triple narrowband perfect absorptions at the resonance wavelengths of 1524 nm, 2279 nm, and 6000 nm that perfectly match the atmospheric absorption bands. Meanwhile, the emissivity of the structure in the wavelength ranges of $3-5\ \mu$m and $8-12\ \mu$m (atmospheric windows) is suppressed considering the average amount of absorption occurred below 0.10. Later, we extend the functionality of design I to cover the possible threats in the SWIR range (design II). The results indicate that a near perfect absorption is acquired in a broadband spectrum spanning from 929 nm to 1472 nm (SWIR range), together with a narrowband absorption peak at 5750 nm (atmospheric absorption window). Finally, a real-time tuning of the infrared response using external electrostatic bias is added to the system by embedding graphene layers. It is also shown that an undesired resonance wavelength at the absorption spectrum related to the intrinsic vibrational modes (optical phonons) of the SiO_2 layer within the LWIR range is reduced by adding a single-layer graphene. Moreover, the amount of reduction is significantly enhanced in the case of embedding a three-layer graphene. In other words, the amount of absorption of the LWIR response for the three-layer graphene device is decreased by 53.19%, compared to 25.53% for the single-layer graphene one. The performances of the proposed structures are validated using rigorous coupled-wave analysis (RCWA) as an analytical method [185], besides a finite-differences time domain solver (FDTD) as a numerical method [108]. In addition, the thermal characteristic performances of design I and design II (without/with graphene layers) are validated by calculating spectral radiant

emittance at different temperatures.

4.2. Design I

4.2.1. Results and Discussions

The schematic diagram of the proposed nanoantenna emitter (design I) is shown in Fig. 4.1(a). The unit cell consists of two metallic silver (Ag) layers: a bottom reflector (optically thick with no transmission in our analysis range) and a top grating array, with an insulator layer of SiO_2 (silicon dioxide) sandwiched in between. The Ag film is selected as the primary thermal radiation layer because of its unique radiation properties [168], while the SiO_2 spacer layer is added to match the selective emissions to the impedance of the air. The analytical (RCWA) and numerical (FDTD) approaches are utilized to investigate the optical properties of the proposed nanoantenna emitter, when the structure is normally illuminated by an x-polarized (p-polarization) uniform plane-wave propagating along the $-z$ direction. In the simulations, the frequency-dependent refractive indices of Ag and SiO_2 are taken into account from the CRC Handbook of Chemistry and Physics [186] and the Palik model database [115], respectively. Then, based on the utilized simulation approaches, the geometrical parameters as explicitly presented in Fig. 4.1(a) are optimized in such a way that the excited resonances in the absorption spectrum match the atmospheric absorption windows. As a result, the thickness of the top nanograting Ag layer is $t_{\mathrm{Ag}} = 160$ nm while its width is considered $w_{\mathrm{Ag}} = 1220$ nm, and the thickness of the SiO_2 layer is set to be $t_{\mathrm{SiO_2}} = 20$ nm. The period of the unit cell is considered to be $p = 1365$ nm along the x direction. The absorptivity of design I with respect to the wavelength is presented in Fig. 4.1(b), where the analytical and numerical approaches are in good agreement with each other. The results unveil that the fourth resonance [λ_4 in Fig. 4.1(b)] is due to intrinsic vibrational modes (optical phonons) of the SiO_2 layer in the LWIR range [187] since the resonance is suppressed by considering a constant relative permittivity ($\varepsilon_{SiO_2} \simeq 2.15$) valid below the wavelength of 8 μm, as shown in Fig. 4.1(b).

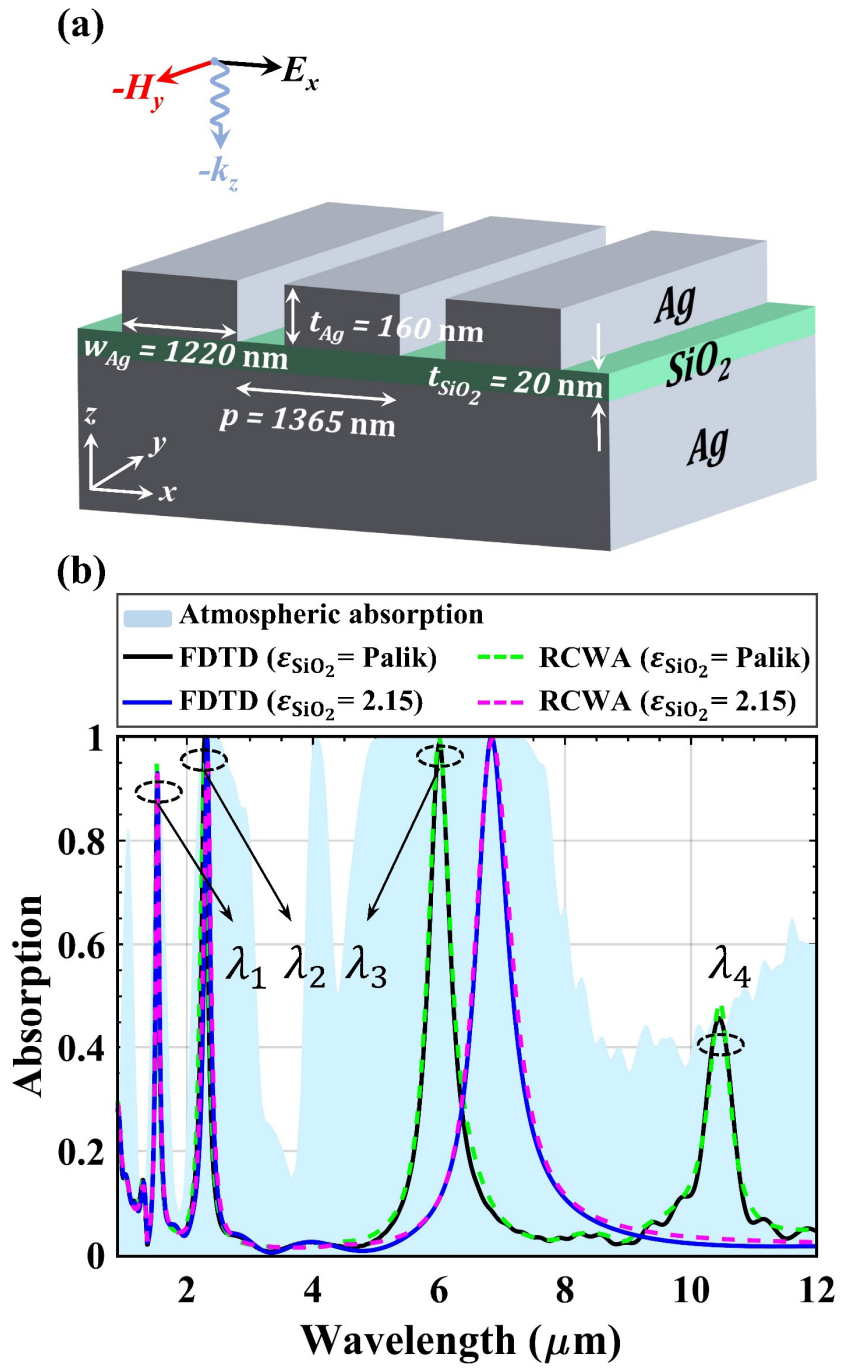

Figure 4.1. (a) Schematic unit cell of the proposed wavelength-selective nanoantenna emitter (design I). (b) Spectral absorption responses of design I obtained by considering constant and frequency-dependent values for the permittivity of the SiO_2 layer. The atmospheric absorption band [shown as the light blue area] is modeled by the US standard atmosphere compositions at the vertical distance of 5 km.

The other triple narrowband perfect absorptions are successfully achieved at the resonant peaks of $\lambda_1 = 1524$ nm, $\lambda_2 = 2279$ nm and $\lambda_3 = 6000$ nm [see Fig. 4.1(b)]. These

resonances are in very good agreement with the atmospheric spectrum [shown as the light blue area in Fig. 4.1(b)], while showing remarkable low average emissivity in the atmospheric windows (i.e., $\varepsilon_{3-5\,\mu\mathrm{m}}$ and $\varepsilon_{8-12\,\mu\mathrm{m}} \leq 0.10$). Therefore, the thermal radiation of the wavelength-selective design can be greatly absorbed by the atmosphere, which makes the coated object hidden to infrared detectors. The atmospheric spectrum is obtained from [188] where the atmospheric absorption is modeled by considering the US standard atmosphere compositions at the vertical distance of 5 km.

4.2.2. Physical mechanism

The physical behavior of design I is analyzed at the resonance wavelengths to determine the types of supported modes by the structure. Therefore, the calculated total electric- and magnetic-field distributions are presented in Fig. 4.2(a)-(f). At the resonance wavelengths of λ_1, λ_2, and λ_3 shown in Fig 4.2(a)-(f), the presented electric and magnetic mode profiles are mostly concentrated within the thin spacer layer, due to the formation of gap surface plasmon (GSP) resonances [98], [189]–[193]. The GSP resonator, being composed of a thin SiO_2 layer sandwiched between the top Ag grating array and bottom Ag substrate, experiences multiple reflections from the termination of the MIM structure. This results in a lateral standing-wave type resonance between the metallic terminations and oscillating antiparallel electric currents in the two metallic layers [193]. Therefore, GSP resonances can be described by a simple Fabry-Perot resonator formula [191], [192]

$$w_{\mathrm{Ag}} \frac{2\pi}{\lambda_0} n_{\mathrm{GSP}} + \varphi = m\pi, \qquad (1)$$

where w_{Ag} as mentioned before denotes the width of the top nanograting array, λ_0 is the wavelength of the free space, n_{GSP} is the real part of the effective mode index, φ is the additional phase acquired upon its reflection at the termination of the structure, and m is an integer showing the order of the GSP mode. According to Fig. 4.2, the electric field distribution at the resonance wavelength of λ_1 demonstrates the excitation of fifth-order mode ($m = 5$) within the spacer layer, while the electric-field mode profiles at the resonance wavelengths of λ_2, and λ_3 correspond to the excitation of the third-order ($m = 3$) and first-order ($m = 1$) modes, respectively [193]. The calculated total magnetic-field

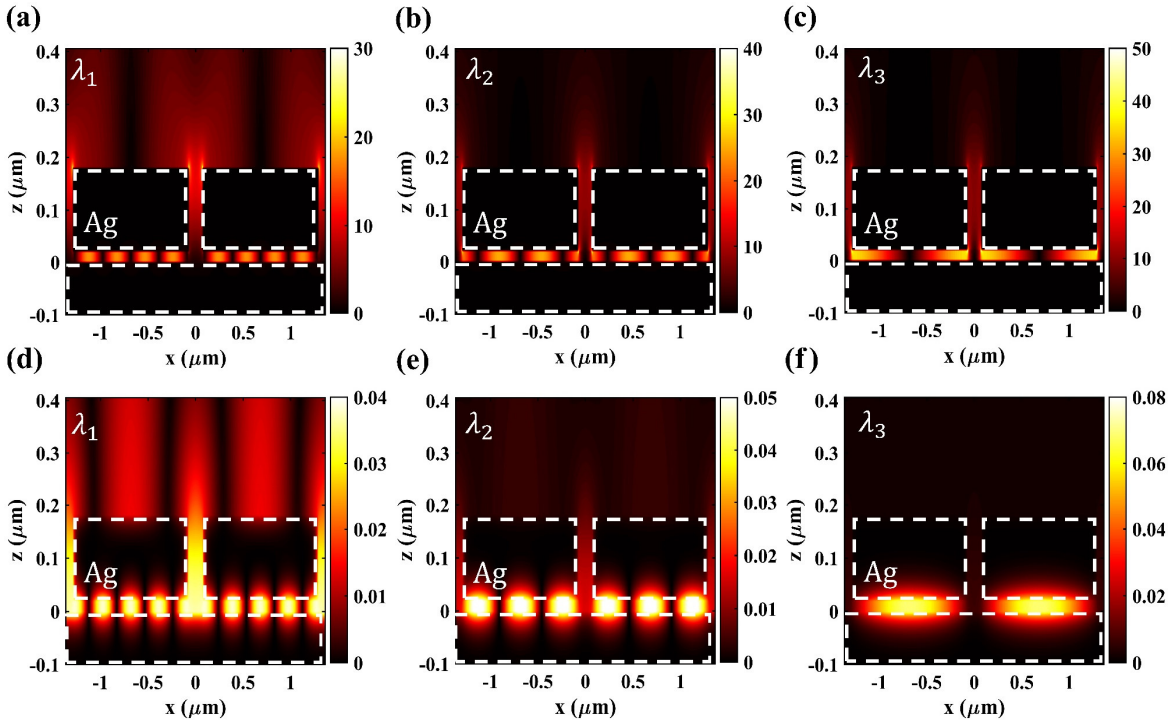

Figure 4.2. Absolute values of the total electric- and magnetic-field distributions on the x − z plane obtained for a two-unit cell of design I at the resonance wavelengths of (a, d) $\lambda_1 = 1524$ nm, (b, e) $\lambda_2 = 2279$ nm, and (c, f) $\lambda_3 = 6000$ nm, respectively. In all the figures, dashed white lines represent the Ag area.

distributions depicted in Figs. 4.2(d)-(f) also validate the type of the GSP-based resonances. In the fifth mode, anti-parallel currents in the top Ag nanograting and the bottom metallic layer create five anti-nodes of the magnetic fields inside the thin spacer layer. Accordingly, the third and first modes are due to the formation of three and first anti-nodes of the magnetic fields in the spacer layer, respectively. From the electric- and magnetic-field distributions given in Fig. 4.2(a) and Fig. 4.2(d), it is observed that surface plasmons (SPs) are also excited between the air and the top Ag nanograting, and localized around the grating corners between the adjacent unit cells, creating an SP-induced light absorption at λ_1. Therefore, the origin of λ_1 is due to the formation of both SP and GSP resonances. While λ_2 and λ_3 are due to the excitations of GSP resonances. These facts can also be illustrated by calculating the absorbed-power densities given in Fig. 4.3. Figure 4.3(a) demonstrates that a small amount of absorption within the groove and the absorption between the top and bottom Ag layers are attributed to the combinations of both SP and GSP resonances at the resonance wavelength of λ_1. Furthermore, the

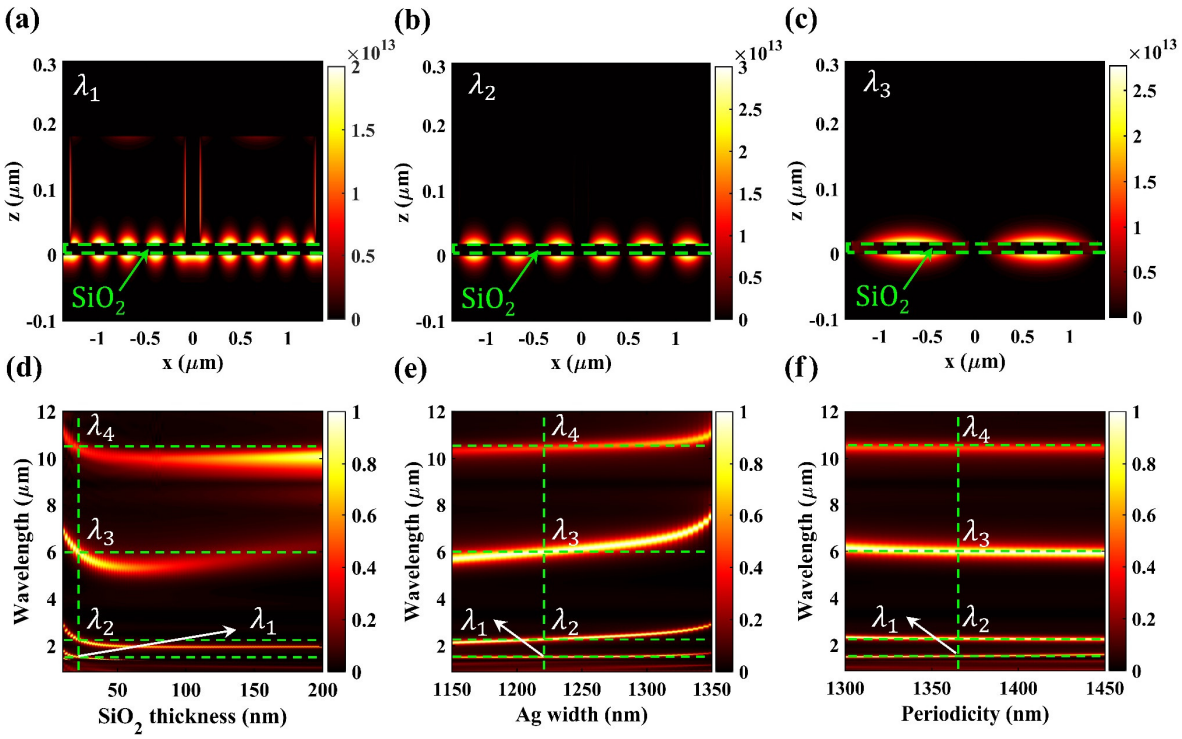

Figure 4.3. Absolute values of the absorbed-power densities on the x − z plane obtained for a two-unit cell of design I at the resonance wavelengths of (a) $\lambda_1 = 1524$ nm, (b) $\lambda_2 = 2279$ nm, and (c) $\lambda_3 = 6000$ nm. In all the figures, dashed green lines represent the SiO_2 area. (d) Simulated contour plot of absorptivity as a function of wavelength for different thicknesses of the spacer (t_{SiO_2}) [10 nm $\leq t_{SiO_2} \leq$ 200 nm when $t_{Ag} =$ 160 nm, $w_{Ag} = 1220$ nm, and $p = 1365$ nm]. (h) Simulated contour plot of absorptivity versus wavelength for different widths (w_{Ag}) of the top Ag nanograting layer [1150 nm $\leq w_{Ag} \leq$ 1350 nm when $t_{SiO_2} =$ 20 nm, $t_{Ag} = 160$ nm, and $p = 1365$ nm]. (f) Simulated contour plot of absorptivity versus wavelength for different periodicities (p) of the structure [1300 nm $\leq p \leq$ 1450 nm when $t_{SiO_2} = 20$ nm, $t_{Ag} = 160$ nm, and $w_{Ag} = 1220$ nm]. The interaction points of the dashed green lines correspond to the resonance wavelengths of $\lambda_1 = 1524$ nm, $\lambda_2 = 2279$ nm, $\lambda_3 = 6000$ nm, and $\lambda_4 = 10450$ nm.

absorbed power densities, given in Fig. 4.3(b) and Fig. 4.3(c), demonstrate that the most amount of absorption occurred between the top and bottom Ag layers (both interfaces of the dielectric layer), confirming the types of the resonance wavelengths of λ_2 and λ_3 are due to the excitation of GSPs.

4.2.3. Geometric parameters effects

The impact of changes of t_{SiO_2}, w_{Ag}, and p on the overall absorption spectrum of design I

is examined. Figure 4.3(d) represents the contour plot of absorptivity versus the wavelength for the different thicknesses of the spacer (t_{SiO_2}), while the other parameters of the structure are kept at their optimal values [$10\ \text{nm} \leq t_{SiO_2} \leq 200\ \text{nm}$ when $w_{Ag} = 1220\ \text{nm}$, $t_{Ag} = 160\ \text{nm}$ and $p = 1365\ \text{nm}$]. The results illustrate triple narrowband perfect absorptions that are sensitive to the variation of the thickness of the spacer as it increases from 10 nm to 200 nm. Increasing and getting far away from the optimized thickness value of the spacer (i.e., $t_{SiO_2} = 20\ \text{nm}$, by considering the fact that the perfect absorption threshold is above 0.9) leads to a reduction in the amount of absorption, while the fourth resonance at longer wavelengths is efficiently excited by moving from a thinner to a thicker spacer. It is evident from Fig. 4.3(d) that all the resonances are a function of the thickness of the spacer. In other words, by changing the thickness of SiO_2 from 50 nm to 10 nm, the resonance wavelengths are red-shifted toward the longer wavelength regions. This behavior of the resonances is in good agreement with the concept of GSP modes [190]. Therefore, according to the electric- and magnetic-field confinements within the spacer as shown in Figs. 4.2(a)-(f), all resonances more or less are affected by the thickness variation of the SiO_2 layer. The normalized contour plot absorptivity response of the design I for different widths of the top Ag nanograting layer is shown in Fig. 4.3(e). The Ag width is swept from 1150 nm to 1350 nm, while the thickness of SiO_2 is kept at its optimal value ($t_{SiO_2} = 20\ \text{nm}$). The resonance wavelengths of λ_2 and λ_3 are smoothly red-shifted by moving toward a wider grating. The red-shifted behavior of the resonances obtained by increasing the width of the top Ag nanograting are in complete agreement with the FP formula given in equation (1) [189]. As a result, it is almost possible to linearly tune the resonances of the nanoantenna emitter by changing the width of Ag nanograting. However, the resonance position of λ_1 is almost unaffected by increasing the width of the top Ag nanograting, confirming that the first resonance is excited by the combination of GSP and SP resonances. Figure 4.3(f) shows the variation of absorptivity versus wavelength at different values of the nanograting periodicity, while the other parameters are kept at their optimized values [$1300\ \text{nm} \leq p \leq 1450\ \text{nm}$ when $t_{SiO_2} = 20\ \text{nm}$, $w_{Ag} = 1220\ \text{nm}$, and $t_{Ag} = 160\ \text{nm}$]. As expected, the periodicity does not affect the position of the GSP-based resonances as explained in [194], [195].

All in all, it is concluded that at specific dimensions (20 nm/1220 nm/1365 nm for $t_{SiO_2}/w_{Ag}/p$), the incident electromagnetic waves can dominantly couple to GSP modes which lead to a high amount of absorption at the resonance wavelengths of λ_1, λ_2, and λ_3.

4.2.4. Power analysis

To evaluate the thermal performance of the proposed nanoantenna emitter (design I), we calculate the spectral radiant emittance of a blackbody, a conventional surface, and the selective nanoantenna emitter at different temperatures. Planks' law which describes the spectral radiance emitted by a blackbody in thermal equilibrium is given by

$$P(\lambda, T) = 2\pi hc^2/\lambda^5 \left(\exp\left(\frac{hc}{\lambda k_B T}\right) - 1\right)^{-1}, \qquad (2)$$

where k_B is Boltzmann's constant, c is the speed of light in vacuum, and λ is the wavelength of the incident light. The IR signatures of the conventional surface $[CS(\lambda, T) = P(\lambda, T) \times (1 - \varepsilon_{\text{atmosphere}}(\lambda, T))]$ and the selective nanoantenna emitter $[NE(\lambda, T) = P(\lambda, T) \times (1 - \varepsilon_{\text{atmosphere}}(\lambda, T)) \times \varepsilon_{\text{structure}}(\lambda, T)]$ can be obtained from the data of the atmospheric absorption $[\varepsilon_{\text{atmosphere}}(\lambda, T)]$ and the calculated emissivity of design I $[\varepsilon_{\text{structure}}(\lambda, T)]$, respectively. Figure 4.4(a) compares the calculated IR signatures of the conventional surface and the selective nanoantenna emitter with the spectral radiant emittance of the blackbody radiation at $300\ K$ by considering the radiation energy emitted from the normal direction. The IR signatures of the selective nanoantenna emitter at the room temperature in the MWIR and LWIR ranges are reduced by 99.71%, and 94.76% compared to the blackbody radiation, respectively. While the selective nanoantenna emitter can reduce the radiant energy by 96.09% throughout the entire wavelength band. As the temperature increases to $400\ K$ and $500\ K$, as shown in Fig. 4.4(b) and Fig. 4.4(c), the reduction rates of IR signatures for the selective nanoantenna emitter in the MWIR and LWIR ranges decrease but are still higher than 95%. Notably, the reduction rate of the selective nanoantenna emitter is greater than 96% across a wide temperature varying from room temperature to $500\ K$ for the entire wavelength range. Using the relation

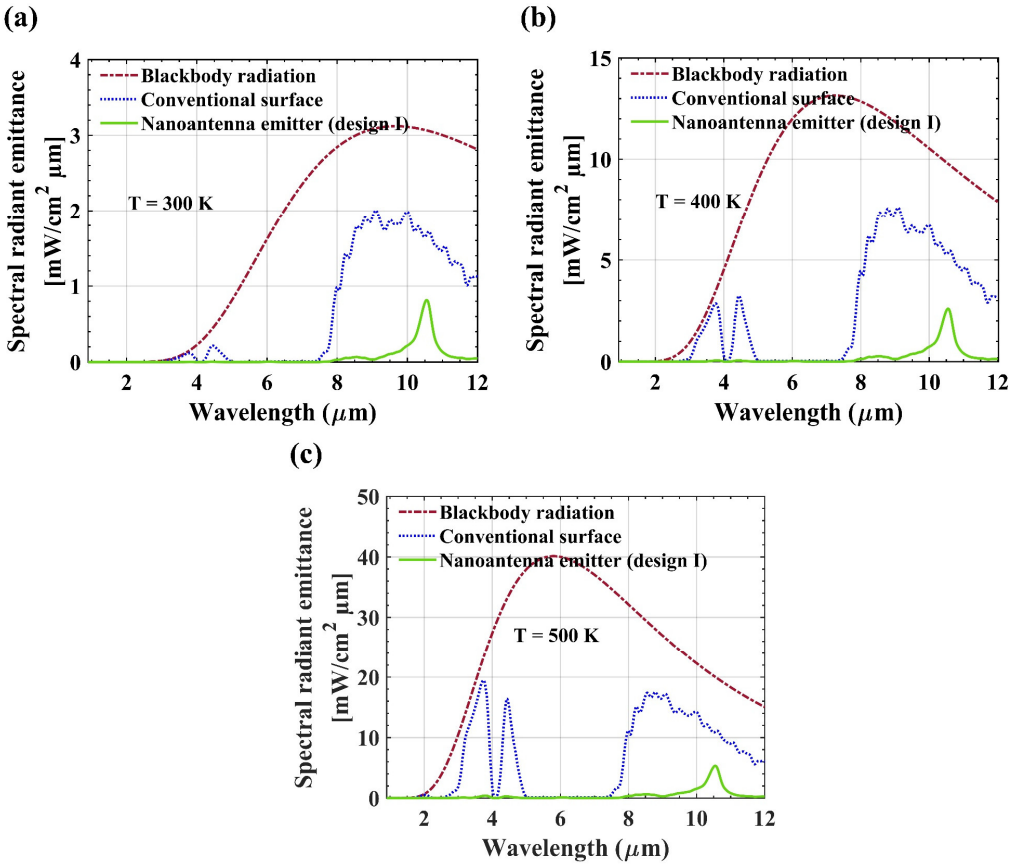

Figure 4.4. IR signatures of a blackbody, a conventional surface, and the selective nanoantenna emitter (design I) at different temperatures of (a) 300 K, (b) 400 K, and (c) 500 K.

$$\text{Reduction rates} = \sqrt{\frac{\sum_{i=1}^{n}|P(\lambda_i, T) - NE(\lambda_i, T)|^2}{\sum_{i=1}^{n}|P(\lambda_i, T)|^2}} \qquad (3)$$

the reduction rates of the selective nanoantenna emitter (design I) in the wavelength ranges of $3-5$ μm, $8-12$ μm, and the entire band for different temperatures are calculated and shown in Table 1.

Table 1. The reduction rates of the selective nanoantenna emitter (design I).

	$3-5$ μm	$8-12$ μm	$0.9-12$ μm
$T = 300$ K	99.71%	94.76%	96.09%
$T = 400$ K	99.61%	95.23%	97.71%
$T = 500$ K	99.53%	95.55%	98.68%

4.3. Design II

4.3.1. Results and Discussions

In the next section of this study, we extend the functionality of design I to provide multifunctional operations including different thermal camouflage scenarios. The extended structure is called design II. The overall detection scenario of a hot object is schematically explained in Fig. 4.5(a). To hide from these surveillance devices, the surface of the object should be decorated with the proposed GSP-based nanoantenna emitters. Unlike MWIR and LWIR mode cameras that detect blackbody photons emitted from the object, SWIR mode cameras detect solar reflectance from the surface. Therefore, in an ideal scheme, the camouflage design should also perform as a broadband absorber in the $900 - 1700$ nm range. To achieve a broadband absorption within the near-infrared (NIR) region and the main atmospheric absorption window, design I is modified with a highly lossy Titanium (Ti) layer [196] embedded on an SiO_2 layer and extended to design II with a multi-layer grating as presented in Fig. 4.5(a). The thickness of each layer of grating is optimized and set to be $t_{\mathrm{Ag}} = 70$ nm, $t'_{\mathrm{SiO_2}} = 180$ nm, and $t_{\mathrm{Ti}} = 5$ nm, respectively. The thickness of the insulator substrate which supports GSPs is considered as $t_{\mathrm{SiO_2}} = 30$ nm. The unit cell is periodically arranged along the x direction with $p = 1200$ nm, and the corresponding unit cell width is $w = 1160$ nm. Furthermore, the MIM grating structure in design II is separated by graphene layers from the substrate. The 2-D graphene layers (single- or three-layer graphene) are added for the manipulation of the surface conductivity at the mid-infrared (MIR) region to have a real-time tunability in the infrared response of the structure within the atmospheric absorption window and quench the LWIR mode response, specifically the fourth resonance occurred in design II (λ'_4) due to intrinsic vibrational modes (optical phonons) of the SiO_2 layer. The surface conductivity (σ_s) of a monolayer graphene in the simulations follows the well-established Kubo formula with intra-band (σ_{intra}) and inter-band (σ_{inter}) contributions as [197],

$$\sigma_s = \sigma_{\mathrm{intra}} + \sigma_{\mathrm{inter}}, \tag{4}$$

$$\sigma_{\mathrm{intra}} = -j\frac{e^2 k_B T}{\pi\hbar^2(\omega - j2\Gamma)}\left[\frac{\mu_c}{k_B T} + 2\ln\left(e^{-\mu_c/k_B T} + 1\right)\right], \tag{5}$$

$$\sigma_{\text{inter}} \simeq \frac{-je^2}{4\pi\hbar} \ln\left(\frac{2|\mu_c| - (\omega - j2\Gamma)\hbar}{2|\mu_c| + (\omega - j2\Gamma)\hbar}\right), \qquad (6)$$

where T, e, $\hbar$ and k_B are representing the temperature, electron charge, Planck's and Boltzmann's constants, respectively. In addition, μ_c and 2Γ ($2\Gamma = \frac{\hbar}{\tau}$, τ is the electron-phonon relaxation time) are the chemical potential and scattering rate of a monolayer graphene accounting for the Fermi energy (E_F) level and the intrinsic losses, respectively. One of the main advantages of using graphene is that its Fermi level can be easily tuned over a wide range by applying an external gate voltage (electrostatic biasing), leading to different surface conductivities. Therefore, it is possible to tune the MIR resonance of design II and reduce the peak absorption of the fourth resonance by varying the Fermi level via electrostatic biasing. The relation between Fermi energy level and the electrostatic biasing is given by an approximate closed-form expression as [198]

$$E_F = \hbar v_F \sqrt{\frac{\pi C_d V_g}{e}}, \qquad (7)$$

where $C_d = \varepsilon_d \varepsilon_0 / t_s$ is the electrostatic gate capacitance, t_s is the thickness of gate oxide, V_g is the applied gate voltage, and v_F is the Fermi velocity (1.0×10^6 m/s in graphene), respectively. As a result, the electrostatic biasing of the graphene layers in design II can be achieved by placing conductive contacts between the graphene and the bottom Ag reflector (electrostatic ground) and applying a gate voltage. The bias then allows for controlling the chemical potential of graphene layers independently [198], [199].

The simulated absorption spectra of design II including different cases are presented in Fig. 4.5(b) when $\Gamma = 0.0032$ eV and $T = 300$ K. The extension of design I to design II *without a graphene layer* leads to having a broadband resonance (λ_1') with a perfect absorption ranging from 929 nm to 1472 nm (suitable for solar applications [200], [201]), where three narrowband absorptions at the longer wavelengths of $\lambda_2' = 2080$ nm, $\lambda_3' = 5750$ nm, and $\lambda_4' = 10260$ nm are excited [see Fig 4.5(b)]. According to the monolayer graphene characteristic [202], [203], the obtained broadband response of design II should stay almost unchanged in the NIR region, while the λ_3' and λ_4' resonances at the MIR region experience blue-shifts by adding the single-layer graphene and increasing μ_c from0.2 eV to 0.6 eV. In addition, the amount of absorption at the λ_4' resonance, caused

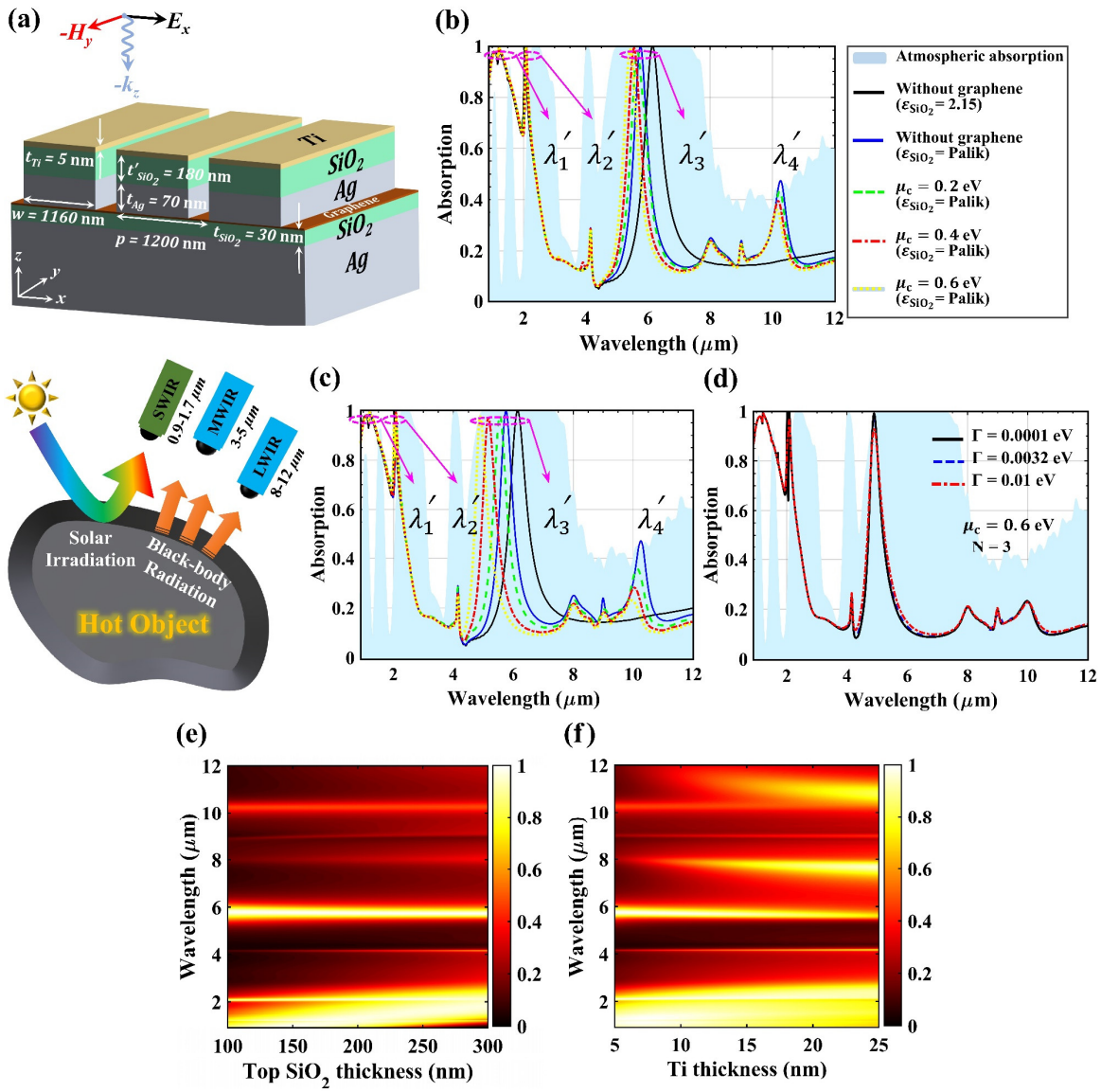

Figure 4.5. (a) Schematic diagram of the extended nanoantenna emitter (design II) and the overall detection scenario of a hot object. (b) Spectral absorption of design II without/with a single-layer (N = 1) graphene when μ_c = 0.2 eV, 0.4 eV, and 0.6 eV at T = 300 K. (c) Spectra absorption of design II without/with a three-layer (N = 3) graphene when μ_c = 0.2 eV, 0.4 eV, and 0.6 eV at T = 300 K. (d) The simulated absorption spectrum of design II with different values of scattering rate for the three-layer (N = 3) graphene case when μ_c = 0.6 eV at T = 300 K. Simulated normalized contour plots of absorptivity versus wavelength for different thicknesses of (e) the top SiO_2 layer [100 nm ≤ t'_{SiO_2} ≤ 300 nm when t_{Ag} = 70 nm, t_{Ti} = 5 nm, t_{SiO_2} = 30 nm, w = 1160 nm, and p = 1200 nm], and (f) the thickness of Ti layer [5 nm ≤ t_{Ti} ≤ 25 nm when t_{Ag} = 70 nm, t'_{SiO_2} = 180 nm, t_{SiO_2} = 30 nm, w = 1160 nm, and p = 1200 nm].

by the vibrational modes of SiO_2 layer, decreases by 25.53% [see the trend between the

blue and yellow dot lines in Fig. 4.5(b)] *for those cases without the graphene layer and with the single-layer graphene*, when μ_c is 0.6 eV. This is due to the fact that a partial amount of power is reflected back from the single-layer graphene and the localization of the electric field decreases within the lower SiO_2 layer. As several works have been reported to effectively design few-layer graphene structures for tuning the resonances at the MIR region [204], [205], we next demonstrate the optical performance of design II for the case of the three-layer ($N = 3$) graphene. Here, it is taken into consideration that the surface conductivity (σ_s) for N-layer graphene is defined as $N\sigma_s$ [206]. Figure 4.5(c) shows the resonance wavelengths of the three-layer graphene device obtained from FDTD method as a function of μ_c ranging from 0.2 eV to 0.6 eV. The resonance wavelengths exhibit a similar trend as observed in the single-layer structure in terms of blue-shifting of the MIR resonances and reducing the peak absorption of the fourth resonance. It is observed in Fig. 4.5(c) that increasing the number of graphene layers from $N = 1$ to $N = 3$ can further shift the MIR resonance wavelengths toward the shorter wavelength regions. In addition, *compared to the case without the graphene layer, the structure containing the three-layer graphene with* $\mu_c = 0.6$ eV, can suppress the λ_4' absorption peak by 53.19% [see the trend between the blue and yellow dot lines in Fig 4.5(c)]. The *three-layer graphene* device also suppresses the λ_4' absorption peak ~ 2.1 times more than the one obtained by the *single-layer graphene* structure. It should be noted that the general functionality of design II with graphene layers is negligibly affected for different values of scattering rate as demonstrated for the three-layer graphene device in Fig. 4.5(d) when the chemical potential is assumed 0.6 eV. This means that variation of scattering rate due to the impurities, defects, and interfaces for realistic graphene layers [207], [208] does not affect the response of the proposed structure. All in all, the absorption spectra of design II perfectly match the atmospheric absorption windows with tunability characteristic [209] that make it suitable for different thermal camouflage scenarios as well as solar energy harvesting application due to the broadband absorption within a wide spectral range of the NIR region. The absorption resonance wavelengths of design II, together with the peak values of the fourth resonance and the corresponding relative reduction rates are all.

Table 2. Absorption resonance wavelengths of the proposed wavelength-selective nanoantenna emitter (design II) without a graphene layer, with a single-layer graphene, and a three-layer graphene (at different chemical potentials: μ_c = 0.2 eV, 0.4 eV, and 0.6 eV at $T = 300\ K$), together with peak values of the fourth resonance and the corresponding relative reduction rates obtained via comparing the results with design II without a graphene layer.

		Resonance				Intensity of #4 and reduction rates	
		#1	#2	#3	#4		
Design II (without a graphene layer)		$\lambda_1' = 929 - 1472$ nm	$\lambda_2' = 2080$ nm	$\lambda_3' = 5750$ nm	$\lambda_4' = 10260$ nm	0.47	
Design II (with a single-layer graphene)	$\mu_c = 0.2$ eV	$\lambda_1' = 929 - 1472$ nm	$\lambda_2' = 2080$ nm	$\lambda_3' = 5656$ nm	$\lambda_4' = 10234$ nm	0.43	−8.51%
	$\mu_c = 0.4$ eV	$\lambda_1' = 929 - 1472$ nm	$\lambda_2' = 2080$ nm	$\lambda_3' = 5551$ nm	$\lambda_4' = 10184$ nm	0.39	−17.02%
	$\mu_c = 0.6$ eV	$\lambda_1' = 929 - 1472$ nm	$\lambda_2' = 2080$ nm	$\lambda_3' = 5432$ nm	$\lambda_4' = 10147$ nm	0.35	−25.53%
Design II (with a three-layer graphene)	$\mu_c = 0.2$ eV	$\lambda_1' = 929 - 1472$ nm	$\lambda_2' = 2080$ nm	$\lambda_3' = 5555$ nm	$\lambda_4' = 10135$ nm	0.35	−25.53%
	$\mu_c = 0.4$ eV	$\lambda_1' = 929 - 1472$ nm	$\lambda_2' = 2080$ nm	$\lambda_3' = 5170$ nm	$\lambda_4' = 10032$ nm	0.28	−40.42%
	$\mu_c = 0.6$ eV	$\lambda_1' = 929 - 1472$ nm	$\lambda_2' = 2080$ nm	$\lambda_3' = 4896$ nm	$\lambda_4' = 9957$ nm	0.22	−53.19%

summarized in Table 2.

4.3.2. Geometric parameters effects

In order to investigate the performance of each layer and their contributions to the resonances, we once again examine how changes in t'_{SiO_2}, and t_{Ti} can affect the overall absorption spectrum of design II without considering the graphene layer. Figure 4.5(e) shows the dependence of the normalized absorbed power by the structure on the changes of t'_{SiO_2}, while keeping all of the other geometrical parameters unchanged [$100\ \text{nm} \leq t'_{SiO_2} \leq 300$ nm when $t_{Ag} = 70$ nm, $t_{Ti} = 5$ nm, $t_{SiO_2} = 30$ nm, $w = 1160$ nm and $p = 1200$ nm]. The result exhibits a broadband perfect absorption at the NIR region [with a peak absorption at (λ_1')] and a sharp narrowband response (λ_3') at the atmospheric absorption window for all t'_{SiO_2} values, where only the former resonance experiences a redshift as the spacer thickness increases. This phenomenon demonstrates that the NIR response (λ_1') is due to the added top layers to the system, while the wavelength resonances
including λ_2' and λ_3' are due to the formation of gap plasmons (similar to design I) in the

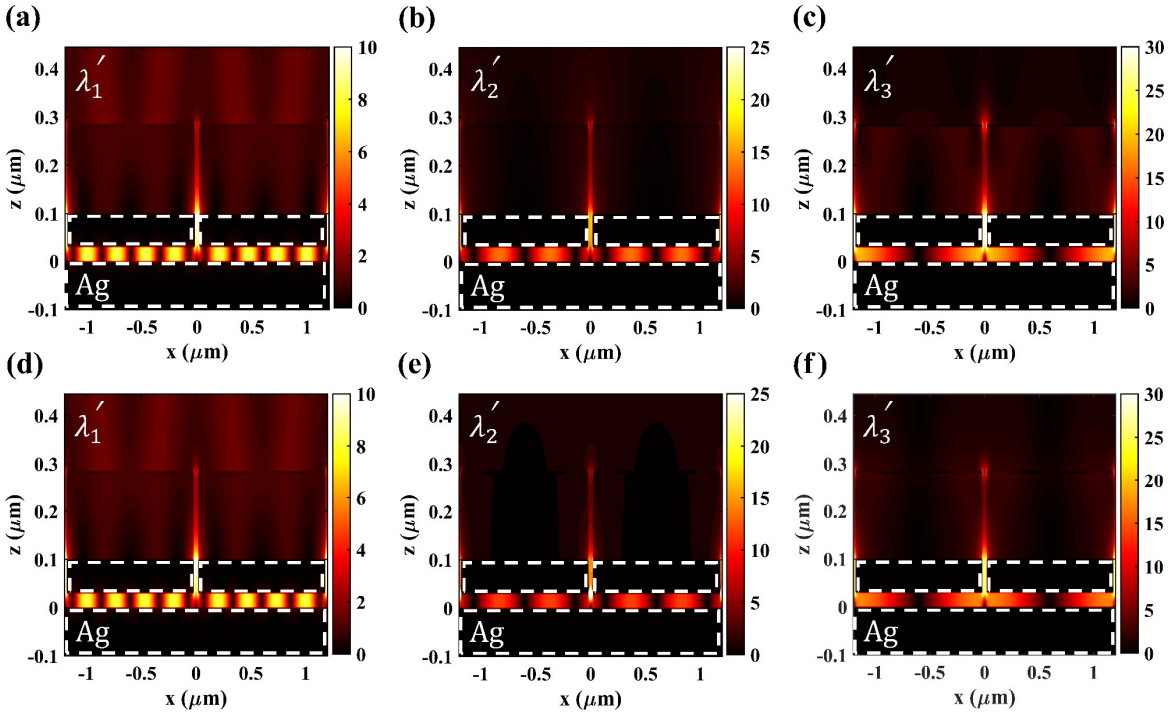

Figure 4.6. Absolute values of the total electric-field distributions on the x − z plane obtained for a two-unit cell of design II (without graphene layers) at the resonance wavelengths of (a) $\lambda_1' = 1205$ nm, (b) $\lambda_2' = 2080$ nm, and (c) $\lambda_3' = 5750$ nm, respectively. Absolute values of the total electric-field distributions on the x − z plane obtained for a two-unit cell of design II (with the three-layer graphene when $\mu_c = 0.6$ eV) at the resonance wavelengths of (d) $\lambda_4' = 1205$ nm, (e) $\lambda_4' = 2080$ nm, and (f) $\lambda_4' = 4896$ nm, respectively. In all the figures, dashed white lines represent the Ag area.

interfaces of the SiO_2 substrate and the Ag layers. To have a solar absorber operating in the NIR region with an absorption above 90%, the optimal thickness of the SiO_2 interlayer (t'_{SiO_2}) is set at 180 nm. Figure 4.5(f) shows the impact of changes in t_{Ti} on the normalized spectral absorption of design II without considering graphene layer, when it varies from 5 nm to 25 nm [5 nm $\leq t_{Ti} \leq$ 25 nm when $t_{Ag} = 70$ nm, $t'_{SiO_2} = 180$ nm, $t_{SiO_2} = 30$ nm, $w = 1160$ nm and $p = 1200$ nm]. Accordingly, the resonances around 8 μm and 10 μm are efficiently excited by moving toward thicker values of the Ti layer ($t_{Ti} > 20$ nm) besides the reduction in the amount of absorption of the resonance (λ_3') in the atmospheric absorption window. As a result, the optimal performance can be achieved with the thickness of $t_{Ti} = 5$ nm.

4.3.3. Physical mechanism

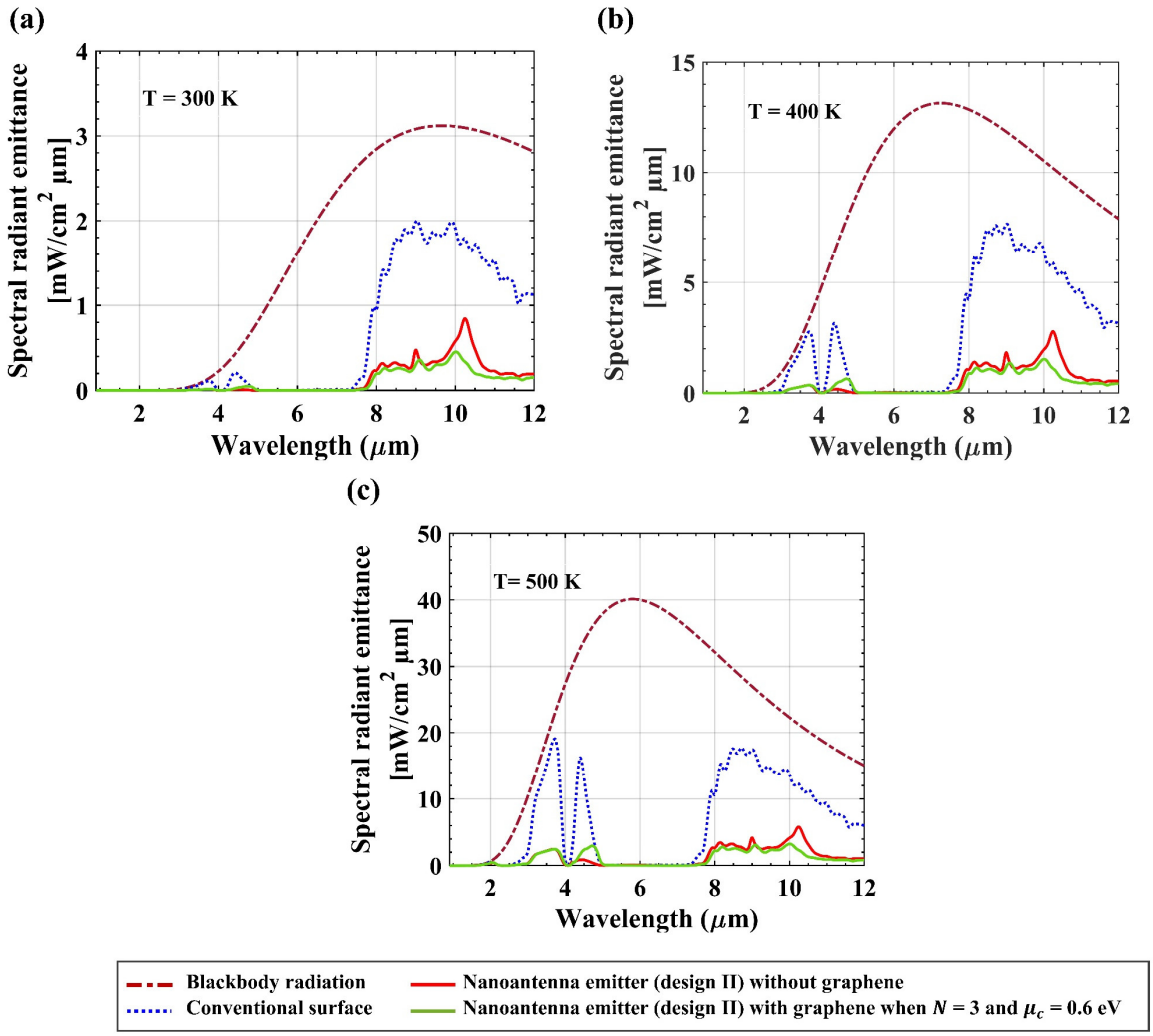

Figure 4.7. IR signatures of a blackbody, a conventional surface, and the selective nanoantenna emitter (design II without/with the three-layer graphene (N = 3) when $\mu_c = 0.6$ eV) at different temperatures of (a) 300 K, (b) 400 K, and (c) 500 K.

In order to reveal the physical mechanism of the proposed selective nanoantenna emitter (design II) under the normal incidence, electric-field distributions at the resonance wavelengths are obtained on the $x - z$ plane and illustrated in Fig. 4.6, corresponding to the cases without graphene and with the three-layer graphene ($\mu_c = 0.6$ eV). It is seen from Fig. 4.6(a) and Fig. 4.6(d) that at the resonance wavelength of $\lambda_1' = 1205$ nm, the incident light penetrates thorugh the thin Ti layer and bounces back at the bottom Ag grating layer. The two reflectors dominantly excite the Fabry-Perot (FP) cavity resonance leading to a broaden absorption response thanks to the lossy behavior of Ti in the NIR region [196].

However, the distributions of the electric-field at the other excited resonances are intrinsically different. In particular, at the resonance wavelength of $\lambda_2' = 2080$ nm presented in Fig. 4.6(b) and Fig. 4.6(e), the electric-field localizations inside the spacer layer correspond to the excitation of the third-order mode GSP resonance [98], [189]–[193], while the absorptions at the resonance wavelengths of $\lambda_3' = 5750$ nm and $\lambda_3' = 4986$ nm are dominantly attributed to the excitation of GSPs with the first-order mode. This can be seen in Fig. 4.6(c) and Fig. 4.6(f) for the design without graphene layer and the design with the three-layer graphene, respectively.

4.3.4. Power analysis

To evaluate the performances of the second nanoantenna emitter (design II) in thermal camouflage technology, we once again calculate the IR signatures of the conventional surface and the extended nanoantenna emitter (design II without/with the three-layer graphene when $\mu_c = 0.6$ eV) to compare with the spectral radiant emittance of the blackbody radiation at $300\ K$. The IR signatures in the MWIR and LWIR wavelength ranges can be reduced by 98.67% and 88.74% without considering the graphene layers as shown in Fig. 4.7(a). As the temperature increases, these two values become 97.90% and 88.64% at $400\ K$ and 96.92% and 88.65% at $500\ K$ as illustreated in Fig. 4.7(b) and Fig. 4.7(c). Meanwhile, the selective nanoantenna emitter can reduce the radiant energy by 91.50%, 94.40%, and 96.21% for the whole wavelength spectrum at $300\ K$, $400\ K$, and 500 K, respectively. Figure 4.7(a)-(c) also show the IR signatures of the selective nanoantenna emitter with the three-layer graphene when $\mu_c = 0.6$ eV. The results show better performance in terms of the reduction rate in comparison to the case without graphene layers. Table 3 summarizes the reduction rates of the selective nanoantenna emitter (design II) for all cases in the wavelength ranges $3 - 5$ μm, $8 - 12$ μm, and the entire band at different temperatures. In general, the reduction rates exhibit a similar trend for all cases such that the IR signatures decrease in the MWIR and LWIR ranges as the temperature increases, while the reduction rate for the entire wavelength range increases as the temperature increases.

Table 3. The reduction rates of the selective nanoantenna emitter (design II without/with the single- and three-layer graphene when $\mu_c = 0.2$ eV, 0.4 eV, and 0.6 eV) in the wavelength ranges of $3-5\ \mu$m, $8-12\ \mu$m, and the entire band at different temperatures.

		The reduction rates			
		Temperatures	**$3-5\ \mu$m**	**$8-12\ \mu m$**	**$0.9-12\ \mu$m**
Design II (without a graphene layer)		300 K	98.67%	88.74%	91.50%
		400 K	97.90%	88.64%	94.40%
		500 K	96.92%	88.65%	96.21%
Design II (with a single-layer graphene)	**$\mu_c = 0.2$ eV**	300 K	98.56%	89.21%	91.85%
		400 K	97.79%	89.07%	94.59%
		500 K	96.82%	89.06%	96.29%
	$\mu_c = 0.4$ eV	300 K	98.53%	89.76%	92.25%
		400 K	97.76%	89.57%	94.82%
		500 K	96.79%	89.53%	96.41%
	$\mu_c = 0.6$ eV	300 K	98.41%	90.22%	92.59%
		400 K	97.67%	90.00%	95.01%
		500 K	96.74%	89.94%	96.51%
Design II (with a three-layer graphene)	**$\mu_c = 0.2$ eV**	300 K	98.31%	90.09%	92.49%
		400 K	97.53%	89.87%	94.94%
		500 K	96.57%	89.81%	96.44%
	$\mu_c = 0.4$ eV	300 K	97.74%	91.29%	93.37%
		400 K	97.10%	91.00%	95.43%
		500 K	96.28%	90.89%	96.67%
	$\mu_c = 0.6$ eV	300 K	95.31%	92.10%	93.96%
		400 K	95.00%	91.79%	95.67%
		500 K	94.57%	91.65%	96.56%

CHAPTER 5

Diode like high-contrast asymmetric transmission of linearly polarized waves based on plasmon-tunneling effect coupling to electromagnetic radiation modes

This chapter is one part reprinted with permission from: Bahram Khalichi, Amir Ghobadi, **Ataollah Kalantari Osgouei**, Amir Ghobadi, and Ekmel Ozbay, Journal of Physics D: Applied Physics, 2021.

5.1. Introduction

Allowing the light transmission from one direction, while suppressing transmission from the opposite side is one of the popular and significant phenomena realized in various optical applications [67], [210]–[217]. This nonreciprocal optical-diode behavior [211], [212] is utilized to control one-way light transmission, increase the efficiency, and reduce the damage in the optical communication circuitry, such as isolators, rectifiers, logic circuits, and clippers. As a common approach, symmetry-broken chiral metamaterials

along with multilayer design and sophisticated structures are utilized to achieve customized and simultaneous functionalities, such as polarization-sensitive asymmetric transmission [218], [219]. This asymmetric transmission (AT) phenomenon originates from the interaction of electromagnetic radiation with the structural two-dimensional chirality in the metamaterials [220], [221]. As a result, a portion of an incident electromagnetic wave is converted to its cross-polarized counterpart for both forward and backward illuminations, while the unidirectional transmission (optical-diode like behavior) is not the goal in chiral metamaterial-based structures. In addition, the use of multilayer metallic configurations prevents obtaining a high-contrast AT ratio. Although optical devices with an AT characteristic can be realized using plasmonic metamaterials as another approach [210], [213], they usually exhibit low transmission amplitudes due to optical losses in the multilayer designs [222]–[228]. Moreover, the realization of a double grating design separated by a thin dielectric is a challenging task from the fabrication perspective [229]–[231]. Therefore, in an ideal scheme, it is required to reduce the optical loss (thinning the metallic components down to sub-wavelength geometries) while keeping the overall design simple. The excitation of surface plasmon polaritons (SPPs) over both boundaries of a thin metal slab is widely utilized in biochemical sensing applications [232]–[234], and it can be an innovative approach to be exploited in diode-like optical devices. Furthermore, based on previous reports, the outcoupling of SPP modes to radiation modes [235]–[240] with an efficiency of 50% is proposed in [240]. In addition, using a modified structure, the transmittance of 68% is reported in [239] and the enhancement of the transmittance up to 72% is predicted in [238]. Therefore, adopting this design architecture for an optical diode application could provide the opportunity to achieve high-contrast AT for narrow-band applications in the near infrared (NIR) region. In the present paper, we demonstrate a high-contrast and a narrowband optical diode that operates based on the plasmon-tunneling effect [231], [241], [242]. The proposed optical diode is made of the dielectric grating waveguide over a thin silver (Ag) layer embedded on a thick substrate. This simple geometry is significantly distinct from other available plasmonic-metamaterial-based AT devices with multilayer configurations [243], multilayer metasurfaces [244], [245], or subwavelength slits [229]. When the proposed device is illuminated by a forward incident light, the symmetric and antisymmetric

plasmonic modes are excited by the diffraction grating waveguide at the bottom and top interfaces of the thin Ag interlayer, respectively. The antisymmetric mode is coupled to radiation modes in the next environment (substrate), while the symmetric mode is absorbed inside the metallic interlayer. Since the antisymmetric SPP mode is excited on the top interface of the metallic interlayer and outcoupled to radiation modes in the next environment, a high forward transmission can be achieved based on the plasmon-tunneling effect. Contrarily, under the backward illumination, the device offers a near-zero backward transmission thanks to the strong reflection of the Ag layer.

5.2. Design Methodology, Operation Principle, and Simulation Results

A schematic diagram of the proposed structure with AT property, using the generation and outcoupling of SPPs, is presented in Fig. 5.1(a). The structure consists of a dielectric diffraction grating as a one-dimensional array on top of a same-material dielectric slab waveguide and a thin metal film, deposited onto a dielectric substrate. In Fig. 5.1(a), t_g, w_g, and Λ denote the height, width, and periodicity of the dielectric grating, respectively. The material of the dielectric grating and the dielectric slab waveguide are considered as silicon nitride (Si_3N_4) with the permittivity of 4.2025, where the thickness of the dielectric slab waveguide is represented by t_d. The dielectric slab forms a Fabry–Pérot cavity, which is used to improve the coupling efficiency. The thickness of the dielectric slab will also give us another degree of freedom on the spectral tuning of the resonance wavelengths [246]. Then, a thin Ag layer with the thickness of t_m is considered between the dielectric slab waveguide and the substrate (Silicon dioxide: SiO_2). The spectral refractive index of Ag is taken from the Johnson and Christy database [114]. Conceptually, when the proposed structure is normally illuminated by an $x-$polarized (TM-polarized wave: electric field is parallel and magnetic field is perpendicular to the plane of incidence [247] uniform plane wave, the incident wave is diffracted by the grating, and then coupled into the waveguide and SPP modes at certain resonance wavelengths (in which the guided-mode condition of the planar waveguide and the phase-matched conditions are satisfied simultaneously). These SPPs are modulated by the grating and can be outcoupled to the radiation modes in the substrate[238]. Therefore, the grating is not only responsible for

the coupling of the incident light to the SPPs, but also for outcoupling the resonant SPPs to the radiation modes. To numerically analyze this structure, the eigen-solver [to find the eigenvalues (resonance wavelengths of the entire structure) and the eigenvectors (the corresponding field distributions)] is exploited to optimize the structure to have an asymmetric transmission at a wavelength of approximately 1550 nm. Accordingly, as shown in Fig. 5.1(a), the period and the width of the dielectric grating are set to be $\Lambda = 1100$ nm and $w_g = 880$ nm, respectively, which leads the filling factor equal to 0.8. The thickness (height) of the grating (t_g) and the dielectric slab (t_d) are 260 nm and 470 nm, and t_m, the thickness of the metal film, is chosen as 20 nm to allow the excitation of both long- and short-range SPPs [28], [248]. These parameters determine the resonance wavelength location in the NIR region at approximately 1550 nm. Next, we computed the reflection, transmission spectra using the rigorous coupled-wave analysis (RCWA) as an analytical approach [249] besides the finite difference time domain (FDTD) software package as a numerical one. The calculated transmission and the reflection spectra when the structure is illuminated by an x-polarized uniform plane-wave propagating along the $\pm z$ directions (forward ($-$z) and backward ($+$z) illuminations) are given in Fig. 5.1(b). The obtained results from both methods are in good agreement with each other which demonstrate the accuracy of the simulations. As seen in this panel, the proposed structure exhibits an optical diode characteristic at a wavelength range of 1535 nm to 1563 nm (full width at half maximum: FWHM$/\lambda_0 = 2\%$). At 1549 nm, the maximum power transmission of 0.88 occurs for the forward illumination, while the backward transmission value stayed below 0.03. Therefore, the highest contrast ratio in the peak position is achieved as 14.67 dB (a ratio of about 29). To clearly scrutinize the origin of this distinct optical-diode behavior, we have to find out the nature of these resonance wavelengths. To begin with, we simplified the geometry by the explanation of the conditions for the excitation of SPP modes in an insulator–metal–insulator (IMI) design. The configuration is presented in Fig. 5.1(c), and a thin metal film with the thickness of t is considered. This configuration can support SPPs at both interfaces, where the excitation and overlapping of SPPs at both boundaries give rise to mixed modes, called symmetric and antisymmetric SPPs [28], [248]. The modes can be found by solving Maxwell's equations in each medium, and by satisfying the boundary conditions at both interfaces of the metallic layer.

As the thickness of the metal slab decreases, the two modes become more distinct, where the symmetric SPP mode exhibits a less attenuation constant and effective refractive index, while the attenuation and effective refractive index of the antisymmetric one increase [234]. Therefore, according to the attenuation and propagation lengths, the symmetric mode is referred to as a long-range SPP (LRSPP), while the antisymmetric mode is referred to as a short-range SPP (SRSPP) [28], [248]. For the analysis, a two-dimensional problem is considered (the width of the structure in the y direction is infinite so that $\partial/\partial y = 0$). The geometry can support TM^x mode (E_x, E_z and, H_y are the nonzero components). In this scenario, an $x-$directed magnetic vector potential (A_x) can be represented as [247]

$$A_x(x,z) = \begin{cases} B_1 \exp\left(-\alpha_z^{d_1} z - ik_x x\right) & z \geq \frac{t}{2} \\ [A_1 \cos(k_z^m z) + A_2 \sin(k_z^m z)] \exp(-ik_x x) & -\frac{t}{2} \leq z \leq \frac{t}{2} \\ B_2 \exp\left(+\alpha_z^{d_2} z - ik_x x\right) & z \leq -\frac{t}{2}, \end{cases} \quad (1)$$

where $\alpha_z^{d_j} (j = 1, 2)$ is the attenuation constant in the dielectric media, k_z^m is the phase constants inside the metal layer, $k_x = k_{\mathrm{L(S)RSPP}}$ is the magnitude of the SPPs wavevector, and A_j, B_j $(j = 1, 2)$ are the unknown coefficients. The corresponding electric and magnetic fields, inside the metal and dielectric regions, can be calculated by

$$E_x(x,z) = \frac{-i}{\omega \mu_0 \varepsilon_j} \left(\frac{\partial^2}{\partial x^2} + k_x^2 \right) A_x(x,z)$$

$$= \begin{cases} \frac{-iB_1}{\omega \mu_0 \varepsilon_{d_1}} \left(-k_x^2 + k_{d_1}^2\right) \exp\left(-\alpha_z^{d_1} z - ik_x x\right) & z \geq \frac{t}{2} \\ \frac{-i}{\omega \mu_0 \varepsilon_m} (-k_x^2 + k_m^2)[A_1 \cos(k_z^m z) + A_2 \sin(k_z^m z)] \exp(-ik_x x) & -\frac{t}{2} \leq z \leq \frac{t}{2} \\ \frac{-iB_2}{\omega \mu_0 \varepsilon_{d_2}} \left(-k_x^2 + k_{d_2}^2\right) \exp\left(+\alpha_z^{d_2} z - ik_x x\right) & z \leq -\frac{t}{2} \end{cases} \quad (2)$$

and

$$H_y(x,z) = \frac{1}{\mu_0}\frac{\partial}{\partial z}A_x(x,z)$$

$$= \begin{cases} \frac{B_1}{\mu_0}\left(-\alpha_z^{d_1}\right)\exp\left(-\alpha_z^{d_1}z - ik_x x\right) & z \geq \frac{t}{2} \\ \frac{1}{\mu_0}[-A_1 k_z^m \sin(k_z^m z) + A_2\, k_z^m \cos(k_z^m z)]\exp(-ik_x x) & -\frac{t}{2} \leq z \leq \frac{t}{2} \\ \frac{B_2}{\mu_0}\left(+\alpha_z^{d_2}\right)\exp\left(+\alpha_z^{d_2}z - ik_x x\right) & z \leq -\frac{t}{2}, \end{cases} \quad (3)$$

respectively. Decomposing the electric- or magnetic-field distributions in the metal layer as a combination of symmetric and antisymmetric modes and satisfying the tangential boundary conditions at the interfaces, different dispersion relations [28], [248] for the SRSPP (antisymmetric) and LRSPP (symmetric) modes are obtained as

$$\text{SRSPP:} \qquad \varepsilon_m \alpha_z^{d_1} + \varepsilon_{d_1} k_z^m \cot\left(k_z^m \frac{t}{2}\right) = 0 \qquad (4a)$$

$$\text{LRSPP:} \qquad \varepsilon_m \alpha_z^{d_2} - \varepsilon_{d_2} k_z^m \tan\left(k_z^m \frac{t}{2}\right) = 0, \qquad (4b)$$

where $-(\alpha_z^{d_j})^2 = \varepsilon_{d_j} k_0^2 - k_{\text{L(S)RSPP}}^2$, and $(k_z^m)^2 = \varepsilon_m k_0^2 - k_{\text{L(S)RSPP}}^2$. It should be noted here that the symmetric configuration of the transverse component E_z or H_y corresponds to the antisymmetric one for the longitudinal components E_x and vice versa. In addition, the z variation in the metal layer can be represented using hyperbolic functions that leads to some modifications in the final results. Based on (4), it can be concluded that SPs are excited on the top and bottom interfaces of the metal layer because of overlapping of the modes. Therefore, if the thickness of the metal film increases, the propagation constants of these two modes get closer, thereby leading to SPs on the top interface.

After a brief discussion regarding the possible excitation of different types of SPPs in IMI configuration, the nature of the resonance of the proposed optical-diode structure at the resonance wavelengths of 1549 nm and 1624 nm can be investigated. To achieve this purpose, five subsections are considered.

5.2.1. Types of resonances

Regarding the types of SPPs, the formation of two dip resonances in the reflection spectrum

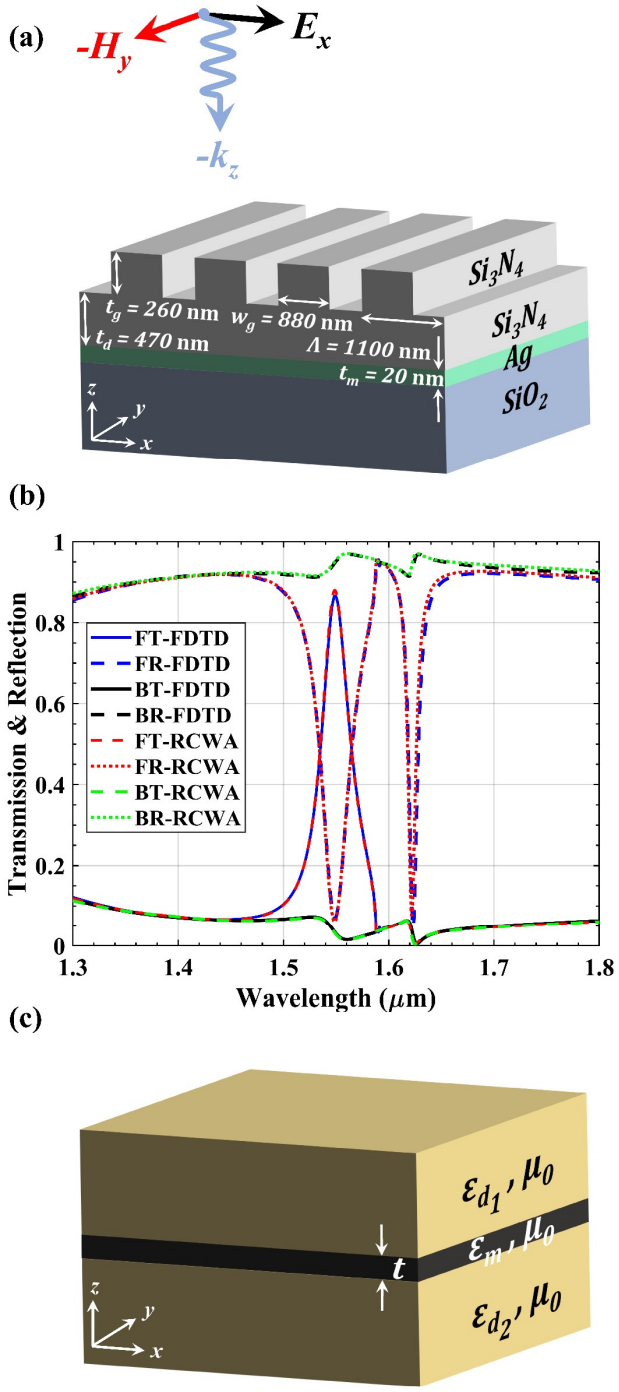

Figure 5.1. (a) Schematic diagram of the proposed optical-diode structure with a high AT characteristic designed based on dielectric diffraction grating waveguide on top of a thin metal film. The structure is normally illuminated by an x-polarized uniform plane wave from both sides. (b) Forward/backward transmission (FT/BT) and reflection (FR/BR) spectra of the proposed structure when the object is illuminated by an x-polarized uniform plane wave propagating along the ±z directions. (c) Schematic representation of a thin metal film with the thickness of t surrounded by infinite dielectric media.

belonging to the forward illumination are due to the symmetric and antisymmetric SP mode excitations that result in absorption and transmission in the structure, respectively.The types and behaviors of the mentioned dip resonances in the reflection spectrum can be illustrated by utilizing dispersion relations given in (4). Accordingly, the SPPs should be dependent on different waveguide slab (superstrate) and substrate materials. Thereby, different materials are utilized as a substrate in the following order for the average refractive indices $CaF_2 < SiO_2 < BaF_2 < Al_2O_3$ (correspond to: $1.42 < 1.44 < 1.46 < 1.74$). In Fig. 5.2(a), it is evident that, as the average refractive index of the substrate increases, there is a red shift in the position of resonances from shorter toward longer wavelengths. However, a negligible shift in the position of the first resonance compared to the second resonance is observed for different substrate materials. Clearly, the spectral separation between the modes increases by increasing the refractive index of the substrate. Based on the dispersion relations given in (4), SRSPP and LRSPP are dependent on superstrate and substrate materials, respectively. Although both SRSPP and LRSPP modes can be outcoupled to radiation modes [238], the analysis reveals that the small and large shifts corresponding to the first and second resonances are due to the SRSPP and LRSPP, respectively, and the SRSPP is tunneling and then dominantly outcoupled (induced) to the substrate, while LRSPP is the main reason for the absorption that appeared as a second resonance in the reflection spectrum. The same procedure continues for different superstrate materials and the results are separately given in Fig. 5.2(b) and Fig. 5.2(c) for the transmission and reflection spectra, respectively. It is seen that the first resonance experiences larger red shifts than the second resonance for different superstrate materials. This validates that the types of the first and second resonances are due to the excitations of SRSPP and LRSPP, respectively.

5.2.2. Near-field light-matter interactions at the resonance wavelength of 1549 nm

Near-field light-matter interactions of the proposed structure including on-resonance absolute values of electric- and magnetic-field distributions on the $x - z$ planes are shown in Fig. 5.3(a) to Fig. 5.3(d) for both-illumination sides. The electric field is partially

confined in the waveguide layer for the forward illumination and it is mainly distributed in the groove medium as presented in Fig. 5.3(a). It is also seen that the guided-mode condition in the dielectric grating waveguide is satisfied, which led to the waveguide-coupled SPP excitation, and then the outcoupling of SPPs to the radiation modes. Moreover, as depicted in Fig. 5.3(c), the magnetic field is mainly confined within the grating structure which also shows the formation of the Fabry–Pérot cavity and the excitation of SPPs for the forward illumination [82], [167], [250], [251]. Therefore, the overall resonance of the designed structure for the forward illumination is due to the pairing of photonic (Fabry–Pérot) and plasmonic (SRSPP) modes. Under backward incidence, the absolute values of electric- and magnetic-field distributions at the operating wavelength of 1549 nm represent the formation of standing waves (partial reflection) in the substrate as shown in Fig. 5.3(b) and Fig. 5.3(d), respectively. The low value of backward transmission within the operating wavelengths is due to the fact that SPPs cannot be excited under backward incidence. In other words, the proposed diode-like device is operating based on the exciting and outcoupling of SPPs to radiation modes using an optimally designed dielectric-based diffraction grating waveguide for the forward illumination. While the backward incident electromagnetic wave cannot be coupled to the SPPs since there is no configuration that is identical to the one in the front side to excite the SPPs [1]. Thereby, the structure offers strong reflection by the Ag film under backward incidence and the incident wave mostly reflects back. This results in the reciprocity breaking and obtaining a high-contrast AT response in the proposed geometry. In addition to the computed absolute values of electric and magnetic fields at the resonance wavelength of 1549 nm, the Poynting-vector distributions, which reflect the average power flow directions, are presented for the forward and backward illuminations in Fig. 5.3(e) and Fig. 5.3(f), respectively. The results demonstrate that the considerable amount of average power can reach the next environment for the forward illumination in contrast to the blockage of the power in the reverse direction.

5.2.3. Near-field light-matter interactions at the resonance wavelength of 1624 nm

Near-field light-matter interaction results, including absolute values of electric- and

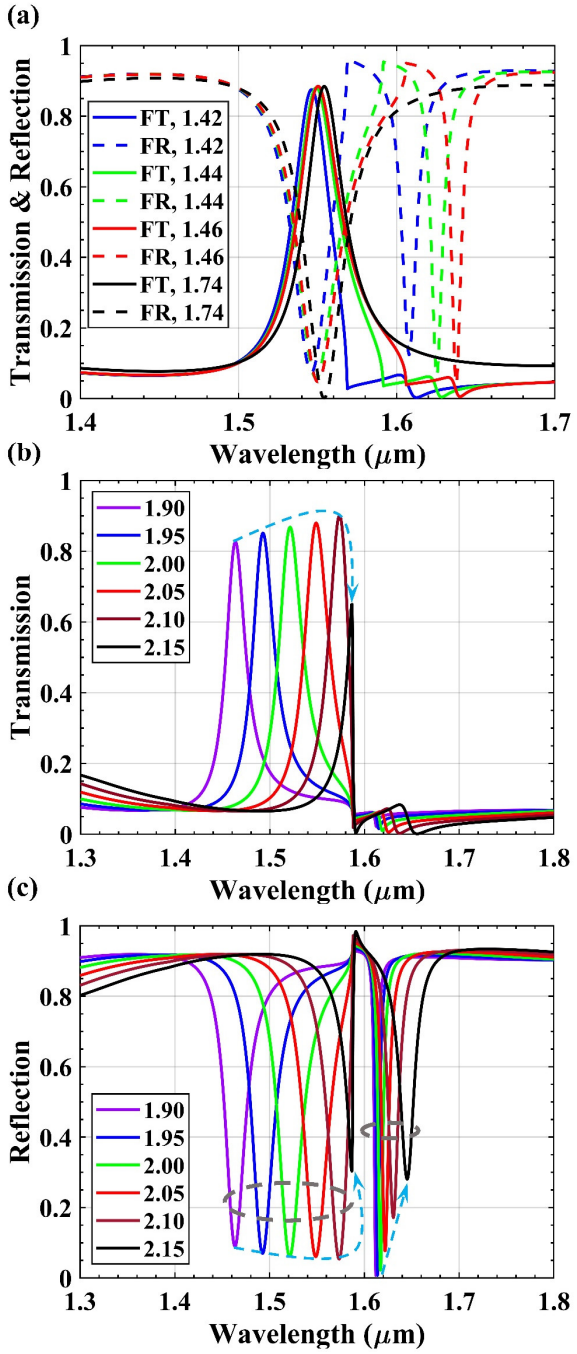

Figure 5.2. (a) Forward transmission/reflection (FT/FR) spectrum of the proposed structure (given in Fig. 1(a)) obtained for different substrates and corresponding refractive indices (CaF_2 (~1.42) < SiO_2 (~1.44) < BaF_2 (~1.46) < Al_2O_3 (~1.74)). The structure is illuminated by an x-polarized uniform plane wave propagating along the −z directions. (b) Calculated forward transmission spectrum and (c) forward reflection spectrum of the proposed structure obtained for different superstrates (different refractive indices from 1.9 to 2.15).

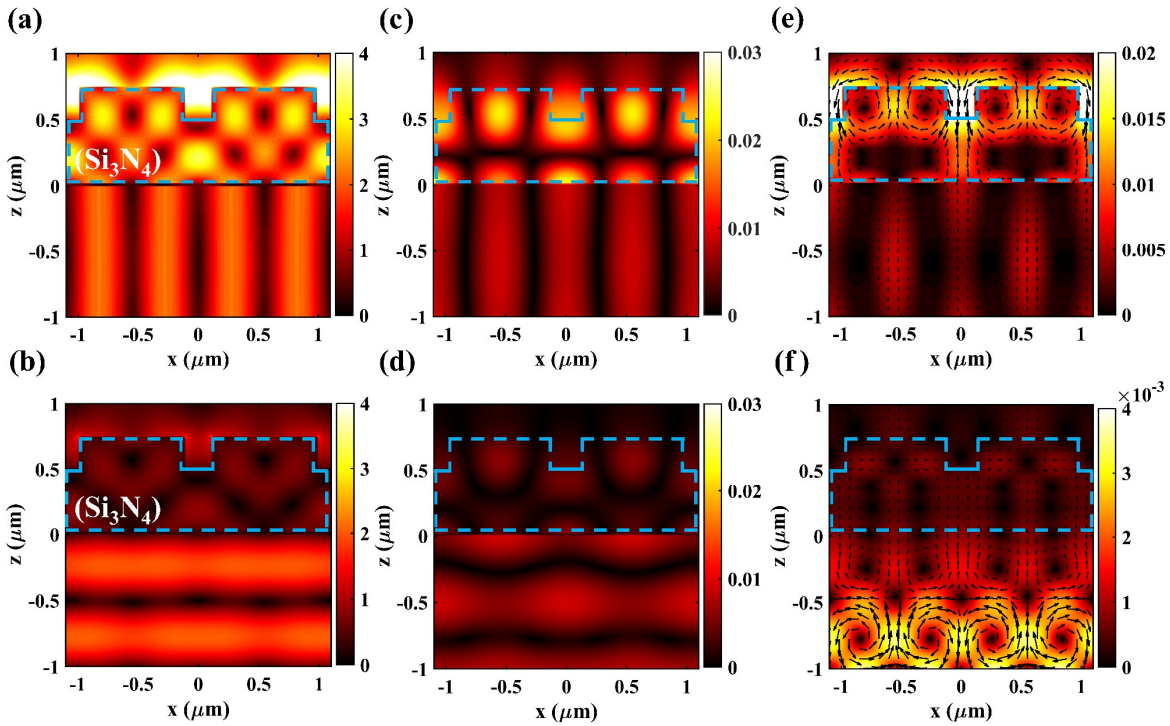

Figure 5.3. The absolute values of the total electric-field distributions on the x – z plane obtained for a two-unit cell at the operating wavelength of 1549 nm (peak resonance of forward transmission spectrum) when the object is normally illuminated by an x-polarized uniform plane wave from the (a) front side (forward illumination) and (b) back side (backward illumination). The absolute values of the total magnetic-field distributions when the structure experiences (c) forward and (d) backward illuminations at the same operating wavelength. The Poynting-vector distributions when the object experiences (e) forward and (f) backward illuminations. In all figures, dashed blue lines represent the Si_3N_4 area.

magnetic-field distributions for both forward and backward illuminations, are shown in Fig. 5.4(a) through Fig. 5.4(d) for a better visualization of the type of the second dip resonance (1624 nm, pertaining to the reflection spectrum of the forward illumination). The excitation of LRSPPs under the forward illumination at the bottom interface of the Ag layer is readily observed from the electric-field and magnetic-field distributions as seen in Fig. 5.4(a) and Fig. 5.4(c), respectively. The Poynting-vector distribution, shown in Fig. 5.4(e) for the forward illumination at the resonance wavelength of 1624 nm, confirms that LRSPPs do not contribute to the radiation in the next environment and are the main reason

for the absorption in the metallic layer. In a similar fashion to the operating wavelength of 1549 nm, the structure offers strong reflection by the Ag film under backward

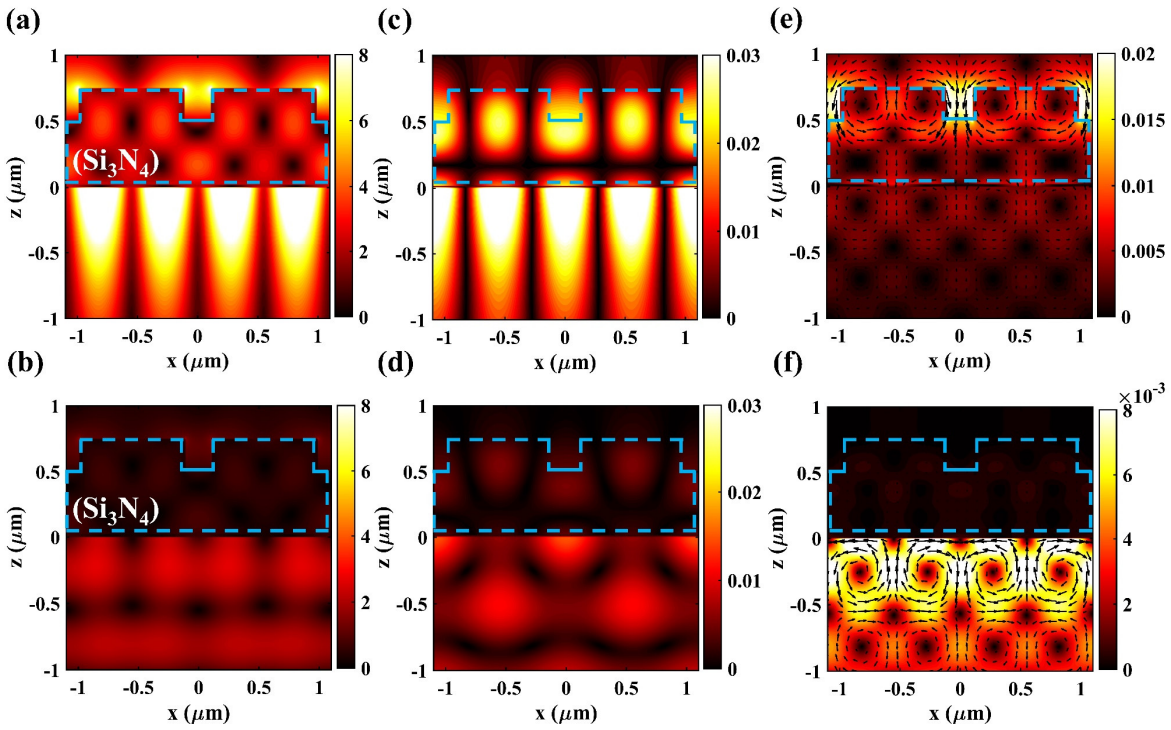

Figure 5.4. The absolute values of the total electric-field distributions on the x − z plane obtained for a two-unit cell at the operating wavelength of 1624 nm (second dip resonance of forward reflection spectrum) when the object is normally illuminated by an x-polarized uniform plane wave from the (a) front side (forward illumination) and (b) back side (backward illumination). The absolute values of the total magnetic-field distributions when the structure experiences (c) forward and (d) backward illuminations at the same operating wavelength. The Poynting-vector distributions when the object experiences (e) forward and (f) backward illuminations. In all figures, dashed blue lines represent the Si_3N_4 area.

incidence as shown in Fig. 5.4(b), Fig. 5.4(d), and Fig. 5.4(f), corresponding to the electric-field, magnetic-field, and Poynting-vector distributions, respectively. This is due to the fact that the configuration cannot support the excitation of SPPs and the plasmon tunneling from the back side.

5.2.4. Absorbed power density

For further investigation, the absolute values of absorbed power densities on the $x - z$ plane and in the vicinity of the Ag layer for both-illumination sides are considered at the resonance wavelengths of the reflection spectrum and shown in Fig. 5.5. The absorbed power density obtained at the resonance wavelength of 1549 nm for the forward

illumination is given in Fig. 5.5(a). It is seen that the transparency of the structure is due to the SPs excited on the top interface of the Ag layer. These SPs are attributed to the dispersion relation given in (4a), so the dominant excitation mode is SRSPP as demonstrated using different superstrate materials (see Fig. 5.2) and the field distributions (see Fig. 3). Regarding the absorbed power density at the second resonance (1624 nm), as shown in Fig. 5.5(b), the SPs excited in the bottom layer are the dominant ones and cause the second reflection dip in the reflection spectrum under forward incidence. Therefore, the great part of the absorption of the structure is due to the SPs excited on the bottom interface of the silver layer. These SPs are related to the dispersion given in (4b), so the excitation mode is LRSPP as demonstrated using different substrate materials (see Fig. 5.2) and the field distributions (see Fig. 5.4). According to Fig. 5.5(c) and Fig. 5.5(d) for the backward illumination at the operating wavelengths of 1549 nm and 1624 nm, respectively, it is observed that small amounts of the electromagnetic wave can be absorbed within the Ag layer due to the penetration of the electromagnetic wave, while these quantities are considerably smaller in comparison to their counterparts obtained from the forward illumination, demonstrating that most of the incident electromagnetic wave reflects.

5.2.5. Geometric parameters effects

It is also possible to provide an efficient optical-diode behavior in the desired operating wavelengths by using different values of the geometric parameters. As a result, the impact of different geometries on the resonance features of each of these modes have been studied as shown in Fig. 5.6 and Fig. 5.7. Under forward incidence, the SRSPPs excited by the dielectric diffraction grating at the upper interface can tunnel through the Ag film, when the thickness of the metallic layer is smaller than the penetration depth of the SRSPPs [231], [241], [242]. Therefore, the thickness of the Ag layer plays an important role in the efficient tunneling of the SRSPPs based on their penetration depth [231], [252]. The simulated forward and backward transmission power versus the wavelengths are presented in Fig. 5.6(a) and Fig. 5.6(b), respectively, for different thicknesses of the Ag layer (t_m: 5– 60 nm) when the other dimensional parameters are being kept fixed at their initial

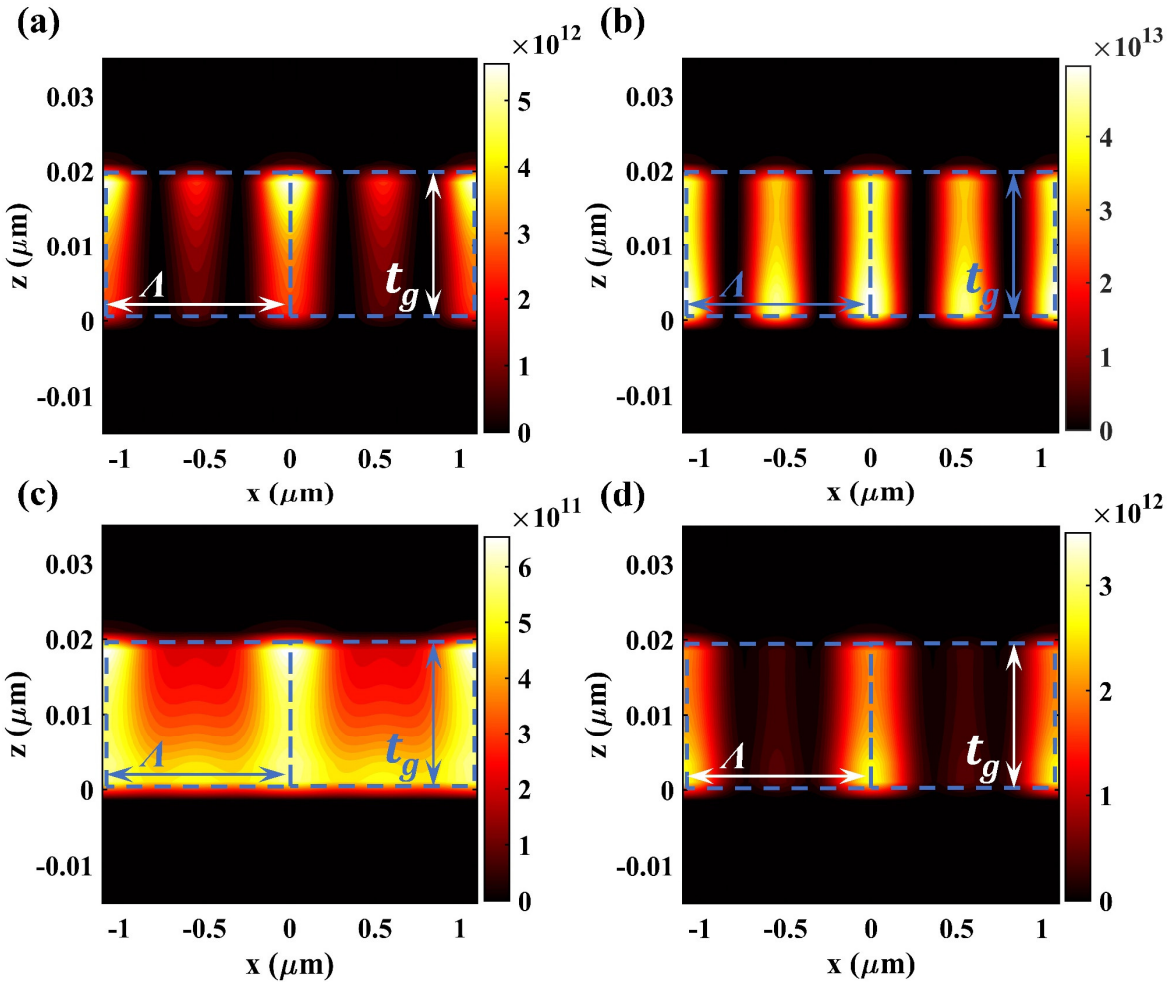

Figure 5.5. Absolute values of absorbed power densities obtained for a two-unit cell at the resonance wavelengths of (a) 1549 nm and (b) 1624 nm when the proposed AT structure is illuminated by an x-polarized uniform plane wave from the front side. Absolute values of absorbed power densities obtained for a two-unit cell at the resonance wavelengths of (c) 1549 nm and (d) 1624 nm when the proposed AT structure is illuminated by an x-polarized uniform plane wave from the back side. In all figures, dashed blue lines represent the Ag area.

(optimal) values. As expected, it is observed that the AT property of the proposed structure is strongly dependent on the thickness of the metallic layer. Under forward incidence (see Fig. 5.6(a)), it promotes the efficient tunneling of SPPs, and thereby helps to increase forward transmission. While under backward incidence (see Fig. 5.6(b)), it enhances reflection and thereby reduces transmission. Therefore, it is critical to choose suitable thickness for the Ag film. The thick Ag layer mitigates mixed mode SPP excitations and leads to

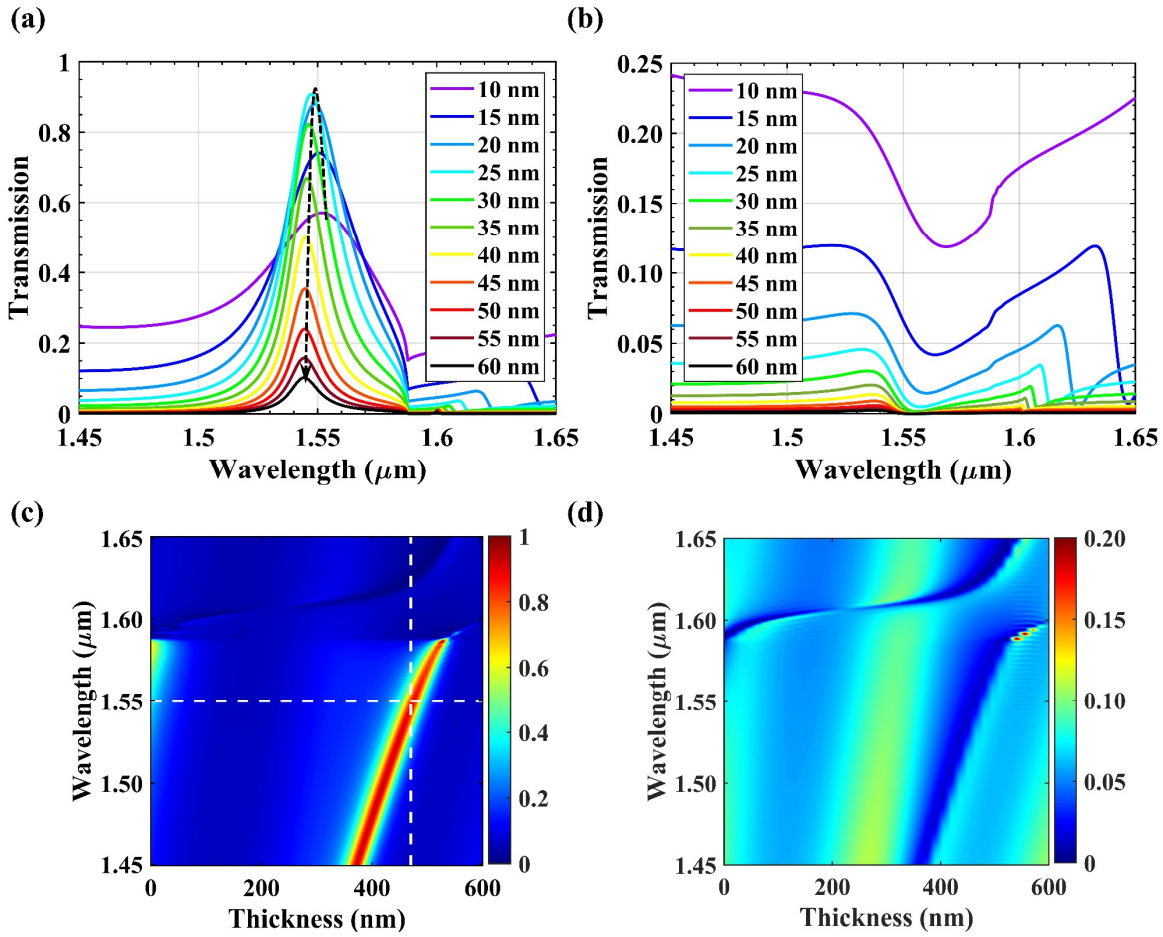

Figure 5.6. Dependency of the forward (first column) and backward (second column) transmission spectra of the proposed optical diode on the variation of geometry parameters including: (a)-(b) the thickness of the metal layer [10 nm $\leq t_m \leq$ 60 nm when $t_g =$ 260 nm, $w_g =$ 880 nm, $t_d =$ 470 nm and $\Lambda =$ 1100 nm], (c)-(d) the thickness of the dielectric slab [$0 < t_d <$ 600 nm when $t_g =$ 260 nm, $w_g =$ 880 nm, $t_m =$ 20 nm and $\Lambda =$ 1100 nm]. The interaction point of the white dashed lines corresponds to the operating wavelengths of 1549 nm.

unidirectional transmission blockage. However, at the optimal values of between 20 nm and 25 nm, the design has high on-resonance forward transmission with a near zero off- resonance backward response. On the other hand, when the Ag film is thinner ($t_m =$ 15 nm and 10 nm), the strong near-field coupling will change the excitation condition of SPPs, and then accordingly change the corresponding SPPs wavelength, resulting in a decrease in the forward transmittance at the operating wavelength. Another prominent geometry parameter is the thickness of the slab waveguide. This parameter can be utilized to tune the SPP resonances and improve the overall performance of the proposed structure

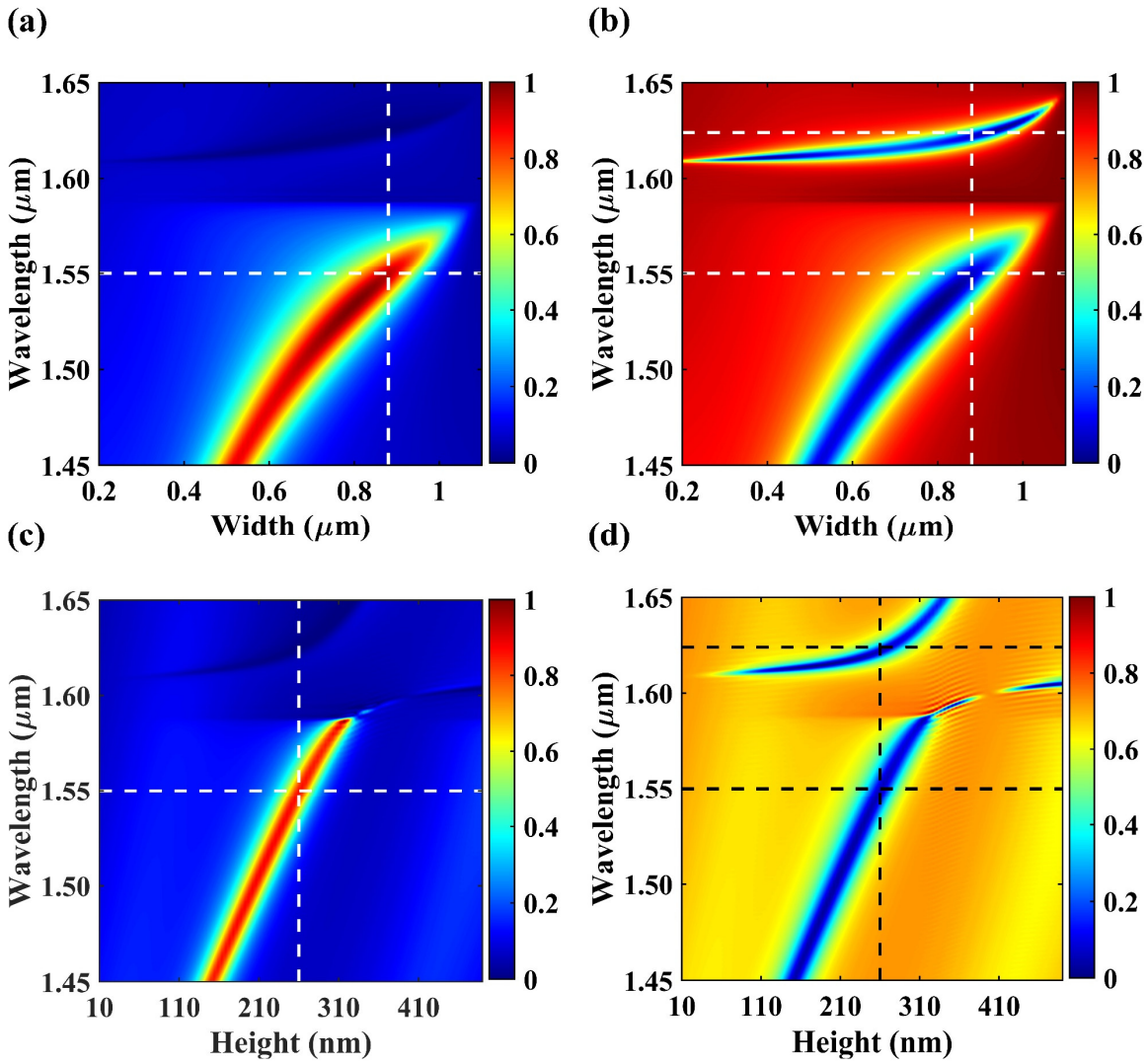

Figure 5.3. Dependency of the normalized transmission (first column) and reflection (second column) spectra of the proposed structure on the variation of geometry parameters including: (a)-(b) the width of grating [200 nm ≤ w_g ≤ 1100 nm when t_g = 260 nm, t_m = 20 nm, t_d = 470 nm and Λ = 1100 nm], and (c)-(d) the height (thickness) of the grating [10 nm ≤ t_g ≤ 490 nm when t_d = 470 nm, w_g = 880 nm, t_m = 20 nm and Λ = 1100 nm]. The interaction points of the dashed lines correspond to the operating wavelengths of 1549 nm and 1624 nm.

as seen in Fig. 5.6(c) and Fig. 5.6(d) representing forward and backward transmissions, respectively. Using this geometry, the resonance wavelength and its strength can be deliberately engineered. As seen in these figures, without this tuner slab, the resonance property (amplitude and FWHM) of the design is quite poor. The SPPs can be efficiently excited when the phase of the diffracted waves in the dielectric slab matches the phase of the surface plasmon waves in the silver film. Therefore, this layer adds a degree of

freedom to provide a better matching condition and stronger resonance response. The coupling efficiency of the proposed structure is also strongly dependent on the periodicity, height, and width of the grating as a fact that the normal incident wave first interacts with the grating and the grating determines the property of the diffracted waves. Therefore, the changes in the grating size seriously affect the performance of the structure and the excitation of SPPs. Fig. 5.7 illustrates the effects of the grating width and the grating height with respect to the wavelengths for both forward transmission and forward reflection cases. It is clear that, as the dimensions of the grating increase, at the specific width and height of the grating, the guided-mode resonance and the phase-matched conditions are satisfied, and the AT property is achieved. In addition, the spectral positions of the SPP modes vary and experience a red-shifted phenomenon in a linear fashion due to the occurring the Fabry–Pérot cavity modes and then corresponding SPP modes at longer wavelengths (provides phase-matching condition for another wavelength). As seen in Fig. 5.7(a) and Fig. 5.7(b), the most important part is that SPP cannot be excited when the width of grating structure is equal to 1.1 (the filling factor is 1), while increasing the height of the grating part decreases the effects of diffracted waves involved in the excitation of the SPPs as seen in Fig. 5.7(c) and Fig. 5.7(d). All in all, the first resonance is affected more by changing the grating dimensions due to the occurring SRSPP between the Ag layer and the waveguide slab in comparison to the second resonance (LRSPP) occurs at the bottom layer.

CHAPTER 6

Conclusion

This thesis presented and discussed four important applications of plasmonic metamaterial based structures, namely, 1) Hybrid indium tin oxide-Au metamaterial absorber in the visible and near-infrared ranges for selective thermal emissions and sensors. 2) Active tuning from narrowband to broadband absorbers using a sub-wavelength VO_2 for optical modulator. 3) A spectrally selective nanoantenna emitter compatible with multiple thermal infrared applications. 4) Diode like high-contrast asymmetric transmission of linearly polarized waves.

In Chapter 2, we have proposed a novel hybrid metastructure that functions as a narrowband MPA at two wavelength is the visible ($733\ nm$) and NIR ($900\ nm$) ranges, and operates as a broadband absorber in a wide range of wavelengths in another window in the NIR region (from $1{,}530\ nm$ to $2{,}700\ nm$ with the bandwidth of $1{,}170\ nm$). The metamaterial is composed of an array of self-aligned hybrid ITO-Au SRRs that are separated from an optically thick bottom reflector with a SiO_2 spacer layer. ITO behaves as a low-loss dielectric material in the visible range and a lossy plasmonic material at wavelengths larger than $1{,}420\ nm$. Consequently, it is found out that the narrowband response of the metamaterial is originated from the low-loss plasmonic response of Au SRRs and the broadband absorptive characteristic is achieved owing to the lossy plasmonic feature of ITO. As mentioned earlier, since feasible parameters have been

considered in optimizing the suggested design, it is possible to experimentally verify the numerical results reported in this study. More investigations revealed that the designed MPA represents polarization-independent and omnidirectional absorption characteristics for oblique incidences up to 50º. The proposal MPA can find potential applications in sensors, thermophotovoltaic devices and thermal emitters.

In our second work, we proposed MPA with diverse functionalities enabled by inserting of a thin VO_2 layer into the plasmonic a-Si nanograting resonator in the NIR region. Double narrowband perfect absorptions are achieved under the insulator VO_2 state. Upon phase transformation from insulator to metallic, the proposed design undergoes from double to triple spectrally adjacent perfect absorptions that results in a broadband light absorption. Our numerical analysis demonstrates that the first resonance peak experiences a blue shift because of changing in the phase of the reflected incident waves. The second resonance is due to the formation of a virtual MIM configuration and finally the third mode is red-shifted because of increasing in the effective refractive index of the nanograting. In addition to the mode profiles, the impedance matching theory is used as the common method to physically analyze the EM waves of the structure at the resonances. In the last part of the paper, the linearly thermal tunability of Si is studied. It is shown that, owing to the strong light confinement in the ultrasmall gaps of the structure, a thermal tuning is achieved within the Si nanograting, which is sufficient enough to design multi-resonance tunable features to cover a broad range spectrum. Therefore, the proposed hybrid design can provide multi-resonances tunable features for designing linearly thermal-tunable and broadband MPAs. Apart from the traditional applications, such as optical switches and filters, this design shows great prospects in the development of novel optical modulators and infrared (IR) camouflages.

In Chapter 4, we proposed a GSP-based wavelength-selective nanoantenna emitter (design I) suitable for multiple thermal camouflage scenarios. Triple narrowband perfect absorptions are achieved at the resonance wavelengths of 1524 nm, 2279 nm, and 6000 nm, whose absorption peaks perfectly match the atmospheric absorption spectrum. The proposed nanoantenna emitter is designed to have low emissivity within atmospheric windows and its performance is validated using numerical and analytical methods. Later, we proposed a multilayer grating structure as an extension of design I to cover solar

thermal application besides multiple thermal camouflage scenarios. Design II contains a nearly perfect absorption ranging from 929 nm to 1472 nm and a narrowband absorption at the resonance wavelength of 5750 nm, where the later absorption resonance is tuned and modified by adding graphene layers. Furthermore, we have also demonstrated that the multi-layer graphene structure could outperform the single-layer one in terms of shifting the MIR resonance wavelength and reducing the absorption peak of the fourth response. Finally, the performances of the selective nanoantenna emitters in thermal camouflage applications are validated by calculating the spectral radiant emittances. It is shown that the infrared signatures of design I and design II (without/with graphene layers) are significantly reduced compared to the blackbody radiation energy for the entire wavelength spectrum at least by 96% and 91%, respectively, ranging from the room temperature to 500 K.

In our fourth and final work, we proposed a simple periodic nano array design with AT property which can be considered as an optical diode. The proposed device is made up of a grating waveguide on a thin metal layer coated on a substrate, and it works based on the excitations of SPPs at both interfaces of the thin metal layer and plasmon-tunneling effect. The plasmon-tunneling effect is based on the transmission provided by the SRSPP excited at the upper interface. In contrast to the other works, the proposed design has a high-contrast asymmetric light transmission ratio in the NIR and provide near-zero inverse transmission. The blocking is caused by the metal layer where the SPP cannot be excited. The spectral behaviors of the proposed design are analyzed and validated by using RCWA besides the FDTD method in order to prove the proposed concept. Furthermore, the emerging nanofabrication techniques will allow the fabrication of our design where the operating principle is not limited to the NIR region, and it can be extended to a different range of the spectrum due to the scalable property and flexible design of the proposed structure.

Bibliography

[1] A. J. Bard, *Fundamentals and Applications Plasmonics : Fundamentals and Applications*, vol. 677, no. 1. 2004.

[2] H. Müller, "Optical Properties of Metal Clusters," *Zeitschrift für Physikalische Chemie*, vol. 194, no. 2, 1996, doi: 10.1524/zpch.1996.194.part_2.278.

[3] P. G. Kik and M. L. Brongersma, "Surface plasmon nanophotonics," *Springer Series in Optical Sciences*, vol. 131, 2007, doi: 10.1007/978-1-4020-4333-8_1.

[4] Y. Chen and H. Ming, "Review of surface plasmon resonance and localized surface plasmon resonance sensor?," *Photonic Sensors*, vol. 2, no. 1. 2012. doi: 10.1007/s13320-011-0051-2.

[5] A. Serrano, O. R. de La Fuente, and M. A. García, "Extended and localized surface plasmons in annealed Au films on glass substrates," *Journal of Applied Physics*, vol. 108, no. 7, 2010, doi: 10.1063/1.3485825.

[6] "VII. Colours in metal glasses, in metallic films, and in metallic solutions.—II," *Philosophical Transactions of the Royal Society of London. Series A, Containing Papers of a Mathematical or Physical Character*, vol. 205, no. 387–401, 1906, doi: 10.1098/rsta.1906.0007.

[7] G. Mie, "Beiträge zur Optik trüber Medien, speziell kolloidaler Metallösungen," *Annalen der Physik*, vol. 330, no. 3, 1908, doi: 10.1002/andp.19083300302.

[8] S. Eustis and M. A. El-Sayed, "Determination of the aspect ratio statistical distribution of gold nanorods in solution from a theoretical fit of the observed inhomogeneously broadened longitudinal plasmon resonance absorption spectrum," *Journal of Applied Physics*, vol. 100, no. 4, 2006, doi: 10.1063/1.2244520.

[9] H. Devoe, "Optical properties of molecular aggregates. I. Classical model of electronic absorption and refraction," *The Journal of Chemical Physics*, vol. 41, no. 2, 1964, doi: 10.1063/1.1725879.

[10] R. W. Wood, "On a remarkable case of uneven distribution of light in a diffraction grating spectrum," *Proceedings of the Physical Society of London*, vol. 18, no. 1, 1901, doi: 10.1088/1478-7814/18/1/325.

[11] U. Fano, “The Theory of Anomalous Diffraction Gratings and of Quasi-Stationary Waves on Metallic Surfaces (Sommerfeld’s Waves),” *Journal of the Optical Society of America*, vol. 31, no. 3, 1941, doi: 10.1364/josa.31.000213.

[12] D. Pines, “Collective energy losses in solids,” *Reviews of Modern Physics*, vol. 28, no. 3, 1956, doi: 10.1103/RevModPhys.28.184.

[13] C. J. Powell and J. B. Swan, “Origin of the characteristic electron energy losses in magnesium,” *Physical Review*, vol. 116, no. 1, 1959, doi: 10.1103/PhysRev.116.81.

[14] R. H. Ritchie, E. T. Arakawa, J. J. Cowan, and R. N. Hamm, “Surface-plasmon resonance effect in grating diffraction,” *Physical Review Letters*, vol. 21, no. 22, 1968, doi: 10.1103/PhysRevLett.21.1530.

[15] E. Kretschmann, “Die Bestimmung optischer Konstanten von Metallen durch Anregung von Oberflächenplasmaschwingungen,” *Zeitschrift für Physik*, vol. 241, no. 4, 1971, doi: 10.1007/BF01395428.

[16] E. Kretschmann and H. Raether, “Radiative Decay of Non Radiative Surface Plasmons Excited by Light,” *Zeitschrift fur Naturforschung - Section A Journal of Physical Sciences*, vol. 23, no. 12. 1968. doi: 10.1515/zna-1968-1247.

[17] A. Otto, “Excitation of nonradiative surface plasma waves in silver by the method of frustrated total reflection,” *Zeitschrift für Physik*, vol. 216, no. 4, 1968, doi: 10.1007/BF01391532.

[18] U. Kreibig and P. Zacharias, “Surface plasma resonances in small spherical silver and gold particles,” *Zeitschrift für Physik*, vol. 231, no. 2, 1970, doi: 10.1007/BF01392504.

[19] M. Fleischmann, P. J. Hendra, and A. J. McQuillan, “Raman spectra of pyridine adsorbed at a silver electrode,” *Chemical Physics Letters*, vol. 26, no. 2, 1974, doi: 10.1016/0009-2614(74)85388-1.

[20] S. L. Cunningham, A. A. Maradudin, and R. F. Wallis, “Effect of a charge layer on the surface-plasmon-polariton dispersion curve,” *Physical Review B*, vol. 10, no. 8, 1974, doi: 10.1103/PhysRevB.10.3342.

[21] C. Kittel, “Introduction to Solid State Physics, 8th edition,” *Wiley & Sons, New York, NY*, 2004.

[22] C. Noguez, “Surface plasmons on metal nanoparticles: The influence of shape and physical environment,” *Journal of Physical Chemistry C*, vol. 111, no. 10, 2007, doi: 10.1021/jp066539m.

[23] M. A. Garcia, “Surface plasmons in metallic nanoparticles: Fundamentals and applications,” *Journal of Physics D: Applied Physics*, vol. 44, no. 28. 2011. doi:

10.1088/0022-3727/44/28/283001.

[24] M. Quinten and U. Kreibig, “Absorption and elastic scattering of light by particle aggregates,” *Applied Optics*, vol. 32, no. 30, 1993, doi: 10.1364/ao.32.006173.

[25] M. A. García, J. Llopis, and S. E. Paje, “A simple model for evaluating the optical absorption spectrum from small Au-colloids in sol-gel films,” *Chemical Physics Letters*, vol. 315, no. 5–6, 1999, doi: 10.1016/S0009-2614(99)01206-3.

[26] F. J. Garcia-Vidal, L. Martín-Moreno, and J. B. Pendry, “Surfaces with holes in them: New plasmonic metamaterials,” *Journal of Optics A: Pure and Applied Optics*, vol. 7, no. 2, 2005, doi: 10.1088/1464-4258/7/2/013.

[27] *Handbook of Surface Plasmon Resonance*. 2008. doi: 10.1039/9781847558220.

[28] Z. Han and S. I. Bozhevolnyi, “Radiation guiding with surface plasmon polaritons,” *Reports on Progress in Physics*, vol. 76, no. 1, 2013, doi: 10.1088/0034-4885/76/1/016402.

[29] L. Li, “Experimental Basics of Surface Plasmon Polaritons,” 2017. doi: 10.1007/978-981-10-4663-6_2.

[30] S. A. Maier, P. E. Barclay, T. J. Johnson, M. D. Friedman, and O. Painter, “Low-loss fiber accessible plasmon waveguide for planar energy guiding and sensing,” *Applied Physics Letters*, vol. 84, no. 20, 2004, doi: 10.1063/1.1753060.

[31] B. Hecht, H. Bielefeldt, L. Novotny, Y. Inouye, and D. W. Pohl, “Local excitation, scattering, and interference of surface plasmons,” *Physical Review Letters*, vol. 77, no. 9, 1996, doi: 10.1103/PhysRevLett.77.1889.

[32] D. Sarid, “Long-Range Surface-Plasma Waves on Very Thin Metal Films,” *Physical Review Letters*, vol. 47, no. 26, 1981, doi: 10.1103/PhysRevLett.47.1927.

[33] A. P. Hibbins, “GRATING COUPLING OF SURFACE PLASMON POLARITONS AT VISIBLE AND MICROWAVE FREQUENCIES,” 1999.

[34] W. Li, Z. Li, J. He, and L. Chu, “Design and performance of a composite grating-coupled surface plasmon resonance trace liquid concentration sensor,” *Sensors (Switzerland)*, vol. 19, no. 24, 2019, doi: 10.3390/s19245502.

[35] P. Matheu, S. H. Lim, D. Derkacs, C. McPheeters, and E. T. Yu, “Metal and dielectric nanoparticle scattering for improved optical absorption in photovoltaic devices,” *Applied Physics Letters*, vol. 93, no. 11, 2008, doi: 10.1063/1.2957980.

[36] S. Pillai, K. R. Catchpole, T. Trupke, and M. A. Green, “Surface plasmon enhanced silicon solar cells,” in *Journal of Applied Physics*, 2007, vol. 101, no. 9. doi: 10.1063/1.2734885.

[37] V. M. Shalaev and S. Kawata, *Nanophotonics with Surface Plasmons*. 2007. doi: 10.1016/B978-0-444-52838-4.X5000-0.

[38] R. Gordon, “Surface Plasmon Nanophotonics: A Tutorial,” *IEEE Nanotechnology Magazine*, vol. 2, no. 3, 2008, doi: 10.1109/MNANO.2008.931481.

[39] Y. Zhao, S. Gan, L. Wu, J. Zhu, Y. Xiang, and X. Dai, “GeSe nanosheets modified surface plasmon resonance sensors for enhancing sensitivity,” *Nanophotonics*, vol. 9, no. 2, 2020, doi: 10.1515/nanoph-2019-0170.

[40] S. Singh *et al.*, “2D nanomaterial-based surface plasmon resonance sensors for biosensing applications,” *Micromachines*, vol. 11, no. 8. 2020. doi: 10.3390/mi11080779.

[41] R. D. Harris and J. S. Wilkinson, “Waveguide surface plasmon resonance sensors,” *Sensors and Actuators: B. Chemical*, vol. 29, no. 1–3, 1995, doi: 10.1016/0925-4005(95)01692-9.

[42] M. M. Miller and A. A. Lazarides, “Sensitivity of metal nanoparticle surface plasmon resonance to the dielectric environment,” *Journal of Physical Chemistry B*, vol. 109, no. 46, 2005, doi: 10.1021/jp054227y.

[43] J. Ibrahim *et al.*, “Surface plasmon resonance based temperature sensors in liquid environment,” *Sensors (Switzerland)*, vol. 19, no. 15, 2019, doi: 10.3390/s19153354.

[44] B. D. Gupta and R. K. Verma, “Surface plasmon resonance-based fiber optic sensors: Principle, probe designs, and some applications,” *Journal of Sensors*, vol. 2009, 2009, doi: 10.1155/2009/979761.

[45] M. E. Leunissen *et al.*, “Ionic colloidal crystals of oppositely charged particles,” *Nature*, vol. 437, no. 7056, 2005, doi: 10.1038/nature03946.

[46] J. B. Pendry, “Time reversal and negative refraction,” *Science*, vol. 322, no. 5898, 2008, doi: 10.1126/science.1162087.

[47] H. Harutyunyan, R. Beams, and L. Novotny, “Controllable optical negative refraction and phase conjugation in graphite thin films,” *Nature Physics*, vol. 9, no. 7, 2013, doi: 10.1038/nphys2618.

[48] S. Palomba, S. Zhang, Y. Park, G. Bartal, X. Yin, and X. Zhang, “Optical negative refraction by four-wave mixing in thin metallic nanostructures,” *Nature Materials*, vol. 11, no. 1, 2012, doi: 10.1038/nmat3148.

[49] A. R. Katko, S. Gu, J. P. Barrett, B. I. Popa, G. Shvets, and S. A. Cummer, “Phase conjugation and negative refraction using nonlinear active metamaterials,” *Physical Review Letters*, vol. 105, no. 12, 2010, doi: 10.1103/PhysRevLett.105.123905.

[50] M. Lapine, I. v. Shadrivov, D. A. Powell, and Y. S. Kivshar, “Magnetoelastic metamaterials,” *Nature Materials*, vol. 11, no. 1, 2012, doi: 10.1038/nmat3168.

[51] A. v. Krasavin, T. P. Vo, W. Dickson, P. M. Bolger, and A. v. Zayats, “All-plasmonic modulation via stimulated emission of copropagating surface plasmon polaritons on a

substrate with gain," *Nano Letters*, vol. 11, no. 6, 2011, doi: 10.1021/nl200255t.

[52] G. A. Wurtz *et al.*, "Designed ultrafast optical nonlinearity in a plasmonic nanorod metamaterial enhanced by nonlocality," *Nature Nanotechnology*, vol. 6, no. 2, 2011, doi: 10.1038/nnano.2010.278.

[53] Z. Jacob, J. Y. Kim, G. v. Naik, A. Boltasseva, E. E. Narimanov, and V. M. Shalaev, "Engineering photonic density of states using metamaterials," *Applied Physics B: Lasers and Optics*, vol. 100, no. 1, 2010, doi: 10.1007/s00340-010-4096-5.

[54] D. E. Chang, A. S. Sørensen, E. A. Demler, and M. D. Lukin, "A single-photon transistor using nanoscale surface plasmons," *Nature Physics*, vol. 3, no. 11, 2007, doi: 10.1038/nphys708.

[55] A. v. Akimov *et al.*, "Generation of single optical plasmons in metallic nanowires coupled to quantum dots," *Nature*, vol. 450, no. 7168, 2007, doi: 10.1038/nature06230.

[56] M. A. Noginov *et al.*, "Demonstration of a spaser-based nanolaser," *Nature*, vol. 460, no. 7259, 2009, doi: 10.1038/nature08318.

[57] S. H. Lee, J. Choi, H. D. Kim, H. Choi, and B. Min, "Ultrafast refractive index control of a terahertz graphene metamaterial," *Scientific Reports*, vol. 3, 2013, doi: 10.1038/srep02135.

[58] H. Lin *et al.*, "A 90-nm-thick graphene metamaterial for strong and extremely broadband absorption of unpolarized light," *Nature Photonics*, vol. 13, no. 4, 2019, doi: 10.1038/s41566-019-0389-3.

[59] S. R. L. da Cunha and J. L. B. de Aguiar, "Phase change materials and energy efficiency of buildings: A review of knowledge," *Journal of Energy Storage*, vol. 27. 2020. doi: 10.1016/j.est.2019.101083.

[60] S. Abdollahramezani *et al.*, "Tunable nanophotonics enabled by chalcogenide phase-change materials," *Nanophotonics*, 2020, doi: 10.1515/nanoph-2020-0039.

[61] Q. Liu, Y. Cui, D. Gardner, X. Li, S. He, and I. I. Smalyukh, "Self-alignment of plasmonic gold nanorods in reconfigurable anisotropic fluids for tunable bulk metamaterial applications," *Nano Letters*, vol. 10, no. 4, 2010, doi: 10.1021/nl9042104.

[62] I. C. Khoo, D. H. Werner, X. Liang, A. Diaz, and B. Weiner, "Nanosphere dispersed liquid crystals for tunable negative-zero-positive index of refraction in the optical and terahertz regimes," *Optics Letters*, vol. 31, no. 17, 2006, doi: 10.1364/ol.31.002592.

[63] C. Zhao, Y. Liu, Y. Zhao, N. Fang, and T. J. Huang, "A reconfigurable plasmofluidic lens," *Nature Communications*, vol. 4, 2013, doi: 10.1038/ncomms3305.

[64] S. Tretyakov, A. Urbas, and N. Zheludev, "The century of metamaterials," *Journal of*

Optics (United Kingdom), vol. 19, no. 8. 2017. doi: 10.1088/2040-8986/aa77a8.

[65] A. Boardman, "Pioneers in metamaterials: John Pendry and Victor Veselago," *Journal of Optics*, vol. 13, no. 2. 2011. doi: 10.1088/2040-8978/13/2/020401.

[66] J. Valentine, J. Li, T. Zentgraf, G. Bartal, and X. Zhang, "An optical cloak made of dielectrics," *Nature Materials*, vol. 8, no. 7, 2009, doi: 10.1038/nmat2461.

[67] Z. Li, M. Mutlu, and E. Ozbay, "Chiral metamaterials: From optical activity and negative refractive index to asymmetric transmission," *Journal of Optics (United Kingdom)*, vol. 15, no. 2. 2013. doi: 10.1088/2040-8978/15/2/023001.

[68] A. Fang, T. Koschny, and C. M. Soukoulis, "Lasing in metamaterial nanostructures," *Journal of Optics A: Pure and Applied Optics*, vol. 12, no. 2, 2010, doi: 10.1088/2040-8978/12/2/024013.

[69] A. J. Hoffman *et al.*, "Negative refraction in semiconductor metamaterials," *Nature Materials*, vol. 6, no. 12. 2007. doi: 10.1038/nmat2033.

[70] C. M. Watts, X. Liu, and W. J. Padilla, "Metamaterial electromagnetic wave absorbers," *Advanced Materials*, vol. 24, no. 23, 2012, doi: 10.1002/adma.201200674.

[71] N. I. Landy, S. Sajuyigbe, J. J. Mock, D. R. Smith, and W. J. Padilla, "Perfect metamaterial absorber," *Physical Review Letters*, vol. 100, no. 20, 2008, doi: 10.1103/PhysRevLett.100.207402.

[72] L. Shi *et al.*, "Ultra-narrow multi-band polarization-insensitive plasmonic perfect absorber for sensing," *Nanotechnology*, vol. 31, no. 46, 2020, doi: 10.1088/1361-6528/abad60.

[73] N. I. Landy, C. M. Bingham, T. Tyler, N. Jokerst, D. R. Smith, and W. J. Padilla, "Design, theory, and measurement of a polarization-insensitive absorber for terahertz imaging," *Physical Review B - Condensed Matter and Materials Physics*, vol. 79, no. 12, 2009, doi: 10.1103/PhysRevB.79.125104.

[74] S. Yokogawa, S. P. Burgos, and H. A. Atwater, "Plasmonic color filters for CMOS image sensor applications," *Nano Letters*, vol. 12, no. 8, 2012, doi: 10.1021/nl302110z.

[75] W. Li and J. Valentine, "Metamaterial perfect absorber based hot electron photodetection," *Nano Letters*, vol. 14, no. 6, 2014, doi: 10.1021/nl501090w.

[76] Y. Liu, Y. Chen, J. Li, T. chen Hung, and J. Li, "Study of energy absorption on solar cell using metamaterials," *Solar Energy*, vol. 86, no. 5, 2012, doi: 10.1016/j.solener.2012.02.021.

[77] T. Liu and J. Takahara, "Ultrabroadband absorber based on single-sized embedded metal-dielectric-metal structures and application of radiative cooling," *Optics Express*, vol. 25, no. 12, 2017, doi: 10.1364/oe.25.00a612.

[78] T. G. U. Ghobadi, A. Ghobadi, E. Ozbay, and F. Karadas, “Strategies for Plasmonic Hot-Electron-Driven Photoelectrochemical Water Splitting,” *ChemPhotoChem*, vol. 2, no. 3. 2018. doi: 10.1002/cptc.201700165.

[79] A. Ghobadi *et al.*, “Visible light nearly perfect absorber: an optimum unit cell arrangement for near absolute polarization insensitivity,” *Optics Express*, vol. 25, no. 22, 2017, doi: 10.1364/oe.25.027624.

[80] C.-H. Lin, R.-L. Chern, and H.-Y. Lin, “Polarization-independent broad-band nearly perfect absorbers in the visible regime,” *Optics Express*, vol. 19, no. 2, 2011, doi: 10.1364/oe.19.000415.

[81] Y. Zhu, T. Lan, P. Liu, and J. Yang, “ Broadband near-infrared TiO 2 dielectric metamaterial absorbers ,” *Applied Optics*, vol. 58, no. 26, 2019, doi: 10.1364/ao.58.007134.

[82] A. Kalantari Osgouei, H. Hajian, B. Khalichi, A. E. Serebryannikov, A. Ghobadi, and E. Ozbay, “Active Tuning from Narrowband to Broadband Absorbers Using a Sub-wavelength VO2 Embedded Layer,” *Plasmonics*, 2021, doi: 10.1007/s11468-020-01370-w.

[83] B. Deng *et al.*, “Coupling-Enhanced Broadband Mid-infrared Light Absorption in Graphene Plasmonic Nanostructures,” *ACS Nano*, vol. 10, no. 12, 2016, doi: 10.1021/acsnano.6b06203.

[84] K. Zhang, R. Deng, L. Song, and T. Zhang, “Broadband near-infrared absorber based on all metallic metasurface,” *Materials*, vol. 12, no. 21, 2019, doi: 10.3390/ma12213568.

[85] H. Liu, K. Luo, S. Tang, D. Peng, F. Hu, and L. Tu, “An ultra-wideband THz/IR metamaterial absorber based on doped silicon,” *Materials*, vol. 11, no. 12, 2018, doi: 10.3390/ma11122590.

[86] Y. Zhao, C. Yu, and W. Zhang, “Ultrabroadband Near-perfect Anisotropic Metamaterial Absorber Based on a Curved Periodic W/TPX Stack,” *Nanoscale and Microscale Thermophysical Engineering*, vol. 23, no. 1, 2019, doi: 10.1080/15567265.2019.1567633.

[87] H. Li, W. Xu, Q. Cui, Y. Wang, and J. Yu, “Theoretical design of a reconfigurable broadband integrated metamaterial terahertz device,” *Optics Express*, vol. 28, no. 26, 2020, doi: 10.1364/oe.414961.

[88] J. Li *et al.*, “Metal-graphene hybrid active chiral metasurfaces for dynamic terahertz wavefront modulation and near field imaging,” *Carbon*, vol. 163, 2020, doi: 10.1016/j.carbon.2020.03.019.

[89] Y. Huang *et al.*, “Catenary Electromagnetics for Ultra-Broadband Lightweight Absorbers

and Large-Scale Flat Antennas," *Advanced Science*, vol. 6, no. 7, 2019, doi: 10.1002/advs.201801691.

[90] H. Zhuang *et al.*, "Broadband microwave metamaterial absorber based on magnetic periodic elements," *Journal of Physics D: Applied Physics*, vol. 53, no. 25, 2020, doi: 10.1088/1361-6463/ab8138.

[91] T. T. Nguyen and S. Lim, "Design of Metamaterial Absorber using Eight-Resistive-Arm Cell for Simultaneous Broadband and Wide-Incidence-Angle Absorption," *Scientific Reports*, vol. 8, no. 1, 2018, doi: 10.1038/s41598-018-25074-8.

[92] H.-T. Chen, "Interference theory of metamaterial perfect absorbers," *Optics Express*, vol. 20, no. 7, 2012, doi: 10.1364/oe.20.007165.

[93] H. Hajian, A. Ghobadi, B. Butun, and E. Ozbay, "Active metamaterial nearly perfect light absorbers: a review [Invited]," *Journal of the Optical Society of America B*, vol. 36, no. 8, 2019, doi: 10.1364/josab.36.00f131.

[94] Z. Li, S. Butun, and K. Aydin, "Large-area, Lithography-free super absorbers and color filters at visible frequencies using ultrathin metallic films," *ACS Photonics*, vol. 2, no. 2, 2015, doi: 10.1021/ph500410u.

[95] Z. Yong, S. Zhang, C. Gong, and S. He, "Narrow band perfect absorber for maximum localized magnetic and electric field enhancement and sensing applications," *Scientific Reports*, vol. 6, 2016, doi: 10.1038/srep24063.

[96] F. Ding, J. Dai, Y. Chen, J. Zhu, Y. Jin, and S. I. Bozhevolnyi, "Broadband near-infrared metamaterial absorbers utilizing highly lossy metals," *Scientific Reports*, vol. 6, 2016, doi: 10.1038/srep39445.

[97] A. Ghobadi, H. Hajian, A. R. Rashed, B. Butun, and E. Ozbay, "Tuning the metal filling fraction in metal-insulator-metal ultra-broadband perfect absorbers to maximize the absorption bandwidth," *Photonics Research*, vol. 6, no. 3, 2018, doi: 10.1364/prj.6.000168.

[98] M. G. Nielsen, A. Pors, O. Albrektsen, and S. I. Bozhevolnyi, "Efficient absorption of visible radiation by gap plasmon resonators," *Optics Express*, vol. 20, no. 12, 2012, doi: 10.1364/oe.20.013311.

[99] B. Zhang *et al.*, "Polarization-independent dual-band infrared perfect absorber based on a metal-dielectric-metal elliptical nanodisk array," *Optics Express*, vol. 19, no. 16, 2011, doi: 10.1364/oe.19.015221.

[100] Z. H. Jiang, S. Yun, F. Toor, D. H. Werner, and T. S. Mayer, "Conformal dual-band near-perfectly absorbing mid-infrared metamaterial coating," *ACS Nano*, vol. 5, no. 6, 2011, doi: 10.1021/nn2004603.

[101] Y. Tang, J. A. Bossard, D. H. Werner, and T. S. Mayer, “Single-layer metallodielectric nanostructures as dual-band midinfrared filters,” *Applied Physics Letters*, vol. 92, no. 26, 2008, doi: 10.1063/1.2944137.

[102] H. Li and J. Yu, “Bifunctional terahertz absorber with a tunable and switchable property between broadband and dual-band,” *Optics Express*, vol. 28, no. 17, 2020, doi: 10.1364/oe.401992.

[103] H. Hajian, A. Ghobadi, B. Butun, and E. Ozbay, “Tunable, omnidirectional, and nearly perfect resonant absorptions by a graphene-hBN-based hole array metamaterial,” *Optics Express*, vol. 26, no. 13, 2018, doi: 10.1364/oe.26.016940.

[104] R. C. Thompson, “Optical Waves in Layered Media,” *Journal of Modern Optics*, vol. 37, no. 1, 1990, doi: 10.1080/09500349014550171.

[105] D. R. Smith, “Analytic expressions for the constitutive parameters of magnetoelectric metamaterials,” *Physical Review E - Statistical, Nonlinear, and Soft Matter Physics*, vol. 81, no. 3, 2010, doi: 10.1103/PhysRevE.81.036605.

[106] C. E. Kriegler, M. S. Rill, S. Linden, and M. Wegener, “Bianisotropic photonic metamaterials,” *IEEE Journal on Selected Topics in Quantum Electronics*, vol. 16, no. 2, 2010, doi: 10.1109/JSTQE.2009.2020809.

[107] D. R. Smith, D. C. Vier, T. Koschny, and C. M. Soukoulis, “Electromagnetic parameter retrieval from inhomogeneous metamaterials,” *Physical Review E - Statistical, Nonlinear, and Soft Matter Physics*, vol. 71, no. 3, 2005, doi: 10.1103/PhysRevE.71.036617.

[108] “Solutions, L. FDTD Solutions, Lumerical Solutions.” Vancouver, 2018.

[109] K. B. Alici, A. B. Turhan, C. M. Soukoulis, and E. Ozbay, “Optically thin composite resonant absorber at the near-infrared band: a polarization independent and spectrally broadband configuration,” *Optics Express*, vol. 19, no. 15, 2011, doi: 10.1364/oe.19.014260.

[110] S. Cakmakyapan, H. Caglayan, and E. Ozbay, “Coupling enhancement of split ring resonators on graphene,” *Carbon*, vol. 80, no. 1, 2014, doi: 10.1016/j.carbon.2014.08.073.

[111] Z. Zhu, P. Evans, R. Haglund, and J. Valentine, “Tunable phase-changing metasurface for near-infrared sensing and imaging,” in *Optics InfoBase Conference Papers*, 2017, vol. Part F55-NOMA 2017. doi: 10.1364/NOMA.2017.NoW3C.1.

[112] X. Luo, “Extraordinary Young’s Interferences and Super-Diffraction Laser Lithography,” in *Handbook of Laser Micro- and Nano-Engineering*, 2020. doi: 10.1007/978-3-319-69537-2_42-1.

[113] Y. Huang, L. Liu, M. Pu, X. Li, X. Ma, and X. Luo, “A refractory metamaterial absorber

for ultra-broadband, omnidirectional and polarization-independent absorption in the UV-NIR spectrum," *Nanoscale*, vol. 10, no. 17, 2018, doi: 10.1039/c8nr01728j.

[114] P. B. Johnson and R. W. Christy, "Optical constants of the noble metals," *Physical Review B*, vol. 6, no. 12, 1972, doi: 10.1103/PhysRevB.6.4370.

[115] E. D. Palik, *Handbook of optical constants of solids*, vol. 1. 2012. doi: 10.1016/C2009-0-20920-2.

[116] H. Caglayan, S. H. Hong, B. Edwards, C. R. Kagan, and N. Engheta, "Near-infrared metatronic nanocircuits by design," *Physical Review Letters*, vol. 111, no. 7, 2013, doi: 10.1103/PhysRevLett.111.073904.

[117] H. Hajian, A. Ghobadi, B. Butun, and E. Ozbay, "Nearly perfect resonant absorption and coherent thermal emission by hBN-based photonic crystals," *Optics Express*, vol. 25, no. 25, 2017, doi: 10.1364/oe.25.031970.

[118] J. Zhu, L. Zhang, S. Jiang, J. Y. Ou, and Q. H. Liu, "Selective light trapping of plasmonic stack metamaterials by circuit design," *Nanoscale*, vol. 12, no. 3, 2020, doi: 10.1039/c9nr07937h.

[119] C. F. Guo, T. Sun, F. Cao, Q. Liu, and Z. Ren, "Metallic nanostructures for light trapping in energy-harvesting devices," *Light: Science and Applications*, vol. 3. 2014. doi: 10.1038/lsa.2014.42.

[120] D. Schurig *et al.*, "Metamaterial electromagnetic cloak at microwave frequencies," *Science*, vol. 314, no. 5801, 2006, doi: 10.1126/science.1133628.

[121] R. Zhu, X. Wu, Y. Hou, G. Zheng, J. Zhu, and F. Gao, "Broadband Asymmetric Light Transmission at Metal/Dielectric Composite Grating," *Scientific Reports*, vol. 8, no. 1, 2018, doi: 10.1038/s41598-018-19329-7.

[122] D. R. Smith, W. J. Padilla, D. C. Vier, S. C. Nemat-Nasser, and S. Schultz, "Composite medium with simultaneously negative permeability and permittivity," *Physical Review Letters*, vol. 84, no. 18, 2000, doi: 10.1103/PhysRevLett.84.4184.

[123] M. E. Stewart *et al.*, "Nanostructured plasmonic sensors," *Chemical Reviews*, vol. 108, no. 2. 2008. doi: 10.1021/cr068126n.

[124] C. Ji, K. T. Lee, T. Xu, J. Zhou, H. J. Park, and L. J. Guo, "Engineering Light at the Nanoscale: Structural Color Filters and Broadband Perfect Absorbers," *Advanced Optical Materials*, vol. 5, no. 20. 2017. doi: 10.1002/adom.201700368.

[125] A. D. Khan, A. D. Khan, S. D. Khan, and M. Noman, "Light absorption enhancement in tri-layered composite metasurface absorber for solar cell applications," *Optical Materials*, vol. 84, 2018, doi: 10.1016/j.optmat.2018.07.009.

[126] S. U. M. Khan, M. Al-Shahry, and W. B. Ingler, “Efficient photochemical water splitting by a chemically modified n-TiO2,” *Science*, vol. 297, no. 5590, 2002, doi: 10.1126/science.1075035.

[127] F. P. García De Arquer, A. Mihi, and G. Konstantatos, “Large-Area Plasmonic-Crystal-Hot-Electron-Based Photodetectors,” *ACS Photonics*, vol. 2, no. 7, 2015, doi: 10.1021/acsphotonics.5b00149.

[128] A. Kong, B. Cai, P. Shi, and X. Yuan, “Ultra-broadband all-dielectric metamaterial thermal emitter for passive radiative cooling,” *Optics Express*, vol. 27, no. 21, 2019, doi: 10.1364/oe.27.030102.

[129] L. Lei, S. Li, H. Huang, K. Tao, and P. Xu, “Ultra-broadband absorber from visible to near-infrared using plasmonic metamaterial,” *Optics Express*, vol. 26, no. 5, 2018, doi: 10.1364/oe.26.005686.

[130] B. X. Wang, C. Tang, Q. Niu, Y. He, and R. Chen, “A broadband terahertz metamaterial absorber enabled by the simple design of a rectangular-shaped resonator with an elongated slot,” *Nanoscale Advances*, vol. 1, no. 9, 2019, doi: 10.1039/c9na00385a.

[131] Y. Cheng, H. Zou, J. Yang, X. Mao, and R. Gong, “Dual and broadband terahertz metamaterial absorber based on a compact resonator structure,” *Optical Materials Express*, vol. 8, no. 10, 2018, doi: 10.1364/ome.8.003104.

[132] J. Zhao *et al.*, “Broadband microwave absorption utilizing water-based metamaterial structures,” *Optics Express*, vol. 26, no. 7, 2018, doi: 10.1364/oe.26.008522.

[133] J. Zhang *et al.*, “Ultra-broadband microwave metamaterial absorber with tetramethylurea inclusion,” *Optics Express*, vol. 27, no. 18, 2019, doi: 10.1364/oe.27.025595.

[134] C.-H. Fann, J. Zhang, M. ElKabbash, W. R. Donaldson, E. Michael Campbell, and C. Guo, “Broadband infrared plasmonic metamaterial absorber with multipronged absorption mechanisms,” *Optics Express*, vol. 27, no. 20, 2019, doi: 10.1364/oe.27.027917.

[135] Y. Zou, J. Cao, X. Gong, R. Qian, and Z. An, “Ultrathin and electrically tunable metamaterial with nearly perfect absorption in mid-infrared,” *Applied Sciences (Switzerland)*, vol. 9, no. 16, 2019, doi: 10.3390/app9163358.

[136] M. Abb, P. Albella, J. Aizpurua, and O. L. Muskens, “All-optical control of a single plasmonic nanoantenna - ITO hybrid,” *Nano Letters*, vol. 11, no. 6, 2011, doi: 10.1021/nl200901w.

[137] X. Huang, W. He, F. Yang, J. Ran, Q. Yang, and S. Xie, “Thermally tunable metamaterial absorber based on strontium titanate in the terahertz regime,” *Optical Materials Express*, vol. 9, no. 3, 2019, doi: 10.1364/ome.9.001377.

[138] S. Chandra, D. Franklin, J. Cozart, A. Safaei, and D. Chanda, "Adaptive Multispectral Infrared Camouflage," *ACS Photonics*, vol. 5, no. 11, 2018, doi: 10.1021/acsphotonics.8b00972.

[139] W. X. Huang, X. G. Yin, C. P. Huang, Q. J. Wang, T. F. Miao, and Y. Y. Zhu, "Optical switching of a metamaterial by temperature controlling," *Applied Physics Letters*, vol. 96, no. 26, 2010, doi: 10.1063/1.3458706.

[140] N. Lee, T. Kim, J. S. Lim, I. Chang, and H. H. Cho, "Metamaterial-Selective Emitter for Maximizing Infrared Camouflage Performance with Energy Dissipation," *ACS Applied Materials and Interfaces*, vol. 11, no. 23, 2019, doi: 10.1021/acsami.9b04478.

[141] M. A. Kats *et al.*, "Vanadium dioxide as a natural disordered metamaterial: Perfect thermal emission and large broadband negative differential thermal emittance," *Physical Review X*, vol. 3, no. 4, 2014, doi: 10.1103/PhysRevX.3.041004.

[142] Z. Song, K. Wang, J. Li, and Q. H. Liu, "Broadband tunable terahertz absorber based on vanadium dioxide metamaterials," *Optics Express*, vol. 26, no. 6, 2018, doi: 10.1364/oe.26.007148.

[143] H. Liu, J. Lu, and X. R. Wang, "Metamaterials based on the phase transition of VO2," *Nanotechnology*, vol. 29, no. 2, 2018, doi: 10.1088/1361-6528/aa9cb1.

[144] Z. Zhu, P. G. Evans, R. F. Haglund, and J. G. Valentine, "Dynamically Reconfigurable Metadevice Employing Nanostructured Phase-Change Materials," *Nano Letters*, vol. 17, no. 8, 2017, doi: 10.1021/acs.nanolett.7b01767.

[145] Y. Sharma, V. A. Tiruveedhula, J. F. Muth, and A. Dhawan, "VO_2 based waveguide-mode plasmonic nano-gratings for optical switching," *Optics Express*, vol. 23, no. 5, 2015, doi: 10.1364/oe.23.005822.

[146] W. Cai *et al.*, "Electromagnetically induced transparency in all-dielectric metamaterials: Coupling between magnetic Mie resonance and substrate resonance," *Physical Review A*, vol. 100, no. 5, 2019, doi: 10.1103/PhysRevA.100.053804.

[147] W. Withayachumnankul *et al.*, "Plasmonic Resonance toward Terahertz Perfect Absorbers," *ACS Photonics*, vol. 1, no. 7, 2014, doi: 10.1021/ph500110t.

[148] L. Zhao, X. Yang, Q. Niu, Z. He, and S. Dong, "Linearly thermal-tunable near-infrared ultra-narrowband metamaterial perfect absorber with low power and a large modulation depth based on a four-nanorod-coupled a-silicon resonator," *Optics Letters*, vol. 44, no. 15, 2019, doi: 10.1364/ol.44.003885.

[149] D. Rosenblatt, A. Sharon, and A. A. Friesem, "Resonant grating waveguide structures," *IEEE Journal of Quantum Electronics*, vol. 33, no. 11, 1997, doi: 10.1109/3.641320.

[150] M. H. Nasr, M. A. K. Othman, I. A. Eshrah, and T. M. Abuelfadl, “Solution of cavity resonance and waveguide scattering problems using the eigenmode projection technique,” *Journal of Applied Physics*, vol. 121, no. 14, 2017, doi: 10.1063/1.4979860.

[151] M. Ng Mou Kehn and W. Y. Lai, “Modal Analysis of Gratings with Conducting Strip-Loaded Bars and Sandwiched between Multiple Dielectric Layers,” *IEEE Transactions on Antennas and Propagation*, vol. 68, no. 6, 2020, doi: 10.1109/TAP.2019.2955214.

[152] M. J. Dicken *et al.*, “Frequency tunable near-infrared metamaterials based on VO_2 phase transition,” *Optics Express*, vol. 17, no. 20, 2009, doi: 10.1364/oe.17.018330.

[153] D. Hohlfeld and H. Zappe, “An all-dielectric tunable optical filter based on the thermo-optic effect,” *Journal of Optics A: Pure and Applied Optics*, vol. 6, no. 6, 2004, doi: 10.1088/1464-4258/6/6/002.

[154] Y. Bai, L. Zhao, D. Ju, Y. Jiang, and L. Liu, “Wide-angle, polarization-independent and dual-band infrared perfect absorber based on L-shaped metamaterial,” *Optics Express*, vol. 23, no. 7, 2015, doi: 10.1364/oe.23.008670.

[155] X. Sun, Y. Sun, Z. Zhou, M. A. Alam, and P. Bermel, “Radiative sky cooling: Fundamental physics, materials, structures, and applications,” *Nanophotonics*, vol. 6, no. 5. 2017. doi: 10.1515/nanoph-2017-0020.

[156] D. Zhao *et al.*, “Radiative sky cooling: Fundamental principles, materials, and applications,” *Applied Physics Reviews*, vol. 6, no. 2. 2019. doi: 10.1063/1.5087281.

[157] D. Liu, H. Ji, R. Peng, H. Cheng, and C. Zhang, “Infrared chameleon-like behavior from VO2(M) thin films prepared by transformation of metastable VO2(B) for adaptive camouflage in both thermal atmospheric windows,” *Solar Energy Materials and Solar Cells*, vol. 185, 2018, doi: 10.1016/j.solmat.2018.05.042.

[158] B. Ko, D. Lee, T. Badloe, and J. Rho, “Metamaterial-based radiative cooling: Towards energy-free all-day cooling,” *Energies*, vol. 12, no. 1. 2019. doi: 10.3390/en12010089.

[159] F. T. Maremi, N. Lee, G. Choi, T. Kim, and H. H. Cho, “Design of multilayer ring emitter based on metamaterial for thermophotovoltaic applications,” *Energies*, vol. 11, no. 9, 2018, doi: 10.3390/en11092299.

[160] J. Zhou *et al.*, “Ultra-broadband solar absorbers for high-efficiency thermophotovoltaics,” *Optics Express*, vol. 28, no. 24, 2020, doi: 10.1364/oe.411918.

[161] B. Khalichi, A. Ghobadi, A. Kalantari Osgouei, and E. Ozbay, “Diode like high-contrast asymmetric transmission of linearly polarized waves based on plasmon-tunneling effect coupling to electromagnetic radiation modes,” *Journal of Physics D: Applied Physics*, vol. 54, no. 36, 2021, doi: 10.1088/1361-6463/ac0ab8.

[162] M. K. Hedayati *et al.*, "Design of a perfect black absorber at visible frequencies using plasmonic metamaterials," *Advanced Materials*, vol. 23, no. 45, 2011, doi: 10.1002/adma.201102646.

[163] F. Lou *et al.*, "Nanosecond-pulsed, dual-wavelength, passively Q-switched ytterbium-doped bulk laser based on few-layer MoS_2 saturable absorber," *Photonics Research*, vol. 3, no. 2, 2015, doi: 10.1364/prj.3.000a25.

[164] D. G. Baranov, Y. Xiao, I. A. Nechepurenko, A. Krasnok, A. Alù, and M. A. Kats, "Nanophotonic engineering of far-field thermal emitters," *Nature Materials*, vol. 18, no. 9. 2019. doi: 10.1038/s41563-019-0363-y.

[165] A. K. Osgouei, E. Buhara, B. Khalichi, A. Ghobadi, and E. Ozbay, "Wavelength selectivity in a polarization-insensitive metamaterial-based absorber consistent with atmospheric absorption windows," 2021.

[166] B. Khalichi, A. Ghobadi, A. K. Osgouei, H. Kocer, and E. Ozbay, "A Transparent all-dielectric multifunctional nanoantenna Emitter Compatible with Thermal Infrared and Cooling Scenarios," *IEEE access*, 2021.

[167] E. Buhara, A. Ghobadi, B. Khalichi, H. Kocer, and E. Ozbay, "Mid-infrared adaptive thermal camouflage using a phase-change material coupled dielectric nanoantenna," *Journal of Physics D: Applied Physics*, vol. 54, no. 26, 2021, doi: 10.1088/1361-6463/abf53d.

[168] L. Peng, D. Liu, H. Cheng, S. Zhou, and M. Zu, "A Multilayer Film Based Selective Thermal Emitter for Infrared Stealth Technology," *Advanced Optical Materials*, vol. 6, no. 23, 2018, doi: 10.1002/adom.201801006.

[169] H. Zhu *et al.*, "High-temperature infrared camouflage with efficient thermal management," *Light: Science and Applications*, vol. 9, no. 1, 2020, doi: 10.1038/s41377-020-0300-5.

[170] O. Salihoglu *et al.*, "Graphene-Based Adaptive Thermal Camouflage," *Nano Letters*, vol. 18, no. 7, 2018, doi: 10.1021/acs.nanolett.8b01746.

[171] J. Kim, K. Han, and J. W. Hahn, "Selective dual-band metamaterial perfect absorber for infrared stealth technology," *Scientific Reports*, vol. 7, no. 1, 2017, doi: 10.1038/s41598-017-06749-0.

[172] T. Kim, J. Y. Bae, N. Lee, and H. H. Cho, "Hierarchical Metamaterials for Multispectral Camouflage of Infrared and Microwaves," *Advanced Functional Materials*, vol. 29, no. 10, 2019, doi: 10.1002/adfm.201807319.

[173] E. Buhara, A. K. Osgouei, B. Khalichi, H. Kocer, A. Ghobadi, and E. Ozbay, "Thermally tunable from narrowband to broadband metamaterial-based nanoantenna emitter," 2021.

[174] V. Erçaglar, V. Erturk, A. Ghobadi, D. U. Yildirim, and E. Ozbay, "Numerical analysis of a thermally tunable spectrally selective absorber enabled by an all-dielectric metamirror," *Optics Letters*, vol. 45, no. 22, 2020, doi: 10.1364/ol.409586.

[175] V. Ercağlar, H. Hajian, and E. Ozbay, "VO2-graphene-integrated hBN-based metasurface for bi-tunable phonon-induced transparency and nearly perfect resonant absorption," *Journal of Physics D: Applied Physics*, vol. 54, no. 24, 2021, doi: 10.1088/1361-6463/abecb2.

[176] A. K. Osgouei, H. Hajian, A. E. Serebryannikov, and E. Ozbay, "Hybrid indium tin oxide-Au metamaterial as a multiband bi-functional light absorber in the visible and near-infrared ranges," *Journal of Physics D: Applied Physics*, vol. 54, no. 27, 2021, doi: 10.1088/1361-6463/abf579.

[177] D. T. Ha *et al.*, "Switching between perfect absorption and polarization conversion, based on hybrid metamaterial in the GHz and THz bands," *Journal of Physics D: Applied Physics*, vol. 54, no. 23, 2021, doi: 10.1088/1361-6463/abeb97.

[178] X. Liu, T. Tyler, T. Starr, A. F. Starr, N. M. Jokerst, and W. J. Padilla, "Taming the blackbody with infrared metamaterials as selective thermal emitters," *Physical Review Letters*, vol. 107, no. 4, 2011, doi: 10.1103/PhysRevLett.107.045901.

[179] Z. Li, L. Stan, D. A. Czaplewski, X. Yang, and J. Gao, "Wavelength-selective mid-infrared metamaterial absorbers with multiple tungsten cross resonators," *Optics Express*, vol. 26, no. 5, 2018, doi: 10.1364/oe.26.005616.

[180] B. Khalichi, A. K. Osgouei, E. Buhara, H. Kocer, A. Ghobadi, and E. Ozbay, "Active thermally tunable samarium nickelate-based nanoantenna emitter," 2021.

[181] A. K. Osgouei, B. Khalichi, E. Buhara, A. Ghobadi, and E. Ozbay, "Dual-band polarization insensitive metamaterial-based absorber suitable for sensing applications," 2021.

[182] Q. Kang, D. Li, K. Guo, J. Gao, and Z. Guo, "Tunable thermal camouflage based on gst plasmonic metamaterial," *Nanomaterials*, vol. 11, no. 2, 2021, doi: 10.3390/nano11020260.

[183] X. Feng *et al.*, "Hierarchical metamaterials for laser-infrared-microwave compatible camouflage," *Optics Express*, vol. 28, no. 7, 2020, doi: 10.1364/oe.388335.

[184] M. Li, D. Liu, H. Cheng, L. Peng, and M. Zu, "Manipulating metals for adaptive thermal camouflage," *Science Advances*, vol. 6, no. 22, 2020, doi: 10.1126/sciadv.aba3494.

[185] M. G. Moharam, T. K. Gaylord, D. A. Pommet, and E. B. Grann, "Stable implementation of the rigorous coupled-wave analysis for surface-relief gratings: enhanced transmittance matrix approach," *Journal of the Optical Society of America A*, vol. 12, no. 5, 1995, doi:

10.1364/josaa.12.001077.

[186] M. L. Williams, “CRC Handbook of Chemistry and Physics, 76th edition,” *Occupational and Environmental Medicine*, vol. 53, no. 7, 1996, doi: 10.1136/oem.53.7.504.

[187] J. Li, R. Gan, Q. Guo, H. Liu, J. Xu, and F. Yi, “Tailoring optical responses of infrared plasmonic metamaterial absorbers by optical phonons,” *Optics Express*, vol. 26, no. 13, 2018, doi: 10.1364/oe.26.016769.

[188] A. Berk, P. Conforti, R. Kennett, T. Perkins, F. Hawes, and J. van den Bosch, “MODTRAN® 6: A major upgrade of the MODTRAN® radiative transfer code,” in *Workshop on Hyperspectral Image and Signal Processing, Evolution in Remote Sensing*, 2014, vol. 2014-June. doi: 10.1109/WHISPERS.2014.8077573.

[189] F. Omeis, R. Smaali, F. Gonzalez-Posada, L. Cerutti, T. Taliercio, and E. Centeno, “Metal-insulator-metal antennas in the far-infrared range based on highly doped InAsSb,” *Applied Physics Letters*, vol. 111, no. 12, 2017, doi: 10.1063/1.4995515.

[190] J. Jung, T. Søndergaard, and S. I. Bozhevolnyi, “Gap plasmon-polariton nanoresonators: Scattering enhancement and launching of surface plasmon polaritons,” *Physical Review B - Condensed Matter and Materials Physics*, vol. 79, no. 3, 2009, doi: 10.1103/PhysRevB.79.035401.

[191] R. A. Deshpande, F. Ding, and S. Bozhevolnyi, “Dual-Band Metasurfaces Using Multiple Gap-Surface Plasmon Resonances,” *ACS Applied Materials and Interfaces*, vol. 12, no. 1, 2020, doi: 10.1021/acsami.9b15410.

[192] F. Ding, Y. Yang, R. A. Deshpande, and S. I. Bozhevolnyi, “A review of gap-surface plasmon metasurfaces: Fundamentals and applications,” *Nanophotonics*, vol. 7, no. 6. 2018. doi: 10.1515/nanoph-2017-0125.

[193] M. G. Nielsen, D. K. Gramotnev, A. Pors, O. Albrektsen, and S. I. Bozhevolnyi, “Continuous layer gap plasmon resonators,” *Optics Express*, vol. 19, no. 20, 2011, doi: 10.1364/oe.19.019310.

[194] L. P. Wang and Z. M. Zhang, “Wavelength-selective and diffuse emitter enhanced by magnetic polaritons for thermophotovoltaics,” *Applied Physics Letters*, vol. 100, no. 6, 2012, doi: 10.1063/1.3684874.

[195] B. J. Lee, L. P. Wang, and Z. M. Zhang, “Coherent thermal emission by excitation of magnetic polaritons between periodic strips and a metallic film,” *Optics Express*, vol. 16, no. 15, 2008, doi: 10.1364/oe.16.011328.

[196] A. Ghobadi, H. Hajian, B. Butun, and E. Ozbay, “Strong Light-Matter Interaction in Lithography-Free Planar Metamaterial Perfect Absorbers,” *ACS Photonics*, vol. 5, no. 11.

2018. doi: 10.1021/acsphotonics.8b00872.

[197] G. W. Hanson, “Dyadic Green’s functions and guided surface waves for a surface conductivity model of graphene,” *Journal of Applied Physics*, vol. 103, no. 6, 2008, doi: 10.1063/1.2891452.

[198] J. S. Gómez-Díaz and J. Perruisseau-Carrier, “Graphene-based plasmonic switches at near infrared frequencies,” *Optics Express*, vol. 21, no. 13, 2013, doi: 10.1364/oe.21.015490.

[199] M. Amin, M. Farhat, and H. Bağci, “A dynamically reconfigurable Fano metamaterial through graphene tuning for switching and sensing applications,” *Scientific Reports*, vol. 3, 2013, doi: 10.1038/srep02105.

[200] S. K. Patel, S. Charola, J. Parmar, and M. Ladumor, “Broadband metasurface solar absorber in the visible and near-infrared region,” *Materials Research Express*, vol. 6, no. 8, 2019, doi: 10.1088/2053-1591/ab207d.

[201] H. Wang and L. Wang, “Perfect selective metamaterial solar absorbers,” *Optics Express*, vol. 21, no. S6, 2013, doi: 10.1364/oe.21.0a1078.

[202] J. Tong, M. Muthee, S. Y. Chen, S. K. Yngvesson, and J. Yan, “Antenna Enhanced Graphene THz Emitter and Detector,” *Nano Letters*, vol. 15, no. 8, 2015, doi: 10.1021/acs.nanolett.5b01635.

[203] D. Rodrigo *et al.*, “Mid-infrared plasmonic biosensing with graphene,” *Science*, vol. 349, no. 6244, 2015, doi: 10.1126/science.aab2051.

[204] S. A. Mikhailov, “Graphene-based voltage-tunable coherent terahertz emitter,” *Physical Review B - Condensed Matter and Materials Physics*, vol. 87, no. 11, 2013, doi: 10.1103/PhysRevB.87.115405.

[205] H. S. Chu and C. How Gan, “Active plasmonic switching at mid-infrared wavelengths with graphene ribbon arrays,” *Applied Physics Letters*, vol. 102, no. 23, 2013, doi: 10.1063/1.4810003.

[206] P. Y. Chen, C. Argyropoulos, M. Farhat, and J. S. Gomez-Diaz, “Flatland plasmonics and nanophotonics based on graphene and beyond,” *Nanophotonics*, vol. 6, no. 6. 2017. doi: 10.1515/nanoph-2016-0137.

[207] Y. Zhang *et al.*, “Independently tunable dual-band perfect absorber based on graphene at mid-infrared frequencies,” *Scientific Reports*, vol. 5, 2015, doi: 10.1038/srep18463.

[208] I. T. Lin, Y. P. Lai, K. H. Wu, and J. M. Liu, “Terahertz optoelectronic property of graphene: Substrate-induced effects on plasmonic characteristics,” *Applied Sciences (Switzerland)*, vol. 4, no. 1, 2014, doi: 10.3390/app4010028.

[209] M. Lei, N. Feng, Q. Wang, Y. Hao, S. Huang, and K. Bi, “Magnetically tunable

metamaterial perfect absorber," *Journal of Applied Physics*, vol. 119, no. 24, 2016, doi: 10.1063/1.4954224.

[210] V. Kuzmiak and A. A. Maradudin, "Asymmetric transmission of surface plasmon polaritons on planar gratings," *Physical Review A - Atomic, Molecular, and Optical Physics*, vol. 92, no. 5, 2015, doi: 10.1103/PhysRevA.92.053813.

[211] M. Mutlu, A. E. Akosman, A. E. Serebryannikov, and E. Ozbay, "Diodelike asymmetric transmission of linearly polarized waves using magnetoelectric coupling and electromagnetic wave tunneling," *Physical Review Letters*, vol. 108, no. 21, 2012, doi: 10.1103/PhysRevLett.108.213905.

[212] P. Xu *et al.*, "Dichroic Optical Diode Transmission in Two Dislocated Parallel Metallic Gratings," *Nanoscale Research Letters*, vol. 13, no. 1, 2018, doi: 10.1186/s11671-018-2818-5.

[213] R. Singh *et al.*, "Terahertz metamaterial with asymmetric transmission," *Physical Review B - Condensed Matter and Materials Physics*, vol. 80, no. 15, 2009, doi: 10.1103/PhysRevB.80.153104.

[214] Z. Li, M. Mutlu, and E. Ozbay, "Highly asymmetric transmission of linearly polarized waves realized with a multilayered structure including chiral metamaterials," *Journal of Physics D: Applied Physics*, vol. 47, no. 7, 2014, doi: 10.1088/0022-3727/47/7/075107.

[215] T. J. Davis, F. Eftekhari, D. E. Gómez, and A. Roberts, "Metasurfaces with Asymmetric Optical Transfer Functions for Optical Signal Processing," *Physical Review Letters*, vol. 123, no. 1, 2019, doi: 10.1103/PhysRevLett.123.013901.

[216] J. H. Shi, H. F. Ma, C. Y. Guan, Z. P. Wang, and T. J. Cui, "Broadband chirality and asymmetric transmission in ultrathin 90°-twisted Babinet-inverted metasurfaces," *Physical Review B - Condensed Matter and Materials Physics*, vol. 89, no. 16, 2014, doi: 10.1103/PhysRevB.89.165128.

[217] B. Khalichi, E. Buhara, A. K. Osgouei, A. Ghobadi, and E. Ozbay, "High contrast asymmetric transmission based on the outcoupling of surface plasmon polaritons to radiation modes," 2021.

[218] M. Ismail Khan, B. Hu, Y. Chen, N. Ullah, M. J. I. Khan, and A. R. Khalid, "Multiband Efficient Asymmetric Transmission with Polarization Conversion Using Chiral Metasurface," *IEEE Antennas and Wireless Propagation Letters*, vol. 19, no. 7, 2020, doi: 10.1109/LAWP.2020.2991521.

[219] C. Huang, Y. Feng, J. Zhao, Z. Wang, and T. Jiang, "Asymmetric electromagnetic wave transmission of linear polarization via polarization conversion through chiral metamaterial

structures," *Physical Review B - Condensed Matter and Materials Physics*, vol. 85, no. 19, 2012, doi: 10.1103/PhysRevB.85.195131.

[220] M. Kang, J. Chen, H.-X. Cui, Y. Li, and H.-T. Wang, "Asymmetric transmission for linearly polarized electromagnetic radiation," *Optics Express*, vol. 19, no. 9, 2011, doi: 10.1364/oe.19.008347.

[221] C. Menzel *et al.*, "Asymmetric transmission of linearly polarized light at optical metamaterials," *Physical Review Letters*, vol. 104, no. 25, 2010, doi: 10.1103/PhysRevLett.104.253902.

[222] Y. Ling *et al.*, "Asymmetric optical transmission based on unidirectional excitation of surface plasmon polaritons in gradient metasurface," *Optics Express*, vol. 25, no. 12, 2017, doi: 10.1364/oe.25.013648.

[223] Y. Li *et al.*, "Dual-band asymmetric transmission and circular dichroism in hybrid coupled plasmonic metamaterials," *Journal of Physics D: Applied Physics*, vol. 51, no. 28, 2018, doi: 10.1088/1361-6463/aac9a3.

[224] C. Pan, M. Ren, Q. Li, S. Fan, and J. Xu, "Broadband asymmetric transmission of optical waves from spiral plasmonic metamaterials," *Applied Physics Letters*, vol. 104, no. 12, 2014, doi: 10.1063/1.4869762.

[225] X. Li, R. Feng, and W. Ding, "Extremely high contrast asymmetric transmission with linear tunability in chiral metamaterials," *Journal of Physics D: Applied Physics*, vol. 51, no. 14, 2018, doi: 10.1088/1361-6463/aab0c2.

[226] Z. Li, W. Liu, H. Cheng, S. Chen, and J. Tian, "Tunable dual-band asymmetric transmission for circularly polarized waves with graphene planar chiral metasurfaces," *Optics Letters*, vol. 41, no. 13, 2016, doi: 10.1364/ol.41.003142.

[227] D. J. Liu, Z. Y. Xiao, X. L. Ma, and Z. H. Wang, "Asymmetric transmission of linearly and circularly polarized waves in metamaterial due to symmetry-breaking," *Applied Physics Express*, vol. 8, no. 5, 2015, doi: 10.7567/APEX.8.052001.

[228] X. J. Shang *et al.*, "Asymmetric transmission and polarization conversion of linearly polarized waves with bilayer L-shaped metasurfaces," *Applied Physics Express*, vol. 10, no. 5, 2017, doi: 10.7567/APEX.10.052602.

[229] S. Cakmakyapan, A. E. Serebryannikov, H. Caglayan, and E. Ozbay, "One-way transmission through the subwavelength slit in nonsymmetric metallic gratings," *Optics Letters*, vol. 35, no. 15, 2010, doi: 10.1364/ol.35.002597.

[230] C. Pfeiffer, C. Zhang, V. Ray, L. J. Guo, and A. Grbic, "High performance bianisotropic metasurfaces: Asymmetric transmission of light," *Physical Review Letters*, vol. 113, no. 2,

2014, doi: 10.1103/PhysRevLett.113.023902.

[231] C. Ba, L. Huang, W. Liu, S. Li, Y. Ling, and H. Li, “Narrow-band and high-contrast asymmetric transmission based on metal-metal-metal asymmetric gratings,” *Optics Express*, vol. 27, no. 18, 2019, doi: 10.1364/oe.27.025107.

[232] A. K. Sharma and A. K. Pandey, “ Self-referenced plasmonic sensor with TiO 2 grating on thin Au layer: simulated performance analysis in optical communication band ,” *Journal of the Optical Society of America B*, vol. 36, no. 8, 2019, doi: 10.1364/josab.36.000f25.

[233] M. Abutoama and I. Abdulhalim, “Self-referenced biosensor based on thin dielectric grating combined with thin metal film,” *Optics Express*, vol. 23, no. 22, 2015, doi: 10.1364/oe.23.028667.

[234] Y. Zhao, R. jie Tong, F. Xia, and Y. Peng, “Current status of optical fiber biosensor based on surface plasmon resonance,” *Biosensors and Bioelectronics*, vol. 142. 2019. doi: 10.1016/j.bios.2019.111505.

[235] C. Hu and D. Liu, “Transmission-type SPR sensor based on coupling of surface plasmons to radiation modes using a dielectric grating,” *Frontiers of Optoelectronics in China*, vol. 2, no. 2, 2009, doi: 10.1007/s12200-009-0040-x.

[236] K. M. Byun, S. J. Kim, and D. Kim, “Grating-coupled transmission-type surface plasmon resonance sensors based on dielectric and metallic gratings,” *Applied Optics*, vol. 46, no. 23, 2007, doi: 10.1364/AO.46.005703.

[237] S. Wedge and W. L. Barnes, “Surface plasmon-polariton mediated light emission through thin metal films,” *Optics Express*, vol. 12, no. 16, 2004, doi: 10.1364/opex.12.003673.

[238] S. Shen, E. Forsberg, Z. Han, and S. He, “Strong resonant coupling of surface plasmon polaritons to radiation modes through a thin metal slab with dielectric gratings,” *Journal of the Optical Society of America A*, vol. 24, no. 1, 2007, doi: 10.1364/josaa.24.000225.

[239] C. Lenaerts, F. Michel, B. Tilkens, Y. Lion, and Y. Renotte, “High transmission efficiency for surface plasmon resonance by use of a dielectric grating,” *Applied Optics*, vol. 44, no. 28, 2005, doi: 10.1364/AO.44.006017.

[240] S. Park, G. Lee, S. H. Song, C. H. Oh, and P. S. Kim, “Resonant coupling of surface plasmons to radiation modes by use of dielectric gratings,” *Optics Letters*, vol. 28, no. 20, 2003, doi: 10.1364/ol.28.001870.

[241] L. Zhang *et al.*, “Theoretical realization of robust broadband transparency in ultrathin seamless nanostructures by dual blackbodies for near infrared light,” *Nanoscale*, vol. 5, no. 8, 2013, doi: 10.1039/c3nr34278f.

[242] L. Zhou, W. Wen, C. T. Chan, and P. Sheng, “Electromagnetic-wave tunneling through

negative-permittivity media with high magnetic fields," *Physical Review Letters*, vol. 94, no. 24, 2005, doi: 10.1103/PhysRevLett.94.243905.

[243] T. Xu and H. J. Lezec, "Visible-frequency asymmetric transmission devices incorporating a hyperbolic metamaterial," *Nature Communications*, vol. 5, 2014, doi: 10.1038/ncomms5141.

[244] H. Kocer, I. Isik, Y. Durna, B. Khalichi, H. Kurt, and E. Ozbay, "Nano shell impact on Huygens' metasurface dipolar resonances and optical response," *Journal of the Optical Society of America B, JOSA B*, 2021.

[245] Ł. Zinkiewicz, J. Haberko, and P. Wasylczyk, "Highly asymmetric near infrared light transmission in an all-dielectric grating-on-mirror photonic structure," *Optics Express*, vol. 23, no. 4, 2015, doi: 10.1364/oe.23.004206.

[246] L. Zeng, M. Chen, W. Yan, Z. Li, and F. Yang, "Si-grating-assisted SPR sensor with high figure of merit based on Fabry–Pérot cavity," *Optics Communications*, vol. 457, 2020, doi: 10.1016/j.optcom.2019.124641.

[247] A. Orlandi, "Advanced Engineering Electromagnetics (Balanis, C.A.; 2012) [Book Review]," *IEEE Electromagnetic Compatibility Magazine*, vol. 4, no. 4, 2016, doi: 10.1109/memc.2015.7407175.

[248] J. A. Dionne, L. A. Sweatlock, H. A. Atwater, and A. Polman, "Planar metal plasmon waveguides: Frequency-dependent dispersion, propagation, localization, and loss beyond the free electron model," *Physical Review B - Condensed Matter and Materials Physics*, vol. 72, no. 7, 2005, doi: 10.1103/PhysRevB.72.075405.

[249] M. G. Moharam, T. K. Gaylord, E. B. Grann, and D. A. Pommet, "Formulation for stable and efficient implementation of the rigorous coupled-wave analysis of binary gratings," *Journal of the Optical Society of America A*, vol. 12, no. 5, 1995, doi: 10.1364/josaa.12.001068.

[250] E. Bosdurmaz, H. Hajian, V. Erçağlar, and E. Özbay, "A novel graphene-based metasurface absorber for the active and broadband manipulation for terahertz radiation," *Journal of the Optical Society of America B, JOSA B*, 2021.

[251] E. Buhara, A. Ghobadi, and E. Ozbay, "An All-Dielectric Metasurface Coupled with Two-Dimensional Semiconductors for Thermally Tunable Ultra-narrowband Light Absorption," *Plasmonics*, vol. 16, no. 3, 2021, doi: 10.1007/s11468-020-01330-4.

[252] A. K. Osgouei, A. Ghobadi, B. Khalichi, and E. Ozbay, "A spectrally selective gap surface-plasmon-based nanoantenna emitter compatible with multiple thermal infrared applications," *Journal of Optics.*, 2021.

Appendix A

Scientific Contributions

A.1 Jounal Articles

[1] **A. K. Osgouei**, A. Ghobadi, B. Khalichi, and E. Ozbay, "A spectrally selective gap surface-plasmon-based nanoantenna emitter compatible with multiple thermal infrared applications," *Journal of Optics.*, 2021.

[2] **A. K. Osgouei**, H. Hajian, A. E. Serebryannikov, and E. Ozbay, "Hybrid indium tin oxide-Au metamaterial as a multiband bi-functional light absorber in the visible and near-infrared ranges," *Journal of Physics D: Applied Physics*, vol. 54, no. 27, 2021, doi: 10.1088/1361-6463/abf579.

[3] **A. K. Osgouei**, H. Hajian, B. Khalichi, A. E. Serebryannikov, A. Ghobadi, and E. Ozbay, "Active Tuning from Narrowband to Broadband Absorbers Using a Sub-wavelength VO_2 Embedded Layer," *Plasmonics*, 2021, doi: 10.1007/s11468-020-01370-w.

[4] B. Khalichi, A. Ghobadi, **A. K. Osgouei**, and E. Ozbay, "Diode like high-contrast asymmetric transmission of linearly polarized waves based on

plasmon-tunneling effect coupling to electromagnetic radiation modes," *Journal of Physics D: Applied Physics*, vol. 54, no. 36, 2021, doi: 10.1088/1361-6463/ac0ab8.

[5] B. Khalichi, A. Ghobadi, **A. K. Osgouei**, H. Kocer, and E. Ozbay, "A Transparent all-dielectric multifunctional nanoantenna Emitter Compatible with Thermal Infrared and Cooling Scenarios," *IEEE access*, 2021.

A.2 Conference Papers

[1] **A. K. Osgouei**, B. Khalichi, E. Buhara, A. Ghobadi, and E. Ozbay, "Dual-band polarization insensitive metamaterial-based absorber suitable for sensing applications," 2021.

[2] **A. K. Osgouei**, E. Buhara, B. Khalichi, A. Ghobadi, and E. Ozbay, "Wavelength selectivity in a polarization-insensitive metamaterial-based absorber consistent with atmospheric absorption windows," 2021.

[3] B. Khalichi, **A. K. Osgouei**, E. Buhara, H. Kocer, A. Ghobadi, and E. Ozbay, "Active thermally tunable samarium nickelate-based nanoantenna emitter," 2021.

[4] B. Khalichi, E. Buhara, **A. K. Osgouei**, A. Ghobadi, and E. Ozbay, "High contrast asymmetric transmission based on the outcoupling of surface plasmon polaritons to radiation modes," 2021.

[5] E. Buhara, **A. K. Osgouei**, B. Khalichi, H. Kocer, A. Ghobadi, and E. Ozbay, "Thermally tunable from narrowband to broadband metamaterial-based nanoantenna emitter," 2021.